RUPRECHT-KARLS-UNIVERSITÄT HEIDELBERG

Susanne Jungmann

Development of New Detector Technologies - Čerenkov Light Readout with Silicon Photomultipliers

Diploma Thesis

HD-KIP-29-11

KIRCHHOFF-INSTITUT FÜR PHYSIK

Fakultät für Physik und Astronomie

Ruprecht-Karls-Universität Heidelberg

Diplomarbeit

Im Studiengang Physik

vorgelegt von

Susanne Jungmann

geboren in Heidelberg

-2011-

Entwicklung neuer Detektortechnologien - Auslese von Čerenkov Licht mittels Silizium Photomultiplier

Die Diplomarbeit wurde von Susanne Jungmann

ausgeführt am

Deutschen Elektronen-Synchrotron, Hamburg

unter der Betreuung von

Prof. Dr. Hans-Christian Schultz-Coulon

Dr. Erika Garutti

Department of Physics and Astronomy

University of Heidelberg

Diploma thesis

in Physics

submitted by

Susanne Jungmann

born in Heidelberg

-2011-

Development of

New Detector Technologies

-

Čerenkov Light Readout with

Silicon Photomultipliers

This diploma thesis has been carried out by Susanne Jungmann

at the

Deutsches Elektronen-Synchrotron, Hamburg

under the supervision of

Prof. Dr. Hans-Christian Schultz-Coulon

Dr. Erika Garutti

Development of

New Detector Technologies

-

Čerenkov Light Readout with

Silicon Photomultipliers

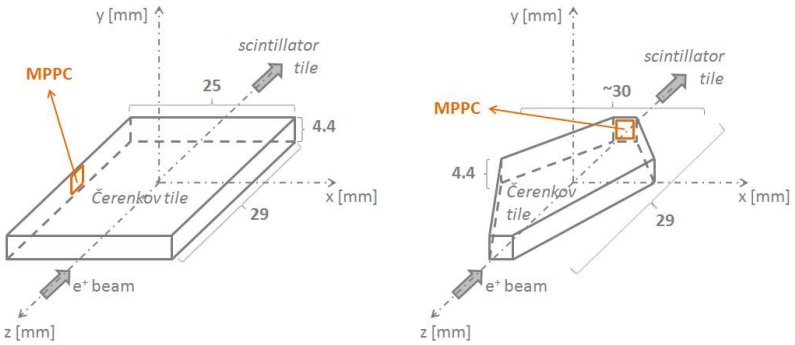

Susanne Jungmann

-February 2011-

Development of new detector technologies - Čerenkov light readout with silicon photomultipliers:

Future experiments in the field of high-energy particle physics require a jet energy resolution that is a factor two better than achieved so far. Up to date this goal seems to be achievable by either using the Particle Flow or the Dual-Readout method. The essential prerequisite if using the former is an unprecedented high granularity of the calorimeter system. In this case the light signals are readout with a novel kind of photodetectors, called Silicon Photomultiplier (SiPM), which convince through their compactness and high gain. The second approach exploits the phenomenon of Čerenkov light produced almost exclusively by the electromagnetic shower component of hadronic showers.
A combination of the two approaches in one highly granular hadronic calorimeter could be realized by integrating additional small Čerenkov tiles readout with SiPM's. Within the scope of this thesis first measurements have been performed at the DESY test beam facility to study the light yield achievable with small tiles. The Čerenkov light was produced by a positron beam traversing either sapphire or lead glass tiles. The photons were afterwards detected by a directly coupled SiPM by Hamamatsu. Different tile shapes and SiPM mounting positions were studied to find the optimal configuration.
The measured light yield and the observed tile behavior was reconstructed with Monte-Carlo studies.

Entwicklung neuer Detektortechnologien - Die Auslese von Cherenkov Licht mittels Silicon Photomultiplier:

Zukünftige Experimente auf dem Gebiet der Hochenergiephysik erfordern eine Jet Energieauflösung, die um einen Faktor zwei höher ist als jemals erzielt. Aktuell scheint dieses Ziel erreichbar zu sein, indem entweder die Particle Flow oder die Dual-Readout Methode benutzt wird. Eine unabdingbare Voraussetzung für erstere Methode ist eine beispiellose Granularität des Kalorimetersystems. Die Signalauslese wird in diesem Fall mit neuartigen Photodetektoren, sogenannten Silicon Photomultiplier (SiPM), bewerktstelligt, die durch ihre Kompaktheit und ihren hohen Verstärkungsfaktor überzeugen. Der zweite Ansatz nutzt das Phänomen des Čerenkov Lichtes aus, das beinahe ausschließlich im elektromagnetischen Teil eines Hadronenschauers produziert wird.
Eine Kombination beider Ansätze in einem hochgranularen Hadronenkalorimeter könnte durch den Einbau zusätzlicher kleiner Čerenkov Kacheln umgesetzt werden, die mit SiPM's ausgelesen werden. Innerhalb der vorliegenden Arbeit wurden erste Messungen am DESY Teststrahl durchgeführt, um die mögliche Lichtausbeute kleiner Kacheln zu vermessen. Das Čerenkov Licht wurde produziert durch einen Positronen Strahl, der entweder Saphir oder Bleiglas Kacheln durchquerte. Die Photonen wurden anschließend ausgelesen durch einen direkt montierten SiPM von Hamamatsu. Unterschiedliche Kachelformen und SiPM Positionen wurden untersucht, um die optimale Konstellation zu finden.
Mittels Monte-Carlo Simulationen wurde die gemessene Lichtausbeute und das beobachtete Verhalten der Kacheln rekonstruiert.

Contents

1 Introduction

During the second half of the 20th century several experiments and theoretical developments gave rise to the nowadays well-established *Standard Model* (SM) of particle physics. It combines the electroweak and the strong interaction and is thus able to describe the fundamental forces between all known elementary particles. The SM successfully predicted new particles whose existence was later on verified by experiments at large particle accelerators.
The SM includes 12 elementary fermions with spin 1/2: 6 quarks and 6 leptons and their respective antiparticles. Following today's understanding of the interaction processes, namely electromagnetic, strong and weak interactions, the so-called gauge bosons are responsible for the intermediation of the fundamental forces between those particles. In case of the electromagnetic interaction the photons hold this function, for the strong interaction the gluons and in case of the weak interaction the $W^{\pm}$- and Z^0 bosons.
Despite such a remarkable success, the SM works only because of an unverified hypothesis: the *Higgs mechanism*. In particle physics, this is the essential process which explains the origin of masses of the $W^{\pm}$- and Z^0 weak gauge bosons through electroweak symmetry breaking.
One of the main objectives of ongoing experiments is the search for the predicted neutral Higgs boson which has yet to be discovered. Results from previous experiments as LEP[1] and SLC[2] at CERN[3] or the Tevatron at FNAL[4] can state only a certain range in which its mass is expected to be found. So far, a lower limit of 114.4 GeV at 95 % confidence level for the Higgs mass is set [1]. In addition, recent combination of data gained at the Tevatron leads to the exclusion of a Higgs mass between 158 GeV and 175 GeV [2].
The most promising experiments with the ability to answer some of the open questions, are those running at the *Large Hadron Collider* (LHC) at CERN. There, colliding protons will reach a center-of-mass energy of $\sqrt{s} = 14\,\text{TeV}$. This energy regime allows the formation and detection of new particles in utterly unexplored mass regions. Therefore, its major goal is, next to finding the Higgs particle, the search for physics beyond the SM (e.g. supersymmetry, dark matter).
However, when colliding compound particles, as the proton consisting of quarks and gluons, the initial state of the scattering processes is unknown in contrary to a lepton collider.
As a consequence of this disadvantage, electron-positron colliders are proposed gen-

[1] **L**arge **E**lectron **P**ositron Collider
[2] **S**tanford **L**inear **C**ollider
[3] **C**onseil **E**uropéen pour la **R**echerche **N**ucléaire
[4] **F**ermi **N**ational **A**ccelerator **L**aboratory

erating much less interfering background events and are thus suitable for precise measurements of the physics discovered at the LHC. One of them, the *International Linear Collider* (ILC), is designed as a superconducting linear collider accelerating electrons and positrons. It is planned to have a center-of-mass energy ranging from $\sqrt{s} = 200\,\text{GeV}$ to $\sqrt{s} = 500\,\text{GeV}$ with a possible upgrade to $\sqrt{s} = 1\,\text{TeV}$ [3].
Based at CERN, a group of physicists works on a competing project that would substitute the ILC. The *Compact LInear Collider* (CLIC) design differs from the one of the ILC by using normal conducting cavities to achieve up to five times higher energies of several TeV at approximately the same length [4].
So it is up to the physics to decide which machine will be built. If the new physics is discovered at lower energies, the ILC might be sufficient. But if the Higgs or new supersymmetry particles are found to be much heavier, then a multi-TeV machine like CLIC will become necessary. This decision has to be made with great elaborateness considering that the ILC design, including possible detector concepts and detailed test beam measurements of its components, is years ahead of the status of CLIC.
Independently of which design will be realized in the end, it is clear that at such high center-of-mass energies new approaches have to be developed to meet the challenging demands placed on the detector performance.
The expected final states are typically multiple hadronic jets accompanied by low momentum leptons and/or missing energy. To fully exploit the physics potential a clear distinction between $W^{\pm}$- and/or Z^0 bosons in their decay modes into two jets has to be achieved. This accounts for a jet energy resolution of at least $\frac{30\,\%}{\sqrt{E_{jet}}}$ or 3 - 4% [3]. This is a factor of two better than reached with any operated calorimeter so far and hence drives the calorimeter design. The embedded hadronic calorimeter is the main limitation to the jet energy resolution. The energy dependent electromagnetic component of a hadronic shower fluctuates strongly from event to event and reduces the energy resolution considerably.
To meet the challenging jet energy resolution two calorimeter concepts are investigated. One approach is the development of a calorimeter structure with an unprecedented granularity in longitudinal as well as transverse direction. This enables the excellent tracking of individual particles as well as the correct assignment of particles to particular shower clusters based on their energy deposition inside the small calorimeter cells. For prototypes of such electromagnetic and hadronic calorimeters optimized for this design see [5] and [6].
The developed *Particle Flow Approach* (PFA) [7] is a new reconstruction method able to considerably improve the jet energy resolution up to jet energies of 1 TeV by measuring the energy in the detector component most suitable for a specific particle type. Thereby only a small fraction of the total energy is measured in the hadronic calorimeter (HCAL) whose jet energy resolution is the worst compared to the other detector components. The signal readout of the small single calorimeter cells can be managed with novel single photon-counting devices, called *Silicon Photomultiplier* (SiPM) that are commercially available.

The second, fundamentally different concept uses the dual-readout (DREAM) of scintillation and Čerenkov light of fibers or crystals to access the varying electromagnetic fraction contained in every hadronic shower. The DREAM detector prototype proved that the hadronic and electromagnetic component inside a shower can be independently measured exploiting the phenomenon of Čerenkov light. It is almost exclusively produced by charged relativistic particles as they are contained in electromagnetic showers. The recombination of the two signals yields an improvement in the jet energy resolution due to the reduction of fluctuations.
A combination of the two complementing approaches in one HCAL would require the same small cell size for both, the active scintillator layers and the Čerenkov layers.

Within the scope of this study first experimental studies with Čerenkov light producing tiles made of sapphire or lead glass were performed at the DESY test beam facility. They featured dimensions at the order of some centimeters. It was searched for an optimal tile configuration, concerning material, shape and surface finishing, to achieve a sufficiently high light yield.
After an introduction into detector and calorimetry physics in the next two chapters, the newly developed Silicon Photomultipliers used for the light detection are presented in chapter 4. The built setup and final results for differently shaped tile samples are presented in the chapters 5 and 6 respectively, while the outcome of Monte Carlo simulations is given in chapters 7 and 8. A summary and an outlook in chapter 9 complete this thesis.

2 Future Lepton Colliders

2.1 The International Linear Collider (ILC)

At any time first insights into particle physics at the Terascale are expected to be found at the currently running LHC. It was built in the tunnel of the former LEP collider at CERN that confirmed the advantages of a lepton collider. The maximum energy reached at LEP was 209 GeV in the year 2000. An energy upgrade was impossible because of the considerable large energy loss due to synchrotron radiation. For ultrarelativistic particles the energy loss per cycle is $-\Delta E \propto E^4/(m_0^4 \cdot R)$ where the radius of the ring accelerator R is fixed and E and m_0 are the energy and the mass of the particles. The ratio between proton and electron mass causes a $1.14 \cdot 10^{13}$ lower loss through synchrotron radiation for protons than for electrons and is therefore negligible at the LHC.
Although the LHC is able to achieve high center-of-mass energies of up to $\sqrt{s} = 14\,\text{TeV}$ providing a great physics potential, there are some drawbacks. Due to the nature of protons as compound objects, hold together by the strong force, there is a huge amount of background events accompanying each interesting event and an enormous radiation exposure of the detectors. To perform more precise measurements at the Terascale one has to leave behind the idea of a ring accelerator. One option is the planned International Linear Collider (ILC) [3] that will collide, unlike the LHC, positrons and electrons based on a linear accelerator structure. It will extend and complement the physics program of the LHC. Figure 2.1 shows a schematic layout of the ILC for a center-of-mass energy of initially 500 GeV. The ILC is based on 1.3 GHz superconducting radio-frequency (SCRF) accelerating cavities made of pure niobium. The electron source is a photocathode DC gun that is illuminated by a laser. The positrons are produced via photoproduction within

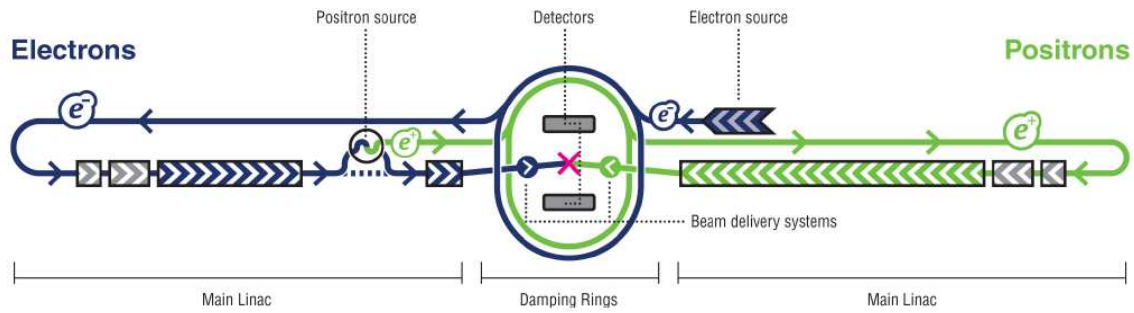

Figure 2.1: Schematic layout of the ILC at a center-of-mass energy of 500 GeV over a total site length of 31 km [3].

undulators driven by the 150 GeV main electron beam. Therefore high energetic photons ($\sim$ 10 MeV) produced by electrons traversing the undulator are directed onto a titanium-alloy target and converted into e^+e^- pairs. The electrons and remaining photons are separated from the positrons and dumped. It is aimed for a beam polarization of >80 % for the electrons and of at least 30 % for the positrons. Two 6.7 kilometre-circumference damping rings, one for the electrons and one for the positrons, are housed in one tunnel and operating at 5 GeV beam energy. In the damping rings the emittance of electrons and positrons is reduced making the bunches more compact before they are accelerated in the main linear accelerators. In the main linacs the beam is accelerated to a maximum energy of 250 GeV over a combined length of 23 km at an average accelerating gradient of 31.5 MV/m. The linacs are composed of radio frequency units, each of which are formed by three contiguous SCRF cryomodules. Finally, two 2 km long beam delivery systems on each side of the collision point focus the beam and bring it into head-on collision. The main ILC parameters are summarized in table 2.1.

Parameter	**Value**	**Unit**
Center-of-mass energy	200-500	GeV
Peak luminosity (*)	$\sim 2 \cdot 10^{34}$	$cm^{-2}s^{-1}$
Availability	75	%
Repetition rate	5	Hz
Main Linacs		
Length of each linac	11	km
Average accelerating gradient in cavity (*)	31.5	MV/m
RF pulse length	1.6	ms
Pulse length	$\sim$1	ms
Number of bunches per pulse	$1000 - 5400$	
Average beam current in pulse	9.0	mA
Charge per bunch	1.6 - 3.2	nC
Typical beam size at IP (h×v) (*)	640×5.7	nm
Damping Rings		
Beam energy	5	GeV
Circumference	6.7	km
Length of beam delivery system	4.5	km
Total site length	31	km
Total AC power consumption (*)	230	MW

Table 2.1: Main beam parameters of the ILC at the point of interaction. (*) Values at 500 GeV center-of-mass energy [3].

The interaction region of the ILC is designed to host two interchangeable detectors. They incorporate complementary technologies and can be moved into the beam with a *push-pull* scheme.

In total there are three different detector concepts [3], all of which are driven by the physics requirements and optimized for the Particle Flow Approach:

- The International Large Detector (ILD) [8]
- The Silicon Detector (SiD) [9]
- Fourth Concept ("4^{th}") Detector [10]

The ILD emerged from the prior Global Large Detector (GLD) [11] design and the Large Detector Concept (LDC) [12].
Even though all of those three remaining concepts pursue different detector technologies, they have in common an inner Vertex Detector, a Silicon Tracker or a Time Projection Chamber (TPC) as tracking system, calorimeters for the energy measurement and an outer muon detector. In the following only the ILD (figure 2.2) will be discussed briefly.

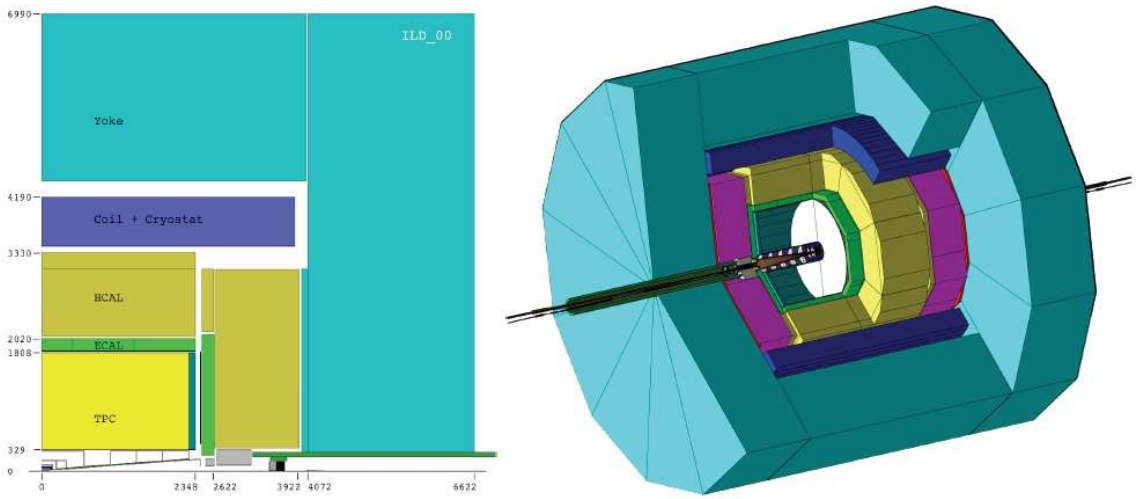

Figure 2.2: **Left:** View of the ILD as implemented by the MOKKA simulation package. **Right:** One quarter of the ILD with length specifications in [mm] [3].

The tracking detectors are closest to the interaction point and are designed to place as less material in front of the calorimeters as possible. They are used for track identification and momentum determination of charged particles. Just outside the beam pipe the Vertex Detector is placed, consisting of multiple layers of silicon pixel detectors ensuring a high spatial resolution down to very small angles. It is surrounded by a large volume TPC which provides up to 224 precise measurements along the track of a charged particle.
The second key component of the ILD precision measurements is a highly granular calorimeter system enclosing the TPC. It consists of a silicon-tungsten based electromagnetic calorimeter (ECAL), followed by a somewhat coarser steel-scintillator hadronic calorimeter (HCAL) design. Both sampling calorimeters are using fine

grained readout techniques. The ECAL corresponds to ∼24 radiation lengths (X_0) and ∼0.8 nuclear interaction lengths (λ_I). The AHCAL at normal incidence covers a total depth of $5.5\,\lambda_I$. The calorimetric coverage is extended by a system of high precision, radiation hard, calorimetric detectors in the very forward region.
A large volume superconducting coil around the calorimeters creates a longitudinal B-field of nominal 3.5 Tesla. Finally, an iron yoke returns the magnetic flux and serves also as muon detector and tail catcher.

2.2 The Compact LInear Collider (CLIC)

Another possible design of an electron-positron linear collider in the post-LHC era for physics in the multi-TeV energy range is the Compact LInear Collider (CLIC) studied at CERN [4]. It aims for center-of-mass energies of$\sqrt{s} = 0.5 - 5\,\text{TeV}$, but is optimized for a nominal value of $\sqrt{s} = 3\,\text{TeV}$. Due to the higher beam energy range achievable, CLIC will become necessary, if the physics discoveries at the LHC are made in the multi-TeV range.
In order to reach this ambitious goal, the accelerating gradient has to be of the order of 100 MV/m which is not within reach when using superconducting cavities. Only room temperature traveling wave structures at a high frequency of 12 GHz are likely to achieve such a high gradient. To allow for a sufficient high RF power needed for this gradient, CLIC relies upon a *Two-Beam-Acceleration* concept. Both beams are generated in a central injector complex and transported along the linac. The RF power is extracted from the secondary beam, the so-called drive beam, for partial sections of the main linac. For a 3 TeV collider 24 of such low-energy, high-intensity electron drive-beams are needed to extract the power with special *Power Extraction and Transfer Structures* (PETS). Transferred to the high-energy, low-current main linac each of them provides enough power to accelerate the beam by another 62.5 GeV. Each unit contains 1491 PETS feeding twice as much accelerating structures. The overall layout of CLIC is sketched in figure 2.3.

The electrons are produced similar to the electron beam at the ILC by illuminating a Gallium arsenide cathode with a laser, situated in a high-voltage DC photo injector.
The described two-beam approach avoids the use of a large number of active RF elements, e.g. klystrons or modulators, in the main linac and eliminates therefore the need for a second tunnel. Including a ∼5.5 km long beam delivery system, CLIC would cover a total length of approximately 48 km.
There are two interaction points foreseen, one for e^+-e^- and one for γ-γ to study for example the Higgs mass. The main accelerator parameters of CLIC are listed in table 2.2.
Some of the suggested CLIC technologies still have to be proven feasible [14].

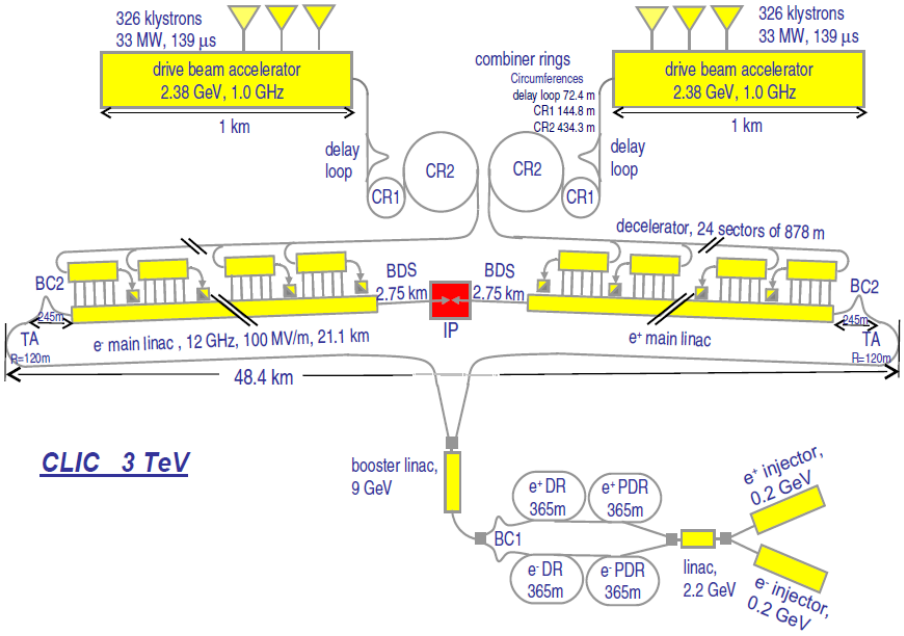

Figure 2.3: Schematic layout of the Compact Linear Collider at a center-of-mass energy of 3 TeV [13].

Parameter	**Value**	**Unit**
Main Beam Parameters		
Peak luminosity	$5.9{\cdot}10^{34}$	$\mathrm{cm}^{-2}\mathrm{s}^{-1}$
Pulse length	156	ns
Number of photons per electron	2.2	
Number of bunches per pulse	312	
Charge per bunch	0.9	nC
Typical beam size at IP (h×v)	45×1	nm
Beam power per beam	14	MW
Main Linac Parameters		
Center-of-mass energy	3	TeV
Repetition rate	50	Hz
RF frequency	12	GHz
Average accelerating gradient in cavity	100	MV/m
Active length per linac	10.74	km
Total two-linac length	42.16	km
Number of drive-beams per linac	24	
Length of beam delivery system	∼5.5	km
Total site length	∼48.4	km
Total AC power consumption	415	MW

Table 2.2: Main beam parameters of CLIC at 3 TeV center-of-mass energy [15].

3 Imaging Calorimetry

With a constantly increasing energy range at which particle accelerators operate, the role of calorimeters as cornerstones of the entire detector system is emphasized. Their hermetic coverage around the interaction vertex allows the detection of multi-particle events, called jets, as well as single particles. Calorimeters measure the properties, mainly the deposited energy, of subatomic particles by total absorption. Particles lose their energy via several interaction processes depending on their nature and the dense matter they cross. As a consequence of these interactions secondary particles are created that carry a certain energy fraction of the initial particle. This property is described by the so-called electromagnetic or hadronic shower development of a particle when traversing matter. The particle multiplication ends if the remaining energy of a particle is too small and it is completely absorbed. In the following the two types of such particle showers shall be described based on their respective formation processes.

3.1 Electromagnetic Showers

If the possible energy loss is based on the electromagnetic interaction as in case of charged leptons and photons, an electromagnetic shower develops.

Interactions of Charged Particles

The five main interactions are listed below:

- **Ionization and atomic excitation:** Moderately charged particles ionize the medium, if their energy is sufficient to release the atomic electrons from the Coulomb fields generated by the atomic nuclei. At lower energies charged particles are still able to excite atoms or molecules to higher energetic states. During de-excitation to the ground state photons are emitted which in turn can be detected by the calorimeter. If the wavelength of these photons is in the visible range, the process is called scintillation.
  The mean energy loss dE of a heavy particle with charge ze per path length dx is described at an accuracy of a few % between $0.1 \lesssim \beta\gamma \lesssim 1000$ by the Bethe-Bloch equation [16]:

$$-\left\langle \frac{dE}{dx} \right\rangle = Kz^2 \frac{Z}{A} \frac{1}{\beta^2} \left[\frac{1}{2} \ln \frac{2m_e c^2 \beta^2 \gamma^2 T_{max}}{I^2} - \beta^2 - \frac{\delta(\beta\gamma)}{2} \right]. \tag{3.1}$$

  It depends next to the mass Z, the atomic number A and the characteristic ionization constant I of the absorber material only on the velocity v ($\beta =$

$v/c,\ \gamma = 1/(1-\beta^2)$) of the particle. K substitutes for a constant term and T_{max} is the kinetic energy which can be transferred to a free electron in a single collision. With an increasing particle energy its electric field flattens and extends until it is partially screened by polarization of the medium. This *density effect* at high relativistic particle energies is described by the $\delta(\beta\gamma)$ function. Figure 3.1 shows the energy loss normalized to the material density for positive muons in copper as a function of $\beta\gamma$. Particles carrying an energy within the broad minimum of energy deposition at $\beta\gamma \approx 3-4$ are called minimum ionizing particles (MIP's). For energies outside this range corrections need to be applied.

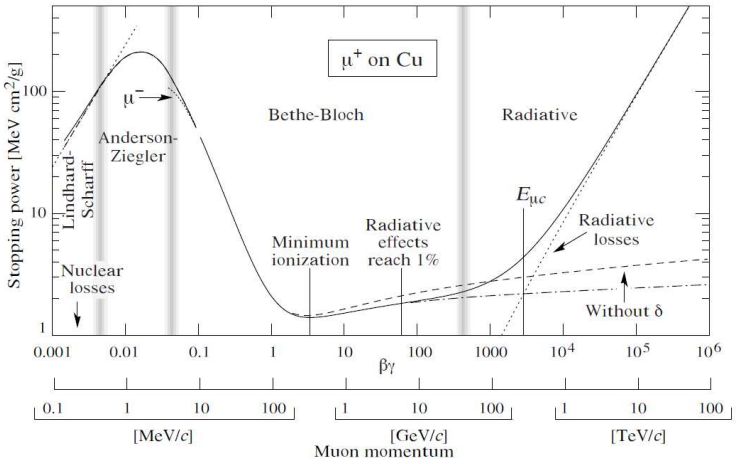

Figure 3.1: Stopping power for positive muons in copper [16].

- **Bremsstrahlung:** High energetic ($\beta\gamma \gtrsim 500$) charged particles can produce bremsstrahlung on their passage through matter. Electrons and positrons radiate photons as a result of the Coulomb interaction with the electric field generated by the atomic nuclei. The energy spectrum of those photons scales with 1/E. Since the energy loss of a particle with energy E and mass m is proportional to $\frac{E}{m^2}$ it dominates the other processes possible for electrons or positrons already at low energies of less than $\sim 100\,\mathrm{MeV}$. The energy loss through bremsstrahlung per unit path length dx is:

$$-\left[\frac{dE}{dx}\right]_{Brems} = \frac{E}{X_0}. \tag{3.2}$$

The radiation length X_0 is the mean distance after which the particle energy drops to 1/e of the initial energy.
For heavier particles it competes with the ionization process at much higher energies. The critical energy ϵ_c at which the ionization loss per radiation length X_0 equals the electron energy is:

$$-\left[\frac{dE}{dx}(\epsilon_c)\right]_{Brems} = -\left[\frac{dE}{dx}(\epsilon_c)\right]_{Ion},\ \text{with}\ -\left[\frac{dE}{dx}(\epsilon_c)\right]_{Brems} \approx \frac{E}{X_0} \tag{3.3}$$

- **Čerenkov effect:** If a charged particle travels faster than the phase speed of light $\frac{c}{n}$ in the dispersive medium of refractive index n traversed, it loses energy by emitting Čerenkov light. The reason for this radiation is an asymmetric polarization of excited atoms along the path of the particle (figure 3.2 (right)). The photons are radiated along a cone with the characteristic half-opening Čerenkov angle $\theta_C = \arccos(1/n\beta)$, relative to the direction of the particle (figure 3.2 (left)). The wavelength spectrum of the photons exhibits

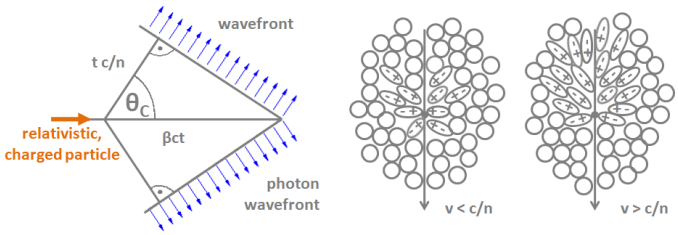

Figure 3.2: **Left:** Principle of the Čerenkov effect. **Right:** Polarization of the surrounding atoms.

  a characteristic $1/\lambda^2$ dependence, which causes mostly blue light within the visible wavelength range. The total contribution to the energy loss from the Čerenkov effect is minor compared to other processes as ionization (1 orders of magnitude less). A very important property of Čerenkov light is that it is instantaneously emitted without the delay through decay times as in the case of scintillation light.

- **Knock-on-electrons (δ rays) and nuclear reactions:** High energetic charged particles can transfer a much larger amount of energy than the ionization energy to an electron during a collision. The released high-energy e^- is called δ ray. At very high energies, the electromagnetic interactions may even induce nuclear reactions.

Interactions of Photons

An overview of the photon interactions in terms of their cross sections in lead is shown in figure 3.3. Included are the following effects:

- **Photoelectric effect:** This process dominates the energy loss of photons at low energies. The photons transfers its total energy to a bound electron of the absorber material. To fulfill the energy-momentum conservation the nucleus of the absorber atom is needed. The free electron carries the energy $E_e = E_{ph} - W$, which is equal to the transferred photon energy minus the energy needed to liberate the electron from its bound state (called work function).

- **Rayleigh scattering:** Another possible interaction at low energies is the Rayleigh scattering. The photons are elastically scattered by the atomic elec-

trons without an exchange of energy. Therefore, this process only affects the spatial distribution of the shower and not the energy deposition.

- **Compton scattering:** If an incident photon interacts with a weakly bound electron of the absorber atoms it can transfer parts of its energy and thereby free the electron. This effect dominates at higher energies of 0.1 - 10 MeV and the energy E_e of the liberated electron is:

$$E_e = h\nu \left(1 - \frac{1}{1 + \frac{h\nu}{m_e c^2}(1 - \cos\theta)} \right), \tag{3.4}$$

  where ν is the photon frequency and θ its scattering angle. The adopted energy of the freed electron is continuously distributed with a maximum for $\theta = 180°$ whereas in case of the photoelectric effect the accepted energy is quantized.

- **Pair production:** Photons with energies higher than twice the rest mass of an electron can create within the electric field of an electron or an atomic nuclei, electron-positron pairs. At high energies this process is the main source of energy loss of the photons and is described by

$$\lambda_{pair} = \frac{9}{7} X_0, \tag{3.5}$$

  where λ_{pair} is the mean free path of a photon for pair production.
  The probability for a high energetic photon to produce electron-positron pairs is therefore $1 - e^{-(\frac{7}{9} x/X_0)}$.

- **Photonuclear reactions:** At energies between 5 - 20 MeV photonuclear reactions, such as photo induced nuclear fission play a modest role ($\sigma_{g.d.r.} \sim 1\,\%$). This process is maximal when the photon energy is equal to the *marginal binding energy* of the proton or neutron (giant dipole resonance).

Figure 3.4 shows a simplified electromagnetic shower that starts with the described pair production process induced by a photon. The generated electron and positron radiate bremsstrahlung photons which in turn might decay into electron-positron pairs. One characteristic of electromagnetic cascades is the particle multiplicity. The multiplied particles and photons spread radially away from the direction of the incident photon until the energy of the radiated bremsstrahlung photons is too small to convert to further electron-positron pairs. The dimensions of an electromagnetic shower are described by two quantities, the radiation length X_0 and the Molière radius ρ_M. The former defines the longitudinal expansion as the distance after which electrons or positrons with energies » 1 GeV on average have lost $1 - 1/e = 63.2\,\%$ of their initial energy due to bremsstrahlung. The transvers propagation of the shower is given by the Molière radius in terms of the radiation length X_0:

$$\rho_M = 21.2\,\text{MeV} \cdot X_0/E_c \tag{3.6}$$

A cylinder of radius ρ_M around the shower axis contains about 90 % of the shower energy while inside $3.5\,\rho_M$ about 99 % is contained.

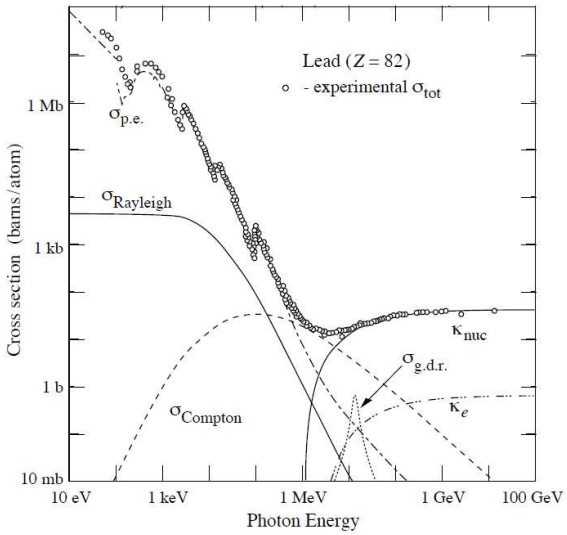

Figure 3.3: Cross sections of photon interactions in lead [16]. $\sigma_{p.e.}$: Photoelectric effect, $\sigma_{Rayleigh}$: Rayleigh scattering, $\sigma_{Compton}$: Compton scattering, $\kappa_{nuc./e}$: Pair production, $\sigma_{g.d.r.}$: Photonuclear reactions.

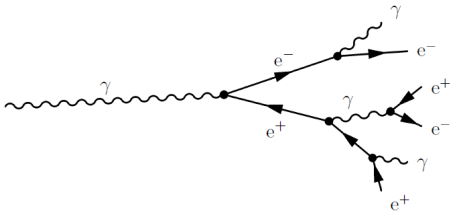

Figure 3.4: Schematics of an electromagnetic shower consisting of photons and electron-positron pairs.

3.2 Hadronic Showers

The interactions of neutral hadrons when traversing matter is based on the strong force. Charged hadrons on the contrary can interact via the strong and the electromagnetic force. This shower type is characterized by the large variety of possible processes and accordingly the amount of secondary particles produced. During this cascade of nuclear interactions, not only the incident particle but also the hit nucleus might get excited and change its identity. The fact that hadronic showers are subject to such large and hard to parametrize fluctuations complicates their description. Unlike in electromagnetic showers, where all energy is deposited in the absorber material and thus can be measured, in hadronic showers part of the dissipated energy exists in form of neutrons or neutrinos, which is undetectable for the calorimeter (*invisible energy*). This phenomenon leads to a hadronic calorimeter response which is smaller than the electromagnetic one and is partially responsible for the considerably worse energy resolution for hadronic shower detection. The shape of the two shower types is in principle similar, but hadronic showers are much broader and less

dense. The increase of the number of particles developed as a function of the shower length is approximately linear and decays less steep after reaching a maximum. A hadronic shower is statistically defined by the nuclear interaction length λ_{int} which gives the mean path length before a high-energy hadron interacts strongly with the traversed material. It is in general larger than the radiation length (e.g. for iron $\lambda_{int}/X_0 \approx 9.6$).
One more typical property of hadronic cascades is the inclusion of an electromagnetic component. This fraction originates from strongly interacting mesons producing neutral pions (π^0) or etas (η) whose decay photons initiate high-energy electromagnetic cascades (π^0,$\eta \to \gamma\gamma$). The varying fraction of the initial hadronic energy that is converted into π^0's and η's depends on the processes occurring during the early stages of the shower development. It increases with energy and was studied in great detail by [17]:

$$f_{\mathrm{em}} = 1 - \left(\frac{E}{E_0}\right)^{k-1}, \quad \text{with} \quad k-1 = \frac{\ln(1-f_{\pi^0})}{\ln < m >}, \tag{3.7}$$

where E_0 corresponds to the energy needed for the production of one pion and $k-1$ is related to the average multiplicity <m> (average number of mesons produced per interaction) and the average fraction f_{π^0} of π^0's produced within those reactions.
The hadronic calorimeter response in general, expressed in terms of f_{em}, is [18]:

$$R(f_{\mathrm{em}}) = f_{\mathrm{em}} + \frac{1}{e/h}(1 - f_{\mathrm{em}}), \tag{3.8}$$

with the nominal beam energy E and R = 1 describing a pure electromagnetic shower. The electromagnetic component (e) of a hadronic shower usually generates a larger signal per unit deposited energy in the calorimeter than the non-electromagnetic (h) does. This leads to e/h > 1, where the exact energy sharing between those two components is subject to large, non-Poissonian fluctuations. Several attempts are made to manage the resulting non-Gaussian response function, its non-linearity and the deviating energy resolution of the hadronic calorimeter from the $1/\sqrt{E}$ proportionality. Up to date *Compensating calorimeters* are designed where it is tried to reach $e/h = 1$ either by a precisely tuned sampling fraction [19] or by off-line compensation [20, 21]. Besides, the so-called *Energy Flow Method* [22] or the measurement of the electromagnetic shower fraction f_{em} event by event through the spatial shower profile (for single particles [23]) succeeded in achieving an improvement of the energy resolution of the hadronic calorimeter.

3.3 Sampling Calorimeters

There are different types of calorimeters for different needs of accelerator experiments. Two very common models are the homogeneous and the sampling calorimeter. In case of a homogeneous calorimeter, the entire detector volume is sensitive and thus contributing to the total signal produced. In a sampling calorimeter layer of two material types are alternated which perform either the function of particle absorption (passive material) or of signal generation (active material). For the passive layers a medium of high density, as iron or uranium, is chosen to contain most of the developing shower. The active medium is mainly made of light producing materials, as scintillator, which forms the basis for the signals from such a calorimeter. The energy fraction deposited inside the absorber layers can not be detected. Nevertheless, a high longitudinal and transverse resolution can only be reached with a sampling calorimeter.
An important parameter characterizing a sampling calorimeter is the *sampling fraction*, which is defined as the energy deposited by a MIP in the active calorimeter layers measured relative to the total energy deposited by that particle. Due to the wider expansion of hadronic showers and the larger λ_{int}, more and denser material is necessary to contain a similar shower fraction of a hadronic shower than of an electromagnetic shower.
The visible energy measured is proportional to the total energy of the shower, which therefore can be reconstructed. The relative energy resolution of a sampling calorimeter $\frac{\sigma_E}{E}$ is composed of several sources of fluctuations added in quadrature[1]:

$$\frac{\sigma_E}{E} = \frac{a}{\sqrt{E}} \oplus \frac{b}{E} \oplus c, \tag{3.9}$$

where E is given in GeV. The first term depends on statistical fluctuations following a Poisson distribution and scaling with $1/\sqrt{E}$. It includes signal fluctuations as the number of shower particles traversing the active layers (sampling fluctuations) and the efficiency in the conversion of photons into electrical signals. Furthermore variations of the invisible energy as well as differences in the track length and an asymmetric distribution of the energy deposition (Landau fluctuations) contributes to it. The fluctuation most important within the scope of this thesis which is affecting this term is the varying electromagnetic component of hadronic showers. The second factor describes the affect of instrumental effects as electronic noise or variations of the sampling fraction that scales with 1/E. The constant term c accounts for uncertainties in the calibration, non-uniformities and non-linearities of the calorimeter.

[1] $c = a \oplus b = \sqrt{a^2 + b^2}$

3.4 Particle Flow Approach

Many of the interesting physics processes will be characterized by multi-jet final states with jet energies between 150 - 350 GeV [7], accompanied by charged leptons and/or missing energy from neutrinos or light super symmetric particles. In the traditional calorimetric approach the achieved jet energy resolution (equation 3.9) depends on the energies deposited in the electromagnetic calorimeter (ECAL) and the hadronic one (HCAL).
Since one of the physics goals for ILC is a clean separation of W and Z hadronic decays ($\frac{\Gamma_W}{m_W} \approx \frac{\Gamma_Z}{m_Z} \approx \sigma_m/m = 2.7\,\%$), the stochastic term $a/\sqrt{E}$ must be at least $\lesssim 30\,\%/\sqrt{E}$ [7]. So far, energy resolutions approximately twice larger were reached at experiments like ALEPH $\sigma_E/E = 60\,\%/\sqrt{E}$ [22] or ATLAS $\sigma_E/E = 56\,\%/\sqrt{E}$ [24].

The developed *Particle Flow Approach* represents a sophisticated particle reconstruction and identification algorithm reaching the required jet energy resolution for beam energies of up to 500 GeV at a future linear collider.
It is based on the idea that an ultimate jet energy resolution can be achieved if every particle in the event, charged and neutral, is measured with the best possible precision. Therefore, charged particles are reconstructed in the tracking detectors, photons in the ECAL only and neutral hadrons in the combined calorimeter system of ECAL and HCAL. Ideally, a perfect separation of charged-particle clusters from neutral particle clusters in the calorimeters is achieved. This reconstruction algorithm requires an unprecedented high granularity of the calorimeter system.
In practice, such a detector performance can not be reached as it is impossible to perfectly reconstruct the four-vectors of all visible particles and assign the corresponding energy deposited by them. The occurring *confusion* places stringent requirements on the granularity of the calorimeters, implying that the final jet energy resolution is a combination of the intrinsic detector performance and the realization of the Particle Flow Approach. Figure 3.5 shows the reconstruction of a jet as it possibly will be observed at the ILD detector. The final jet energy resolution is composed of several terms:

$$\sigma_{jet} = f_c\sigma_{trk} \oplus f_\gamma\sigma_{ECAL} \oplus f_0\sigma_{HCAL} \oplus \sigma_{confusion}, \tag{3.10}$$

with f_x accounting for the total fraction of charged and neutral particles as well as photons generated in a jet. Measurements at LEP have shown that on average (but subject to large fluctuations) 62 % of the jet energy is carried by charged particles (mainly hadrons), around 27 % by photons, 10 % by neutral hadrons and approximately 1.5 % by neutrinos [25]. Assuming this jet composition, the HCAL featuring the worse energy resolution is used to measure only ∼10% of the energy conatined in a jet.
The first three components describe the respective energy resolutions originating from the tracker (σ_{trk}), the ECAL (σ_{ECAL}) and the HCAL (σ_{HCAL}). The confusion term accounts for events where the particle flow method does not succeed in a perfect disentanglement of overlaying jets or a correct assignment of single particles to

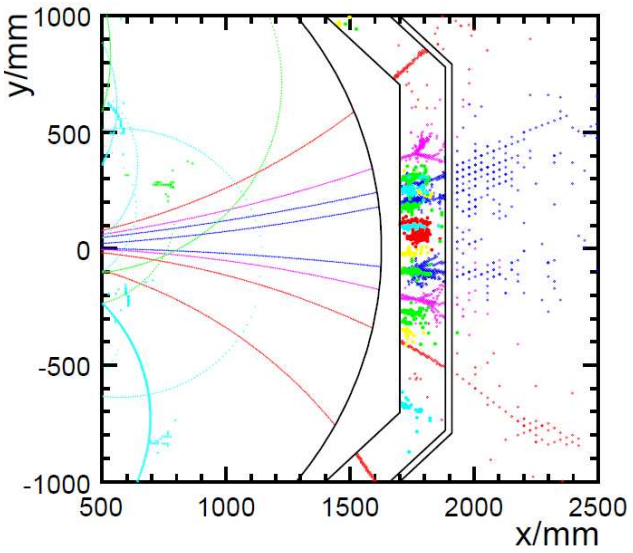

Figure 3.5: Particle flow reconstruction of a 100 GeV jet inside the ILD detector. The track coloring corresponds to the different energies of the reconstructed particles [7].

a cluster, for example. For higher jet energies and a higher density of overlapping clusters, $\sigma_{confusion}$ dominates the contribution to σ_{jet}.

3.5 Dual-Readout Calorimetry

In consideration of the fact, that the confusion term increases with higher jet energies it is not clear that the particle flow approach is suitable for energies in the multi-TeV range as at CLIC. One alternative approach to the particle flow approach is the *Dual-Readout Method* which is studied by the DREAM[2] collaboration [18, 26, 27]. It is proposed to achieve a higher energy resolution of the hadronic calorimeter by measuring the electromagnetic fraction f_{em} of a hadronic shower event by event.
A detector prototype was built with which a comparison of shower signals produced in the form of Čerenkov and scintillation light is possible. Only the electromagnetic fraction of a hadron shower registers in the former material, whereas the non-electromagnetic component, consisting of spallation and recoil protons, is typically not sufficiently relativistic to produce Čerenkov light. The developed DREAM detector consists of 2 m long, $4\times4\,mm^2$ copper rods, which were equipped with a hollow, central cylinder of 2.5 mm diameter to make room for seven optical fibers (figure 3.6). Three of those fibers produce scintillation light for every charged shower particle that crosses them, the other four are *Čerenkov fibers*, made of either high purity quartz or acrylic plastic, that give almost exclusively a response signal if they are traversed by charged particles traveling faster than the local speed of light.

[2] **D**ual **REA**dout **M**ethod

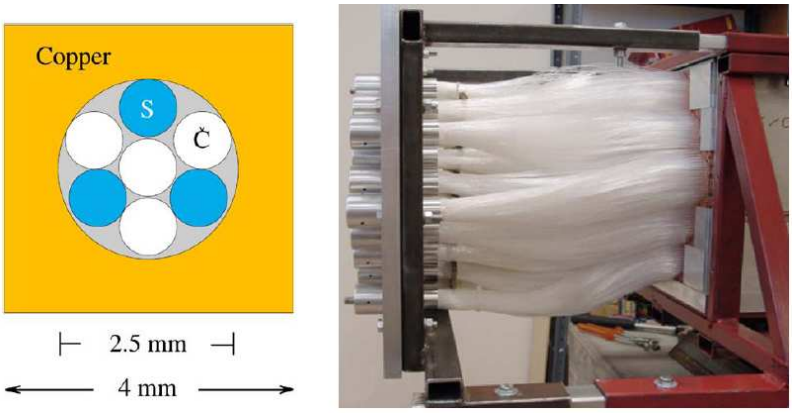

Figure 3.6: **Left:** Basic layout of one of the copper rods of the DREAM detector equipped with optical fibers. The Čerenkov fibers are colored in white, the scintillating fibers in blue. **Right:** Fiber bunches exiting from the rear face of the DREAM detector [18].

Comparing the signals of both fiber types therefore is a measure for the electromagnetic fraction carried by π^0's and η's to the total energy deposited in the calorimeter. The e/h ratio depends on the amount of passive and active calorimeter material as well as on the sampling fraction. In case of the DREAM detector e/h is 4.7 for the copper/quartz fibers and e/h = 1.3 for the copper/plastic-scintillator structure [28]. Therefore, the simultaneous measurement of the two signal types provides complementary information and allows for the improvement of the calorimeter performance. In figure 3.7 the DREAM principle is illustrated for a 100 GeV π^- run. The correlation between the Čerenkov (Q) and the scintillator (S) signals is depicted by single dots representing single events. The fact that the dots do not cluster around the line Q/S = 1 verifies the complementary content those two signal types provide.

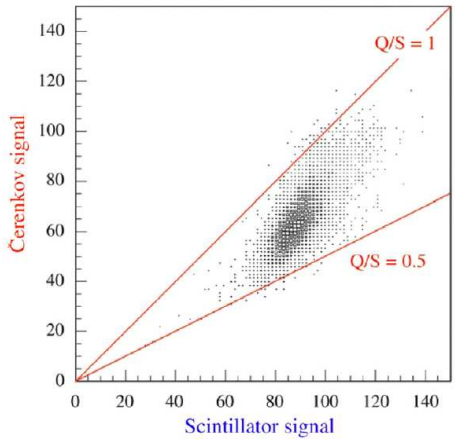

Figure 3.7: Correlation of the Čerenkov (Q) and the scintillator (S) signals of the DREAM calorimeter for 100 GeV π^- mesons [18].

There are several ways to combine those two signals, where one is the energy independent ratio of Q/S which is directly related to f_{em} (using equation 3.8):

$$\frac{Q}{S} = \frac{f_{em} + (h/e)_Q(1 - f_{em})}{f_{em} + (h/e)_S(1 - f_{em})}. \tag{3.11}$$

The fact that the values for Q/S shown in figure 3.7 are almost always < 1 with a mean value of 0.78, indicates that typically ∼22 % of the scintillator signal is caused by non-relativistic particles (protons from spallation or elastic neutron scattering). A measurement of this ratio, assuming the knowledge of the e/h values, provides directly the value of f_{em}.
The advantage of using an energy reconstruction method based on the ratio of Q/S is the jet energy independence it features. Nevertheless it suffers from event-to-event fluctuations of the shower leakage, which directly effect the value of f_{em} as can be seen in figure 3.8a. Since the DREAM calorimeter was too small to fully contain the hadron showers, the value of f_{em} was subject to uncertainties as indicated by the dotted lines (e.g. 10±5 % leakage). Using the measured Q/S value and thus

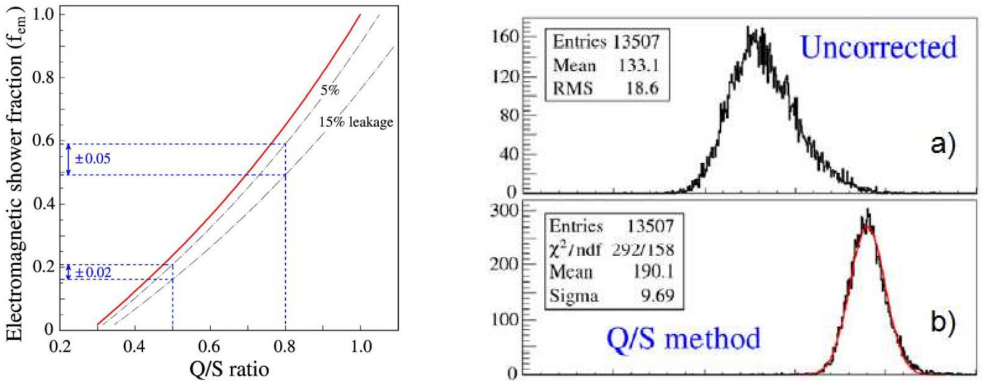

(a) (b)

Figure 3.8: **a:** Relationship between f_{em} and the measured Q/S signal ratio including uncertainties in case of a shower leakage of 10±5 %. **b:** Čerenkov signal distribution for a 200 GeV jet in the DREAM detector before (a) and after the Q/S correction (b) [18].

knowing the value of f_{em}, corrections for the effects of non-compensation are applied to the scintillator signal with the following formula:

$$\frac{S_{\text{final}}}{S_{\text{corr}}} = \frac{e/h}{1 + e/h \cdot f_{em} - f_{em}}, \tag{3.12}$$

where S_{corr} is the leakage-corrected scintillator signal. This equation is obtained by fitting a linear function to the leakage-corrected scintillator signal versus f_{em}. In figure 3.8b one can see, that the energy resolution increased from 14 % in case of the uncorrected jet signal distribution to 5 %, if the Q/S correction is applied to

the Čerenkov channel. This proves that even without knowing the nominal beam energy sufficiently good energy resolutions can be achieved. The signal distributions become more symmetric, deviations from the $1/\sqrt{E}$ scaling are largely eliminated and the hadronic signal response is linear (figure 3.9).
Using this method, the jet energy resolution is finally improved to $\sigma/E = \frac{64\,\%}{\sqrt{E}} + 0.6\,\%$ and the energy resolution for single pions increases to $\frac{41\,\%}{\sqrt{E}} + 4.2\,\%$ [18].
Further investigations are made to reduce leakage fluctuations, fluctuations in the Čerenkov light yield and sampling fluctuations by building a homogeneous DREAM calorimeter. For this purpose molybdenum doped $PbWO_4$ or BGO crystals are used, exploiting the different time structures of scintillation and Čerenkov light [28, 29].

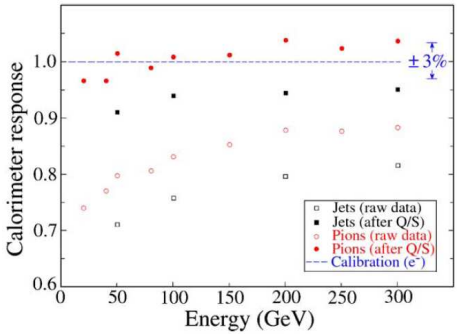

Figure 3.9: Scintillator response before and after the Q/S correction was applied to single pions and high-multiplicity jets [18].

3.6 Combination of Particle Flow with the Dual-Readout Method

There is no reason why the DREAM principles should be limited to fiber or homogeneous detector structures. One common feature of such calorimeter systems is the missing longitudinal segmentation, which makes the use of the particle flow method impossible.
A combination of particle flow with the dual-readout calorimetry would benefit from both approaches. The fast Čerenkov signal additionally would offer the needed environment to time tag single events of the complex CLIC bunch structure.
There are various ways in which such a calorimeter could be realized. One approach could be to use an active medium which generates both scintillation and Čerenkov light. To readout the two signals separately their different time structure can be used (scintillation light is isotropic and time-delayed whereas Čerenkov light is directional and instantaneously) or different photodetectors can be installed which are sensitive to the their characteristic wavelength regions.
Another option could be to develop a highly granular hadronic calorimeter not only using active layers made of a scintillating material, but also of a second active material generating Čerenkov light. This way the power of the particle flow approach

based on high granularity would be sustained and by measuring f_{em} eventwise the energy resolution of neutral hadrons could be improved further. On the other hand, for events in the multi-TeV energy regime were the particle flow approach might fail due to the dominating confusion term, the calorimeter energy resolution can be significantly improved by the dual-readout information. A possible hadronic calorimeter layout for the latter proposal is sketched in figure 3.10. A hadronic

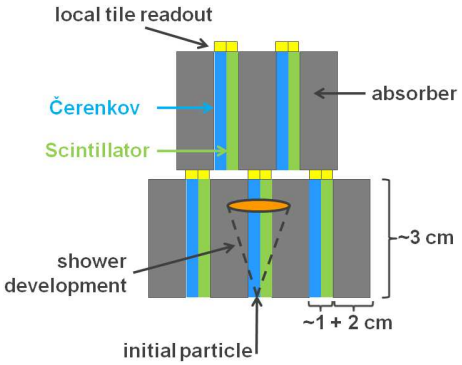

Figure 3.10: Possible calorimeter layout suitable for a combination of the particle flow and the dual readout method.

shower developing in the calorimeter would generate highly resolved spatial signals in the longitudinal and lateral direction, where only its electromagnetic component would leave tracks in the Čerenkov channels. The dimensions of the single calorimeter cells would have to match the optimal cell size found for a calorimeter suitable for particle flow ($\mathcal{O}(3\times3\times1\,\mathrm{cm}^3)$) [8]. Furthermore both active materials need to sample the same shower fraction and thus need to be installed together in every single cell. The subsequent segmentation layers have to be staggered to maximize the material density along the shower development and to avoid events where the initial particle only crosses one of the three materials (absorber or one of the active layers).

For a realization of this concept materials featuring suitable properties have to be found and an efficient light readout mechanism has to be established. In case of the Čerenkov light producing material it is crucial that its transmission probability is high particularly in the UV wavelength region. Furthermore its density and index of refraction should be sufficiently high to produce as many Čerenkov photons as possible to achieve a sufficient Čerenkov light yield. This consequentially demands a high efficiency of the light readout mechanism. Newly developed, very compact and high gain photomultiplier devices, so-called Silicon Photomultipliers (SiPM), could fulfill those requirements. The produced light can be readout directly from the single tiles reducing the loss of Čerenkov photons to a minimum. The size of those tiles suitable for particle flow is of some cm. However, the feasibility of Čerenkov light readout from small tiles is not proven yet. Only a few studies are available on the readout of Čerenkov light produced within tiles of a comparable size [30, 31].

To study the achievable Čerenkov light yield obtained from small tiles suitable for the particle flow calorimetry was the assigned task for this thesis. Different materials, tile shapes and mounting positions of the SiPM were tested in order to find the optimal constellation.

4 Silicon Photomultiplier

The different kinds of light detectors range from vacuum Photomultiplier Tubes (PMT's) to Semiconductor Detectors as the Avalanche Photodiode (APD's) is one. All of them amplify an optical current of incident light in a way that makes the detection of individual photons possible. With the latest design, the *Silicon Photomultiplier* (SiPM), the field of photon detection has experienced considerable progress. The SiPM uses parts of earlier developments combined with new convincing features. It is insensitive to magnetic fields and its size is in the range of some millimeters, which allows an implementation directly inside modern particle detectors. Furthermore, they are operated at a bias voltage that is approximately two orders of magnitude smaller than the one of common PMT's, but nevertheless are able to reach a similar gain factor of 10^5-10^6. This chapter shall give a theoretical overview of the main properties of the SiPM. For a detailed review, the reader is referred to [32, 33]. The measurements made to characterize the installed SiPM's can be found at the end of this chapter.

4.1 Working Principle

Like every other semiconductor based photodetector, a SiPM is operated in Geiger mode. It consists of an array of single pixels each designed as a Geiger mode Avalanche Photodiode (GAPD) and acting as an individual single photon counter. The pixels have to be isolated from each other which creates non-sensitive areas. The SiPM depicted in figure 4.1 joins 400 pixels over an area of $1\times1\,\mathrm{mm}^2$ on a common substrate. All pixels are connected to the same bias voltage by aluminum tracks.
If an APD is operated in Geiger mode, a reverse voltage higher than the breakdown-voltage is applied to the device. A high electric field of typically $\sim10^5\,\mathrm{V/cm}$ is produced between the few micrometer thin p^+-doped and n^+-doped layers of the pn-junction. Incident photons are absorbed there and generate electron-hole pairs. Both, electrons and holes are accelerated towards opposite ends of the depletion region. Via the so-called process of impact ionization secondary electrons and/or holes are produced, if the charge carriers gained enough energy from the electric field in-between two interactions to excite an additional electron from the bound state to the conduction band. Therefore, an electron drifting from the low resistive p^--doped layer into the depletion region will trigger an avalanche breakdown, called Geiger discharge. In case of a Silicon Photomultiplier this procedure is referred to as "firing of a pixel". The formed output signal of one pixel is independent of the number of initially absorbed photons. Accordingly, the analog signal response of

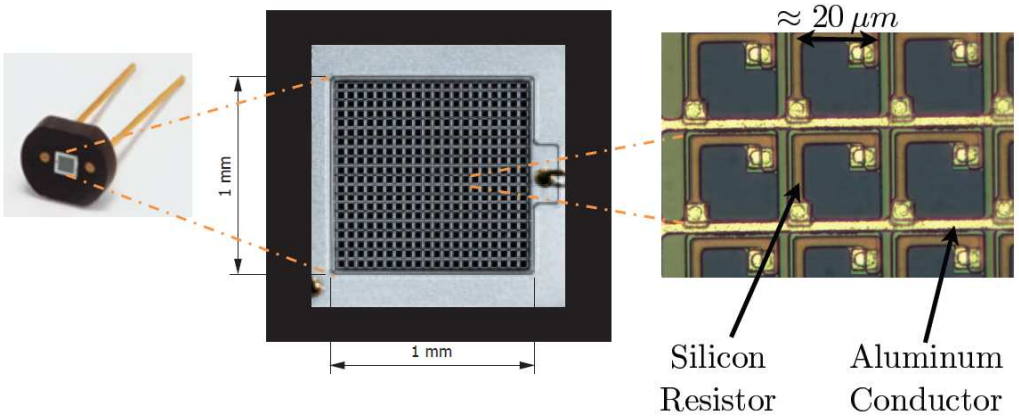

Figure 4.1: **Left:** SiPM produced by *HAMAMATSU Photonics K.K.*, Japan [34]. **Middle:** Photograph of the $1\times1\,\mathrm{mm}^2$ large sensitive surface. **Right:** Microscopic picture of the single pixels [35].

the entire SiPM corresponds to the number of pixels fired. The dynamic range of a SiPM is limited by the total number of installed pixels. If the SiPM is illuminated by only a small light flux compared to the total number of pixels, the number of pixels fired corresponds approximately to the number of incident photoelectrons. Else the SiPM signal goes into saturation. The pixel layout is illustrated in figure 4.2 (left).
The two guard rings made of n^--doped material reduce the electric field close to the edge of the pixel, where impurities could lead to unwanted discharges.
For voltages well above breakdown the avalanche sustains itself and thus has to be "quenched" by the built-in silicon resistor on the pixel surface. The breakdown current causes a voltage drop over this quenching resistor R_{quench} ($\approx$ hundreds kΩ to a few MΩ) that reduces the effective voltage below breakdown and the avalanche dies out.

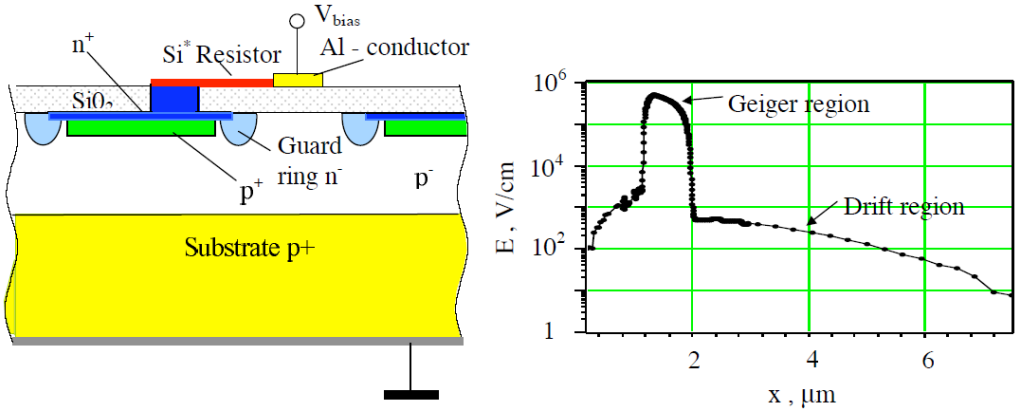

Figure 4.2: **Left:** Working Principle and topology of a single pixel of a SiPM. **Right:** Electric field profile in a SiPM [32].

The recovery time τ of a pixel defines the time span between a Geiger discharge and the complete recreation of the electric field. If C_{pix} is the single pixel capacitance (typically $\approx$ 20 - 300 fF), determined by the pixel geometry and the doping of the semiconductor material, τ is:

$$\tau = C_{pix} \cdot R_{quench}. \tag{4.1}$$

Gain and Signal Response

The gain is defined as the number of secondary electron-hole pairs generated in the discharge cascade. In case of silicon the ionization coefficient $\alpha\,[\mathrm{m}^{-1}]$ is larger for electrons than for holes, which is why only electron can induce breakdown avalanches [36]. The typical gain of SiPM's is of the order of 10^5 to 10^6 comparable to the gain of a PMT.
The gain G is determined by the total charge Q_{pix} released by a firing pixel divided by the elementary charge q_e:

$$G = \frac{Q_{pix}}{q_e}, \quad \text{with } Q_{pix} = C_{pix} \cdot (U_{bias} - U_b). \tag{4.2}$$

The difference between the applied bias voltage U_{bias} and the breakdown-voltage U_b is the over-voltage U_{over}. The pixel capacitance should not be too large and the voltage as stable as possible to reduce gain fluctuations.
Figure 4.3 shows the gain for a constant breakdown-voltage and varying bias voltage. The gain stays constant at 1 for as long as the bias voltage is considerably smaller

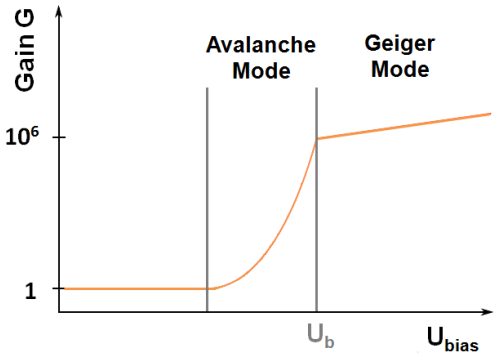

Figure 4.3: Voltage dependence of the SiPM gain.

than the breakdown-voltage, but increases quickly for larger bias voltages close to U_b. As soon as U_{bias} exceeds U_b the device is in Geiger mode and the gain reaches values of $\sim 10^6$. Within this region its gain factor increases linearly with the applied voltage. This results in an absolute and a relative gain-voltage dependency using equations 4.2:

$$\frac{dG}{dU} = \frac{C_{pix}}{q_e} \quad \text{and} \quad \frac{1}{G}\frac{dG}{dU} = \frac{1}{(U_{bias} - U_b)}. \tag{4.3}$$

Since the voltage-temperature dependence of the breakdown-voltage is determined to be $\frac{dU_b}{dT} = 56.0 \pm 0.1 \frac{mV}{K}$ [34], cooling down the SiPM increases the gain. This leads to a voltage-temperature dependence of the gain of:

$$\frac{dG}{dT} = (-\frac{U_b}{dT}) \cdot \frac{dG}{dU}. \tag{4.4}$$

To obtain the same dependencies for the signal response A of a single-photoelectron detector operated in Geiger mode, the photon detection efficiency ϵ has to be taken into account (see next section). The signal amplitude A is the product of gain G and ϵ yielding as final voltage and temperature dependencies:

$$\frac{1}{A}\frac{dA}{dU} = \frac{1}{G}\frac{dG}{dU} + \frac{1}{d\epsilon}\frac{d\epsilon}{dU}, \tag{4.5}$$

and

$$\frac{1}{A}\frac{dA}{dT} = \frac{1}{G}\frac{dG}{dT} + \frac{1}{d\epsilon}\frac{d\epsilon}{dT} = (-3.7 \pm 1.1 \frac{\%}{K})[37]. \tag{4.6}$$

A detailed description of these dependencies can be found in [38]. The quoted value of the temperature dependency of the signal response is used for temperature corrections of data taken during this thesis.

Dark Rate, Afterpulses and Optical Cross-Talk

There are several processes that influence or even falsify the measured optical signal. One of them the mean dark current or mean dark count rate accounts for the fact, that even if no light is present, charge carriers can be produced, that induce Geiger discharges. This is caused either by thermal excitation of an electron to intermediate energy states or by the quantum-mechanical phenomenon of "tunneling" through the band gap of the semiconductor. Whereas the first unwanted effect can be reduced by cooling the SiPM, the second depends on the high electric field within the depletion region that can not be reduced. Typical values of the dark rate range from 100 kHz to a few MHz.
Another process influencing the analog SiPM signal is the so-called afterpulse. Thereby some of the carriers during avalanche breakdown are trapped by impurity states and are released time-delayed. If this time interval is longer than the recovery time of the pixel, this results in an additional, delayed Geiger discharge.
The last process is based on the production of photons during avalanche breakdown. It has been shown in [39], that the emission efficiency of photons with energies higher than 1.14 eV is about $3{\cdot}10^{-5}$ photons per charge carrier. This corresponds to approximately 30 photons per avalanche which might carry an energy, that is high enough to traverse the border between two neighboring pixels, inducing a Geiger discharge in the adjacent pixel. This effect, often called optical cross-talk, misleadingly increases the measured signal of the SiPM (figure 4.4).

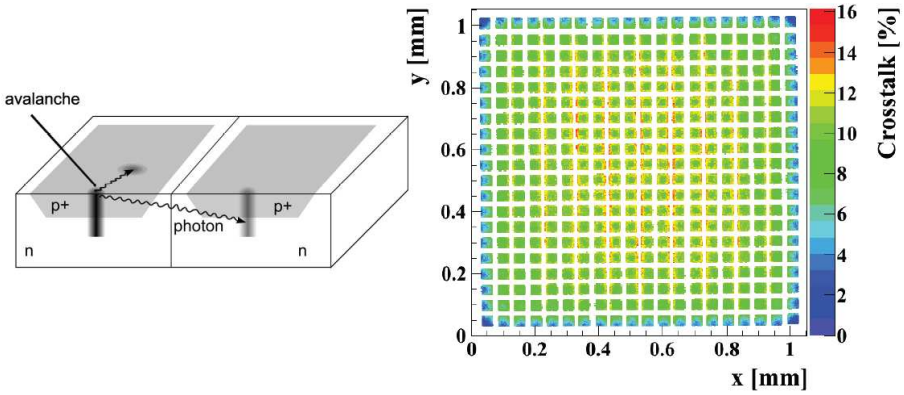

Figure 4.4: **Left:**Principle of optical cross-talk. **Right:**Measured inter-pixel cross-talk for the example SiPM shown at the beginning of this chapter [40].

Photon Detection Efficiency

The photon detection efficiency (PDE) is a measure of how many incident photons are effectively detected by the SiPM. Not all carriers generated by the incident photons produce a signal large enough to be detected. The PDE is determined by the wavelength depending quantum efficiency ϵ_{QE} of the photodetector. It corresponds to the probability that a photon traversing the depletion region of the pixel is absorbed and generates an electron-hole pair. For SiPM's an additional geometrical efficiency ϵ_{Geom}, also called fill-factor, has to be included as only part of the total pixel area is also sensitive to photon detection. By producing SiPM's with less but larger pixels the fill factor can be improved. This would increase the PDE but simultaneously reduce the dynamic range of the SiPM. The last factor is the Geiger efficiency ϵ^{Geiger} which depends on the incidence position of the photon and on the applied bias voltage. It gives the probability that an electron or a hole, passing through the depletion region, initiates a Geiger discharge. Therefore, the PDE is:

$$\epsilon = \epsilon_{QE} \cdot \epsilon_{Geom} \cdot \epsilon_{Geiger} \tag{4.7}$$

Most SiPM's are optimized for light in the green or blue wavelength region and reach a peak PDE of ∼50% if cross-talk and afterpulses are included [34].

4.2 SiPM Characterization

In order to determine the light yield measured with a SiPM two quantities need to be measured in advance: the intrinsic gain of the device and its breakdown-voltage. The first has to be known for the conversion of the signal amplitude measured in QDC-channels into the number of photoelectrons and the second influences the absolute height of the PDE.

The two SiPM's used for the light detection are both produced by Hamamatsu[1].

[1]Hamamatsu Photonics K.K., Solid State Division, Japan

The so-called *Multi-Pixel Photon Counter* (MPPC[2]) by Hamamatsu features excellent photo detection capabilities as well as all other advantages of a SiPM. A detailed characterization of different MPPC types can be found in [41]. Table 4.1 lists the major characteristics of the two MPPC types used and figure 4.5 depicts the PDE as provided by the producer.

	S10362-11-050C	**S10362-33-050C**
Active Area [mm^2]	1×1	3×3
Pixel Size [μm^2]	50×50	50×50
Number of Pixels	400	3600
Fill Factor [%]	61.5	61.5
Spectral Response Range [nm]	320 - 920	320 - 920
Peak Wavelength [nm]	440	440
Dark Count [kHz]	400	6000
Terminal Capacitance [pF]	35	320
Gain	$7.5{\cdot}10^5$	$7.5{\cdot}10^5$

Table 4.1: Typical quantities of the two MPPC types used as quoted in the provided datasheets of Hamamatsu [34].

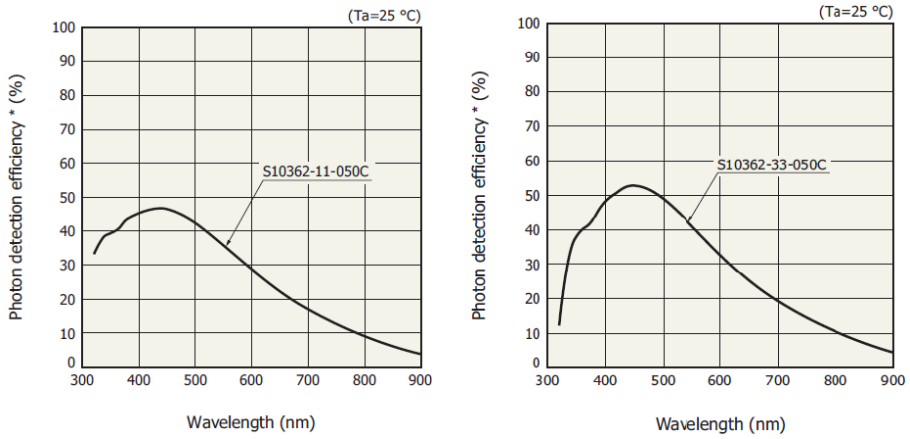

Figure 4.5: Photon Detection Efficiency for the two MPPC's used for the measurements presented in this thesis. Optical cross-talk and afterpulses are included [34].

The MPPC of the type S10362-33-050C was chosen for the detection of Čerenkov photons, since it features a large sensitive surface. The probability to detect a Čerenkov photon is therefore higher. The other MPPC (S10362-11-050C) is used to readout the scintillator tile as it provides a very low noise rate and a higher PDE.

[2]From now on the term MPPC will be used and no longer the abbreviation SiPM.

Laboratory Measurements

A laboratory setup was built to measure the gain G and the breakdown-voltage U_b of each MPPC. The MPPC itself was placed inside a lightproof box. A blue LED was used as light source, installed inside a second light-tight box well screened from the MPPC and triggered by a pulse generator. Light pulses with a length of a few ns are guided from the LED to the sensitive surface of the MPPC by a coated fiber bundle. The light intensity was adjusted by tuning the LED voltage ($\sim$3 V) such that only a very small number of photons ($\mathcal{O}(5)$) arrived at the sensitive surface of the MPPC per light pulse. The electronic readout chain shown in figure 4.6 was used for both MPPC's.

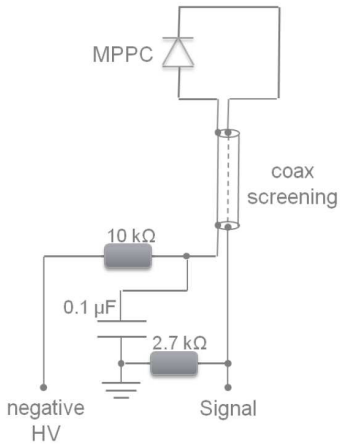

Figure 4.6: Basic scheme of the electronic operation circuit for each MPPC.

The MPPC cathode is connected to the signal output and the anode through a 10 kΩ resistor with a negative voltage of roughly 70 V. This resistor limits the voltage drop at the SiPM during breakdown. The 2.7 kΩ resistor converts the optical current generated by a photon hitting the sensitive surface of the MPPC into a voltage signal at the output. The capacitor of 0.1 μF is decoupling the signal and provides the needed charge when the MPPC is in breakdown [42]. The detected signal was amplified by a factor of 50 using a fast preamplifier to be able to resolve the single photoelectron peaks. The signals were integrated with a Charge-to-Digital Converter over a time window of $\sim$100 ns.

MPPC S10362-33-050C The figure 4.7 shows the single photoelectron spectrum as it is obtained with the above described setup for a bias voltage of -71 V. The first peak, called pedestal, contains events where only electronic noise was integrated by the QDC. A Gaussian distribution was fitted to the peak yielding a mean amplitude of $A^{Ped} = 47.9$ QDC-channels and a width of $\sigma_{Ped} = 4.01$ QDC-channels. The adjacent peaks to the right of the pedestal represent the detected signal of one or more photoelectrons (p.e.). From the distance between two neighboring peaks, the gain G[QDC-ch.] of the MPPC can be calculated. In units of the elementary

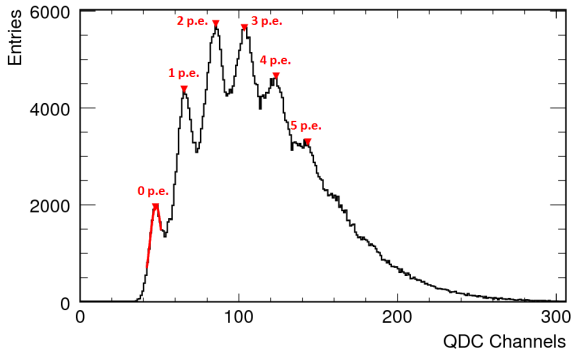

Figure 4.7: Single photoelectron spectrum as obtained with the MPPC responsible for the Čerenkov light readout.

electron charge q_e it is:

$$G[q_e] = \frac{G[\text{QDC-ch.}] \cdot C_{QDC}}{k \cdot q_e}, \tag{4.8}$$

with $G[\text{QDC-ch.}] = 19.64$ QDC-channels, a QDC conversion factor C_{QDC} of 250 fC/QDC-channel and a pre-amplification factor $k \approx 50$ for the laboratory setup. This results in a measured MPPC gain of $G[q_e] = 6.14 \cdot 10^5$.
During test beam measurements that will be described in the next chapter no amplifier will be used ($k = 1$). The QDC at test beam (TB) features a 10 times smaller conversion factor of $C_{QDC}^{TB} = 25$ fC/QDC-channel compared to the device in the laboratory. Therefore $G[\text{QDC-ch.}]$ has to be divided by a factor of 5. A final value of $G[\text{QDC-ch.}] = 3.93$ QDC-channels is used to obtain the measured light yield LY in terms of photoelectrons per minimum ionizing particle (MIP) at test beam:

$$\text{LY [p.e./MIP]} = \frac{A^{Sig} - A^{Ped}[\text{QDC-ch.}]}{G[\text{QDC-ch.}]}, \tag{4.9}$$

where A^{Sig} is the measured signal amplitude.
The breakdown-voltage was determined by measuring the gain as a function of the applied bias voltage (figure 4.8). The data points are fitted with a straight line and interpolated to $G = 0$ to determine U_b. The found value of $U_b = -70.1$ V implies that the MPPC is operated at $\sim$1 V overvoltage.

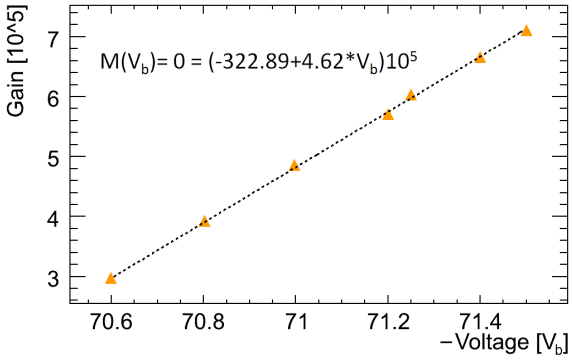

Figure 4.8: Measurement of the breakdown-voltage of the MPPC S10362-33-050C used for the Čerenkov light readout.

MPPC S10362-11-050C Following the same procedure as described above a single photoelectron spectrum was recorded of the second MPPC (figure 4.9). The breakdown-voltage was determined to be $V_b \cong -69.8\,\mathrm{V}$ which accounts for an overvoltage of 1 V at a bias voltage of -70.8 V. The mean value of the pedestal is found

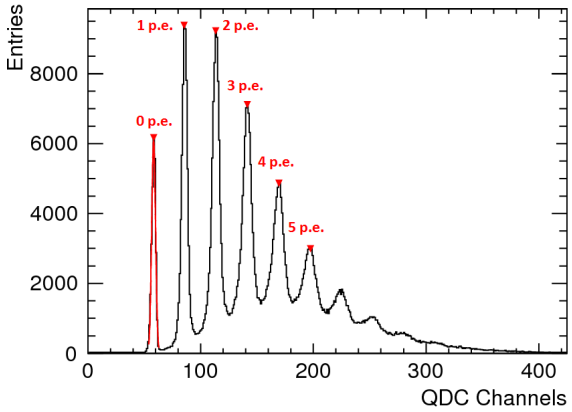

Figure 4.9: Single photoelectron spectrum of the MPPC used for scintillation light readout.

to be at 58.3 QDC-channels with $\sigma_{Ped} = 1.7$ QDC-channels. The lower dark noise rate of this MPPC becomes apparent in the smaller peak widths leading to a sharp separation of the individual peaks. The spectrum yields a mean peak-to-peak distance of 27.9 QDC-channels which corresponds to $G[\mathrm{q}_e] = 8.71 \cdot 10^5$. A final value of $G[\text{QDC-ch.}] = 5.58$ QDC-channels is used for the test beam analysis of the measured light yield.

5 Čerenkov Light Measurements

Indispensable if using particle flow, is a high granularity of the calorimeter system. The additionally integrated active layers made of a Čerenkov light producing material have to feature a similar granularity as the active layers made of a scintillator material. The number of produced and thus the number of detectable Čerenkov photons depends on the amount of material crossed by the relativistic charged particle. Considering the optimized tile size for PFA, Čerenkov tile sizes of a few centimeters are reasonable. For the readout of every single calorimeter cell a MPPC will be directly coupled to the tiles. This reduces the loss of Čerenkov photons of the expected low light yield to a minimum. So far it is not clear, if a sufficiently high Čerenkov light yield is achievable in such small tiles that can be measured with the noise sensitive MPPC's.
An experimental test setup was built to study the Čerenkov light yield distributions measurable with MPPC's. To find the optimal constellation yielding the highest number of detected Čerenkov photons and the most uniform tile response, two different dispersive media, two differing tile shapes and MPPC readout positions were examined. As a reference signal a scintillator tile was readout simultaneously with the Čerenkov tile. The scintillator features a higher light yield sensitive to temperature and noise fluctuations. It thus offers the possibility to monitor the system stability and accomplish a reasonable error estimation of the Čerenkov signal.
The setup for these measurements will be described in detail in this chapter.

5.1 Experimental Setup

All data taken for this thesis were collected at beam line 21 of the DESY test beam facility. A more detailed description of the beam generation can be found in the appendix (see section 10.1).
In figure 5.1 the experimental setup is drafted. The positron beam with energies of 2 - 3 GeV arrives from the left. For data acquisition a trigger mechanism is installed requiring a coincidence signal of two perpendicularly aligned scintillator counters. From the number of coincidences the beam rate is determined. The trigger is mounted on a movable stage in order to align the trigger cross to the beam center. The actual experimental setup is placed about 30 cm behind the trigger stand. It is installed on a second translation stage, movable from inside the control room while the beam is switched on. A systematic uncertainty of ± 0.5 mm concerning the accuracy of one particular stage position is estimated. On top of this translation stage a steel box is mounted containing the scintillator and Čerenkov tile as well as the electronic readout circuits for both MPPC signals which are powered by the

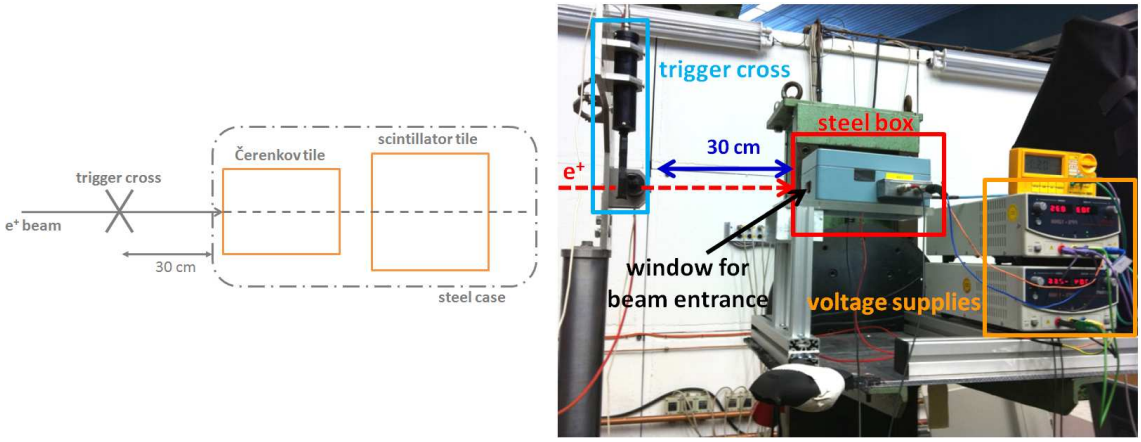

Figure 5.1: **Left:** Sketch of the experimental setup. **Right:** Picture of the test stand with voltage supplies and steel box containing the tiles samples. The trigger cross can be seen on the left.

respective voltage supplies visible on the right in the photograph.
While shape and readout position of the scintillator tile were the same for all measurements, the impact of different Čerenkov tiles and readout positions of its MPPC were studied concerning the achievable light yield and the uniformity of the tile response.
The approaching positrons enter the steel box through a small window in the wall and traverse the Čerenkov and the scintillator tile. Assuming that the active material layer is thin enough and of low-density the positrons behave approximately as minimum ionizing particles.
Within the next two sections an overview of the operation mechanism of the trigger and the signal readout is given as well as a description of the installation of the two tiles inside the steel box.

5.2 Trigger Mechanism and Signal Readout

The readout was triggered by requiring coincident signals from two perpendicular scintillator counters with a size of $10\times1\times0.5\,\mathrm{cm}^3$ each. To be able to scan the tile's front surface with the beam, the trigger cross section was chosen to be as small as $0.5\times0.5\,\mathrm{cm}^2$. For the readout of the trigger signals a photomultiplier tube was mounted at the rear back of each scintillator counter driven at $\sim$1700 V.
The triggered event rate measured as a function of the energy can be seen in figure 5.2. The maximum rate of roughly 4.6 kHz is achieved at a beam energy of 2 GeV. The rate decreases to $\sim$0.08 kHz for energies around 6 GeV.

Crucial for the success of the measurements was a very low noise environment since small optical signals should be detected with a reasonable MPPC signal-to-noise level. For this purpose the steel box was isolated via a 1.5 cm thick plastic plate from the test stand and all electronic devices were connected to the same ground

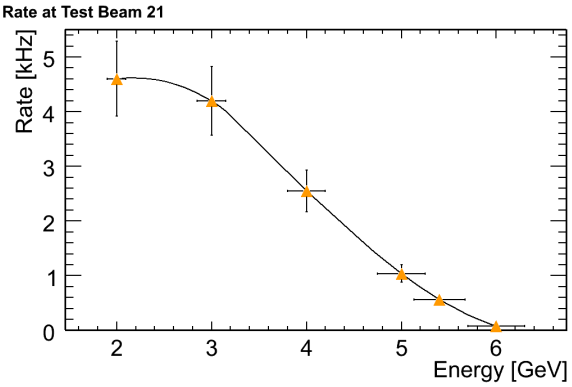

Figure 5.2: Measured test beam rates as a function of the beam energy. A 15 % error is assumed and applied to the rate due to scaling uncertainties.

level. The lightproof box was covered in addition with a thick black tissue.
A sketch of the installed electronic readout chain is displayed in figure 5.3. A negative bias voltage is applied to each of the MPPC's. Both voltages lie about 1 Volt above the breakdown voltage, which results in $U_{bias} = -70.8\,\mathrm{V}$ for the MPPC coupled to the scintillator and $U_{bias} = -71.0\,\mathrm{V}$ for the readout MPPC of the Čerenkov tile.
The negative signal outputs generated by each MPPC are connected via delay lines to a Charge-to-Digital Converter (QDC). The used *CAEN Module V965A* is a Dual Range Multi-event QDC housing eight channels integrating negative current inputs over a defined time gate. This means the input charge of each channel is converted to a voltage level by a Charge-to-Amplitude (QAC) section. The dual range capability of the device allows to convert the QAC outputs by two ADCs in parallel. One with a conversion factor of 1, the other with a conversion factor of 8 resulting in a low range of 100 pC (25 fC per ADC channel) and a high range of 820 pC (200 fC per ADC channel) of the QDC in total. Thereby, saturation by large charge pulses can be avoided and the resolution for small ones can be increased. Since it was intended to look for small charge pulses that were created by single photons hitting the sensitive surface of the MPPC's, only the low range mode is used for the analysis presented in this thesis. The trigger signals from the scintillator cross are discriminated into

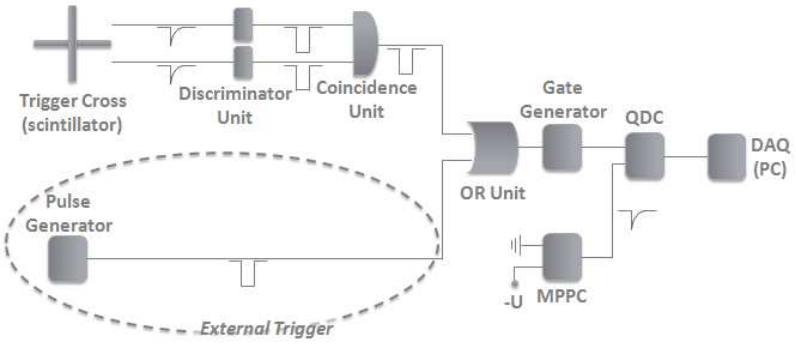

Figure 5.3: The complete electronic readout chain of the test beam setup.

standard NIM signals of -0.7 V before entering a coincidence unit (logical AND). The required QDC gate is produced by connecting the trigger coincidence signal to a gate generator. The gate signal has to precede the analog MPPC signals by 15 ns to 20 ns. This additional delay is requested by the QDC electronics. The gate length of 200 ns is chosen such that as less noise as possible is integrated by the QDC, but without discarding too much of the signal tail.
Two exemplary MPPC signals as observed on an oscilloscope screen can be seen in figure 5.4. Dispersion and attenuation due to 30 m long cables running from the test beam area to the oscilloscope inside the control room smear the three pictured signals out. The number of pixels fired of both MPPC's can be determined by the

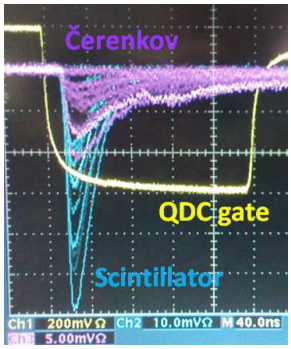

Figure 5.4: Snap-shot of the detected scintillator (channel 3, blue) and Čerenkov (channel 2, violet) signals as seen on the oscilloscope within a gate of 200 ns (channel 1, yellow) produced by triggered events. Note the differing voltage scales.

pulse height of the signals. As expected the number of detected Čerenkov photons is about a factor of $2-3$ lower than the number of detected scintillation photons.
To perform pedestal measurements a pulse generator was installed. It was set to give a negative NIM pulse of 50 ns width and was triggered with a rate of 10 kHz. Connected to the same gate generator with a logical OR unit, it as well produced a gate of 200 ns width. During a pedestal measurement the beam shutter was closed and the QDC integrated the existing electronic noise within randomly distributed gates.
All QDC signals were recorded by a Linux computer and stored in text files on a hard disk for off-line analysis.

5.3 Installation of the Tiles

Each tile was wrapped completely with a reflective coating to increase the signal response primarily in case of rough tile surfaces.
There were two possible reflector materials at hand: *Tyvek*[1] or *3M Radiant Mirror Film*[2] (3M foil). Tyvek is a diffuse reflector, consisting of 0.5 - 10 μm thick olefin fibers that are first spun and then bonded together by heat and pressure. One of its properties is high opacity caused by multiple light refractions among the very fine polyethylene fibers and air within the densely packed sheet structure. An opaque substance transmits no light, and therefore reflects, scatters, or absorbs all of it.
3M foil is a non-metallic reflective coating with a reflectivity of at least 98 % (figure 5.5). It is a non-conducting, multi-layer polymeric film, absorbing wavelengths smaller than 400 nm and larger than 1000 nm.

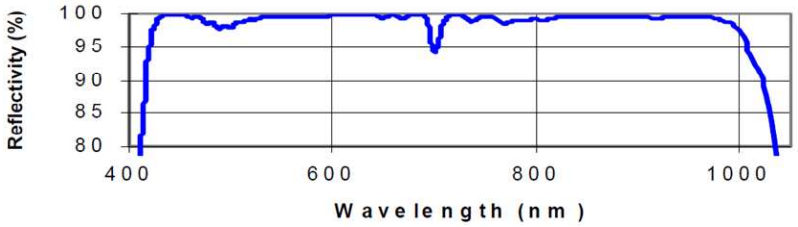

Figure 5.5: Typical reflectivity distribution of *3M Radiant Mirror Film* in percent as a function of the photon wavelength. Provided by the manufacturer [43].

The MPPC was directly coupled to the tile with *Silicon Optical Grease BC-630*[3]. This is a clear, colorless, silicon, optical coupling compound which features an excellent light transmission at 25 °C. It has a specific density of 1.06 and a refractive index of 1.465. The usage of optical cement is reducing the Fresnel losses due to reflections at the optical boundary in front of the MPPC. The relative improvement depends on the agreement between the indices of refraction of the tile material and the optical grease used.
The wrapped tiles were fixed with small pieces of Styrofoam inside especially designed plastic cassettes to avoid movement when the position of the translation stage was changed. Afterwards the entire cassettes were covered with black tape to make them lightproof (figure 5.6) and mounted in a $20\times13\times10\,\mathrm{cm}^3$ large steel case. The tile box is a light-tight, noise shielding container with a $2\times4\,\mathrm{cm}^2$ large window as beam entrance and fixtures for the two cassettes. The final installation is sketched in figure 5.7.
The scintillator tile was placed behind the Čerenkov tile in order to measure signals produced by the same positron. Crucial for such a consideration is the vertical and

[1]Registered trademark of *E. I. du Pont de Nemours and Company*
[2]3M Deutschland GmbH, Lichtsysteme
[3]Saint-Gobain Crystals, Organic Scintillators

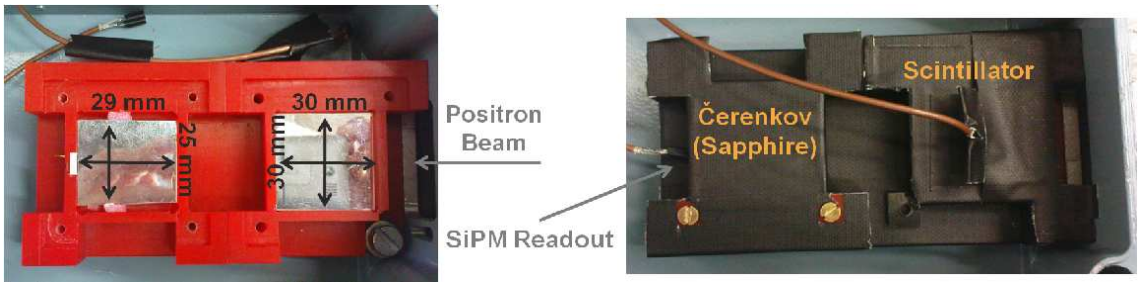

Figure 5.6: Mounting of the tiles and the cassettes inside the steel box. **Left:** Tiles wrapped in a reflective coating and fixed inside the cassettes - the Čerenkov tile on the left, the scintillator on the right. **Right:** Cassettes are mounted inside the steel case and wrapped with black tape for light protection.

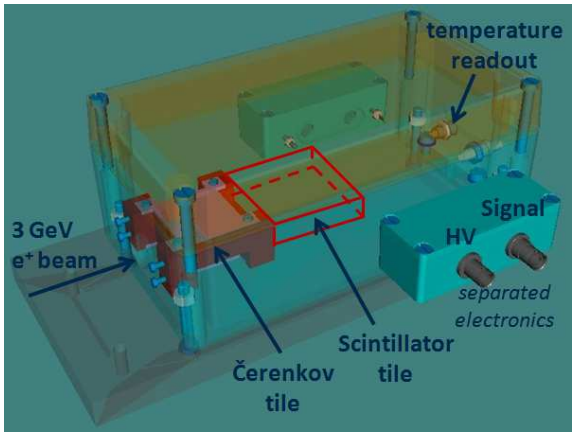

Figure 5.7: Schematics of the steel box containing the test assembly. The cassettes (red) can be seen in which the scintillator or Čerenkov tiles are fixed.

horizontal alignment of the two tiles. They were adjusted as good as possible in height.
To meet the required noise shielding of the MPPC signals, the electronic circuit of each MPPC was attached on the outside wall of the steel case in a separated small box. Small holes enabled coax cables running from the electronics to the respective MPPC for readout and powering.
A temperature sensor of the type Pt100 [44] was installed inside the box to monitor temperature fluctuations and to allow correcting later measurements for them. It exploits the linear change in electrical resistance of platinum (Pt) as a function of the temperature. Sensors of the type Pt100 have a resistance of 100 Ω at 0°C.
A systematic uncertainty of 0.5°C is assumed.

5.4 Tile Shapes and Surface Finishings

The scintillator tile has a size of 30×30×5 mm^3. The MPPC for readout was placed in the center of the large tile surface, lying on top of the tile (figure 5.8). Concerning the Čerenkov tile not only different materials were tested (see section 5.5), but also different shapes - rectangular and rhombic - and different surface finishings - polished and unpolished. An overview of the available configurations concerning material, shape and surface finishings is given in table 5.1.

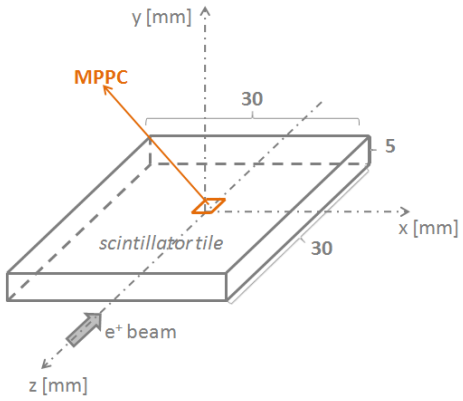

Figure 5.8: Central MPPC readout placement on top of the scintillator tile.

Tile Material	Tile Shape	Surface Finishing	Size [mm^3]
Sapphire	rectangular	unpolished (one side polished)	29×25×4.4
	rhombical	polished	29.8×24.6×4.5
		unpolished (one side polished)	29.7×24.7×4.4
Lead Glass	rhombical	polished	36×20×4

Table 5.1: The different tested Čerenkov tile configurations.

One of the rhombically shaped sapphire tiles is polished completely, whereas the other one is left unpolished besides the small surface where the MPPC should be placed. The purpose of this particular shape was to act as a light guide for Čerenkov photons produced within the tile, guiding them towards the MPPC. The geometrical area where the MPPC was planned to be placed is with 4.5×4.5 mm^2 more than twice as large as the sensitive surface of the MPPC. Ideally, this spot would have been exactly the size of the sensitive surface of the MPPC which corresponds to $3 \times 3\,\mathrm{mm}^2$. Due to the disagreement in size only of 44 % of the Čerenkov photons arriving at the end area are detected.

The lead glass tile was manually machined at DESY. The shape, including the optimal opening angle, and the surface finishing was simulated beforehand (within the scope of other studies [45]). The opening angle producing the highest output signal was found to match the Čerenkov angle of lead glass of 53.22°. With the end

area being $4{\times}4\,\mathrm{mm}^2$ in size one loses at maximum 44 % of the Čerenkov photons guided to the tile end. The photon detection rate is worsened by the fact, that this surface was not achieved to be completely flat but bended slightly outwards.
Pictures of the different tiles plus the sketched outlines of the rhombic Čerenkov tiles can be seen in figures 5.9, 5.10 and 5.11.

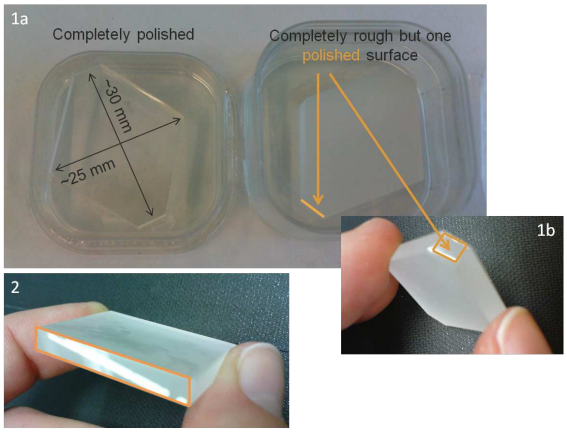

Figure 5.9: The tested sapphire tiles. In 1a) the two rhombic tiles and in 2) the rectangular tile is pictured. In case of an unpolished tile, the polished side is marked orange. In 1b) this denotes also the placement for the MPPC.

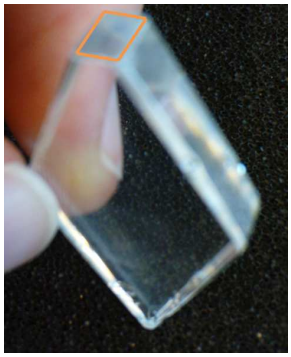

Figure 5.10: Polished lead glass tile as used for test beam measurements. The mounting position of the MPPC is marked orange.

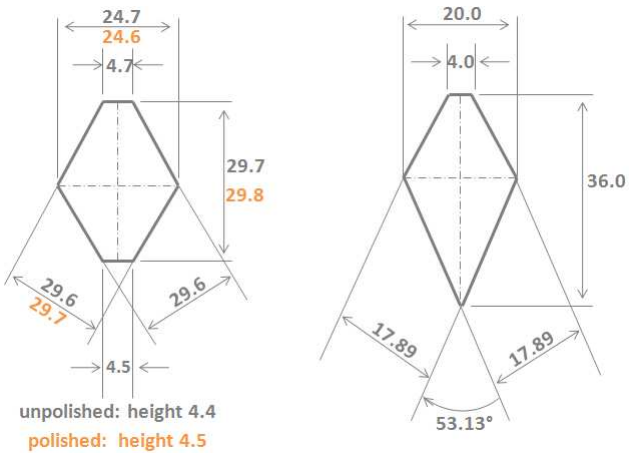

Figure 5.11: Schematics of the three rhombically shaped tiles. **Left:** Two rhombic tiles are made of sapphire. The deviating lengths of the polished sapphire tile are given in orange. **Right:** Dimensions of the rhombic tile made of lead glass.

5.5 Material Characteristics

In total three different tile materials were used for measurements done in the course of this work: plastic scintillator, sapphire and lead glass. The Čerenkov angles quoted in the following section are calculated for a positron energy of 3 GeV. Each of the materials will be described in the following section in more detail.

Scintillator The used plastic scintillator features the largest radiation length (X_0) of all used materials with 42.63 cm. Hence, it has the lowest density with only 1.032 g/cm^3 as well as the lowest refractive index of 1.58 and consequentially the smallest Čerenkov angle of 50.73°. The organic material BASF-130 further processed by the Vladimir company [46] (Russia) emits UV scintillation light with a wavelength peaking at 430 nm (figure 5.12).

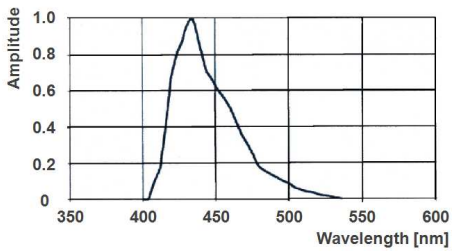

Figure 5.12: The emission spectrum of the used plastic scintillator material.

Sapphire The sapphire tiles used for the measurements are produced and cut to shape by *RSA*[4]. The so-called flamed fusion is used to melt a finely powdered substance with an oxyhydrogen flame and crystallize the melted droplets into a sapphire boule.
The quoted physical quantities are adopted from the database of the producer [47]. The formed colorless crystal is of a rhombohedral structure composed of Al_2O_3. The density is $3.98\,\mathrm{g/cm^3}$ at a purity of 99.998 %. Emanating from a refractive index of 1.76 at 589.3 nm the Čerenkov angle is 55.38°. The radiation length is relatively small with only 7.02 cm. The sapphire tile in combination with the scintillator tile therefore accounts for $0.48\,\mathrm{X_0}$ in total.
Its transmission for a 1 mm thick disk goes down to 60 % at 280 nm (50 % at 200 nm). For a thicker sapphire sample the transmission in the ultraviolet wavelength region is lower. Therefore, the absorption properties of the two reflector types described may not effect the number of possibly detectable photons because most of them in this wavelength range are not even transmitted out of the tile onto the respective foil surface.

Lead Glass Lead glass is made by replacing the calcium content of typical potash glass by lead oxide (PbO). By adding PbO to the glass its density and refractive index raises. The kind of lead glass used for measurements is of the type CEREN 25 produced by *Corning France* which is equivalent to SF5 manufactured nowadays by *Schott AG*[5]. Since no material properties of CEREN 25 could be found, the material properties quoted in the following originate from the Schott database.
SF5 is composed of 55 % PbO which results in a density of $4.07\,\mathrm{g/cm^3}$ and a refractive index of 1.67 at 589.3 nm resulting in a Čerenkov angle of 53.22° [48].
The improvement by using optical grease is higher than in case of sapphire due to the better agreement of the refractive indices of lead glass and BC-630.
The radiation length of lead glass is 2.5 cm. This increases the effective radiation length test setup to $1.51\,\mathrm{X_0}$ and consequentially also the probability for a positron to electromagnetically interact inside the Čerenkov tile.
The internal transmittance of lead glass within the ultraviolet wavelength region decreases rapidly from 360 nm on and goes down to almost zero for smaller wavelengths.

[4]LE RUBIS SA producer of synthetic corundum and spinels, France
[5]SCHOTT AG, Mainz

6 Experimental Results from Test Beam Measurements

Within the following chapter the analyzed results as obtained from test beam measurements with the previously described setup are presented. The experimental results originate from data taken over a period of two months at the end of 2010. After an introduction about the tested tile configurations, it is shown how the light yield of both signals was improved and how this led to the final results concerning maximum achievable light yield and response uniformity. An error estimation including several factors will be discussed.

6.1 Readout Configurations

In total five different readout configurations were tested composed of the four available tile samples. The first two investigated configurations concern the rectangular sapphire tile with a roughened surface. Two mounting positions of the MPPC on the tile with respect to the beam line were examined. Either the MPPC was mounted opposite to the beam entrance (figure 6.1 (left)) or it was rotated by 90° to the unpolished lateral side of the rectangular tile (figure 6.1 (right)).

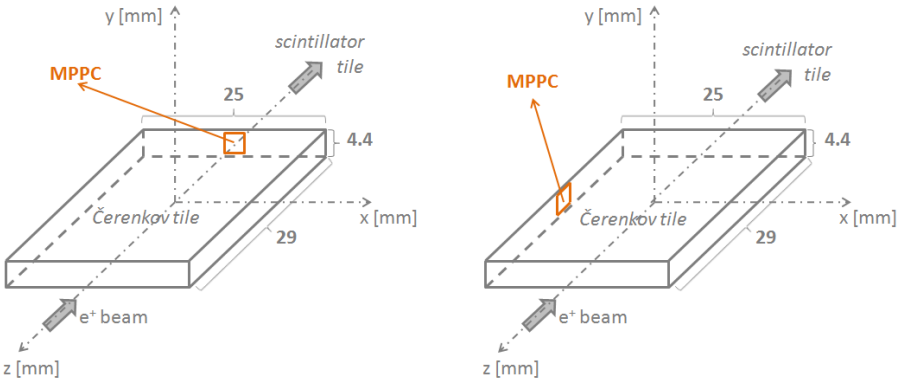

Figure 6.1: Draft of the rectangular tile under a central beam incidence (0°). The placement of the scintillator tile is indicated. **Left:** MPPC positioned opposite to the beam entrance (referred to as Pos_{opp}). **Right:** MPPC positioned at the lateral side, 90° rotated (referred to as Pos_{lat}).

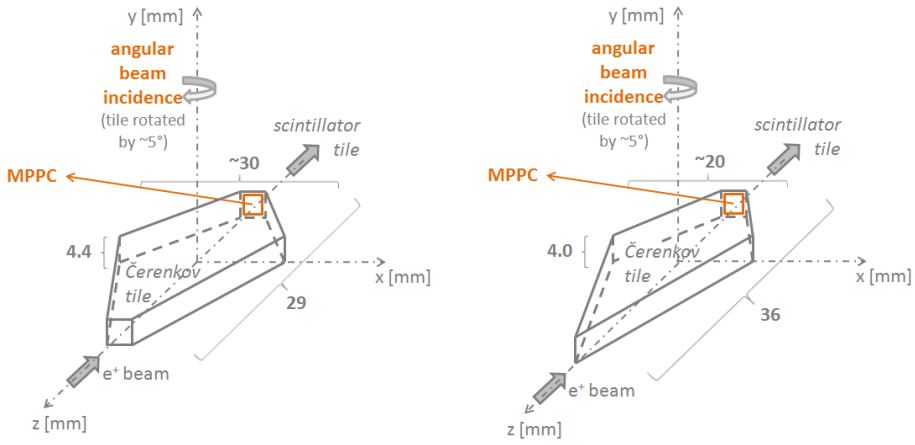

Figure 6.2: Draft of the rhombic tiles under a central beam incidence (0°). A beam incidence under a small angle $\alpha \approx 5°$ is achieved by turning the tile around the y-axis. **Left:** Sapphire tiles. **Right:** Lead glass tile.

For a further improvement in terms of achievable light yield, the rectangular tile was exchanged by rhombically shaped tiles. In total three rhombic tiles, two made of sapphire and one made of lead glass, were examined. The exact dimensions can be read from table 5.1. This particular design was supposed to guide the produced Čerenkov photons towards the MPPC mounting position, resulting in an increase in the light yield 6.2.
The two rhombic sapphire tiles (polished and unpolished surface) feature different dimensions than the rhombic lead glass tile (polished). The opening angle of the lead glass tile equals the Čerenkov angle of lead glass while the rhombic sapphire tiles have a flattened front surface. By choosing this particular design for the lead glass tile, the produced photons shall be even more efficiently guided towards the MPPC surface. It is expected that the higher density of lead glass leads to a higher absolute light yield compared to sapphire.
To build a possible active calorimeter layer composed of rhombic tiles, several different opening angles of the tiles are needed to reduce the dead space in between. Simulations of such a possible calorimeter design resulted in the need of three different rhombic shapes. For more details see [45].
It should be noted, that the calorimeter signal generated by active layers of rhombically shaped tiles would be the sum of all rhombic tiles traversed by the particle. Thereby, the disadvantage imposed by the varying material length traversed by a particle in case of a rhombic tile shape is compensated through the neighboring tiles.
The beam energy for all measurements was set to 3 GeV and 3M foil was used as reflective coating in the configuration 3M foil$_{air}$. The positrons traversed first the Čerenkov tile and then the scintillator tile if not stated elsewise. At least 500 000 events were collected per data run. The obtained histograms are normalized to the respective number of entries and rescaled from QDC-channels to the number of firing pixels or rather the number of detected photoelectrons (p.e.) following equation 4.9.

6.2 Stabilization of Data Acquisition Conditions

The role of the additionally installed scintillator plays an important role in the monitoring of the test beam conditions during data acquisition. Several facts have to be taken into account, before measurements collected over a wide time span become comparable. This includes the consideration of temperature variations, noise fluctuations and other not directly measurable parameters as beam instabilities and the temperature dependencies of the electronics and the dipole magnet installed at the beam line. A reasonable estimation of the resulting uncertainties of the analyzed data spectra will be discussed in the following sections.

6.2.1 Noise Level

During the data acquisition the pedestal was monitored to observe changes in shape, width or amplitude. The width of the pedestal σ_{Ped} originates not only from the used MPPC type, but also from the fluctuating electronic noise depending to some extent on the environmental temperature. The more stable the working conditions are, the smaller are the fluctuations of the pedestal peak. The noise amplitude was nearly stable throughout the testing time, only its width σ_{Ped} fluctuated slightly by a few percent at maximum.
In figure 6.3 an example pedestal measurement is shown. The randomly distributed noise events were collected within gates triggered by an external pulse generator while the beam shutter was closed. The different width of the pedestals arises from the two MPPC types used that differ in the size of their sensitive surface.

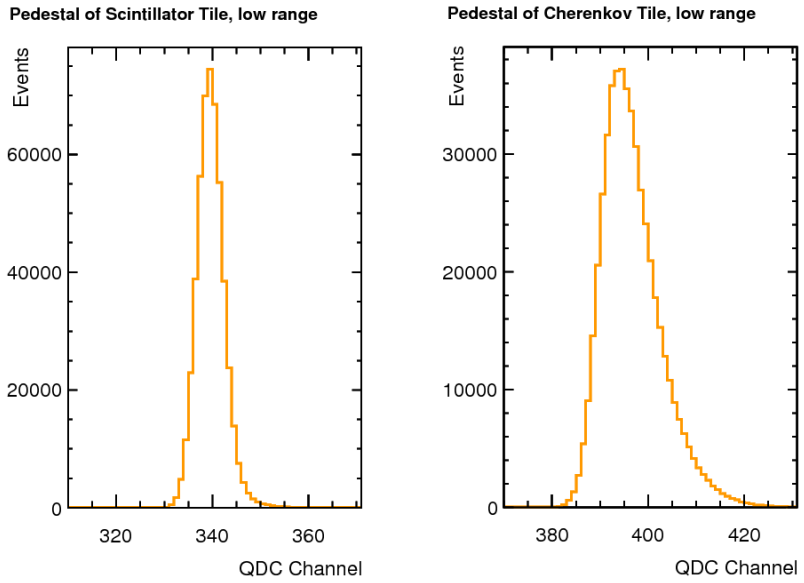

Figure 6.3: **Left:** Scintillator pedestal.**Right:** Čerenkov pedestal. The pedestals were measured with an external pulse generator (see figure 5.3).

As described in chapter 4 the higher the number of pixels is, the larger becomes the noise rate and consequentially the pedestal width.
The mean values of the two histograms shown in figure 6.3 were determined to be $A^{Ped} = 339.7$ QDC-channels with $\sigma_{Ped} = 2.92$ QDC-channels for the scintillator and $A^{Ped} = 396.7$ QDC-channels with $\sigma_{Ped} = 6.22$ QDC-channels for the Čerenkov readout chain.
The signal-to-noise ratio $\frac{S}{N}$ demonstrates the quality of the measurements and is defined as:

$$\frac{S}{N} = \frac{A^{Sig} - A^{Ped}}{\sigma_{Ped}}, \tag{6.1}$$

where A^{Sig} is the signal amplitude of the MPPC.

6.2.2 Beam Energy Dependence

The influence of the beam energy on the number of detected photoelectrons is shown in figure 6.4. Only the rectangular sapphire tile was used for this study, readout in the configuration Pos_{opp}. Its position with respect to the beam impact was not changed during the energy scan. The broad peak (A^{Sig}) is caused by a MIP-like positron crossing the tiles and producing scintillation or Čerenkov photons along its trajectory. The scintillator peak can be fitted with a Gaussian distribution to

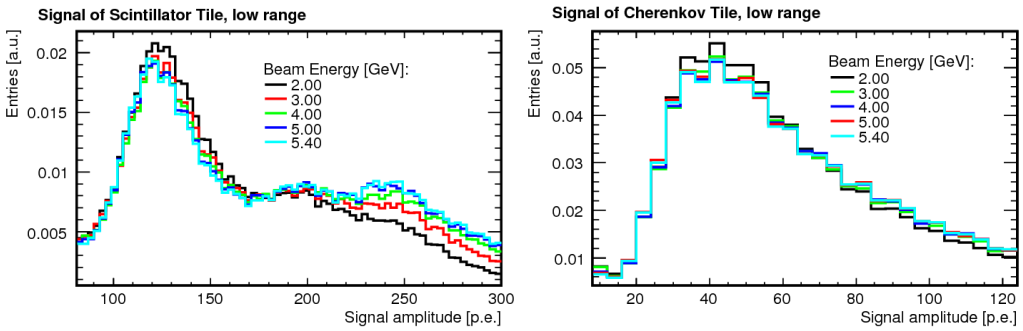

Figure 6.4: **Left:** Signal response of the scintillating material for changing beam energies. **Right:** The corresponding Čerenkov signal of the rectangular sapphire tile for energies between 2 and 5.4 GeV.

obtain the mean amplitude and the width σ_{Scint}, whereas in case of the Čerenkov spectrum a Landau distribution is fitted to the spectrum to gain the most probable value (MPV) and the corresponding width σ_{Cher}. The pedestals are not shown.
While the mean scintillator amplitude A^{Sig}_{Scint} decreases by 2.3 % and narrows by 7 % for higher beam energies, the Čerenkov amplitude A^{Sig}_{Scint} increases by 2.2 % and broadens by 17 %. A small increase in the shower fraction of the scintillator signal can be observed for higher energies.
Since only a small change in the generated signal amplitude A^{Sig} depending on energy is observed, the positrons with energies between 2 and 5.4 GeV can treated as approximately minimum ionizing particles.

6.2.3 Error Estimation

Since the MPPC signal response is temperature dependent, it has to be corrected for this behavior to be able to compare the results of several measurements at different temperatures. The temperature variations at test beam were monitored during the data acquisition (figure 6.5). All data spectra are corrected for the measured mean temperature of 19.95 °C using a temperature dependency of the MPPC signal response of -3.7 %/K (equation 4.6).

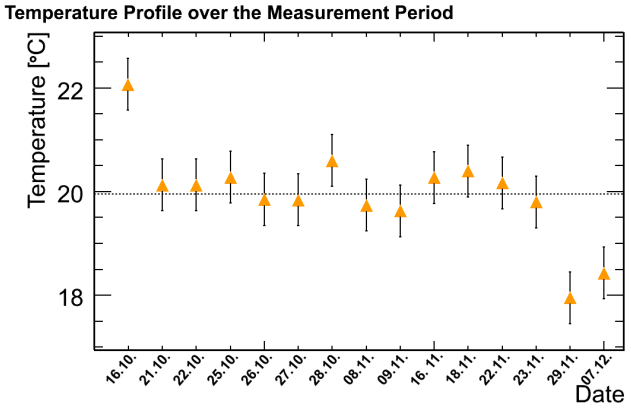

Figure 6.5: Measured temperature profile during test beam measurements with a mean at 19.95 °C (indicated by the dotted black line). On average an uncertainty of 0.5 °C is assumed due to temperature variations over one day.

As mentioned in the introduction of this chapter, the scintillator signal can be used as a reference level for the Čerenkov signal. It is assumed that the scintillator and the Čerenkov signals are subject to the same uncertainties. Temperature fluctuations, positioning and fitting uncertainties contribute to the total uncertainty. In the four readout configurations with sapphire used as Čerenkov material the positrons traverse the same amount of material (track length of ∼30 mm) in case of a central beam incidence before entering the scintillator tile. The scintillator light yield for a central beam impact is maximal due to the chosen readout position of the scintillator MPPC at the tile center. This maximum achievable scintillator signal therefore should be constant under the same operating conditions and consistent temperatures.
However, the measured maximum light yield of the scintillator plotted in figure 6.6 still shows discrepancies. The lead glass tile is included (5) for the sake of completeness. The values are temperature corrected. In case of an optimized beam impact the maximum scintillator light yield is found to be on average 144 p.e./MIP.
The fact that the data points vary around the mean confirms that there still remain environmental uncertainties whose influence can not be directly determined.
However, the maximum relative deviation from the mean scintillator signal can be used to estimate the accuracy of the Čerenkov measurements under the assumption

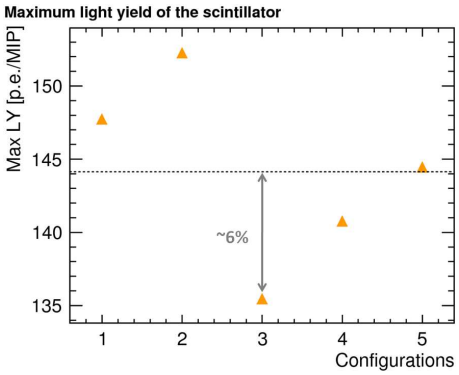

Figure 6.6: Measured and temperature corrected maximum scintillator signals versus the respective configuration. Rectangular sapphire tile with the MPPC positioned at Pos_{opp} (1) and Pos_{lat} (2); rhombic sapphire tiles with a rough (3) and a polished (4) surface finishing and the polished lead glass tile (5).

that the both signals are subject of the same uncertainties. The obtained 6 % at configuration (3) might contain those missing uncertainties and have to be assumed for all further results stating a measured Čerenkov light yield.

6.3 Light Yield Optimization

After having achieved a stable noise level it was tried to improve the measured light yield of the tiles. For those measurements only the rectangular Čerenkov tile made of sapphire readout in the configuration Pos_{opp} was studied.

Reflective Foil

It is known that a reflective wrapping can increase the number of detectable photons. How large the effect is depends on the kind of reflective foil used. Therefore it was searched for the one yielding the highest signal response. There were two possible options available: Tyvek or 3M foil. The first one features diffuse reflection characteristics for wavelengths down to the ultraviolet region, while the second one is a specular reflector (see section 5.3).
To find the ideal wrapping for the rectangular sapphire tile different configurations were analyzed: first without any reflective foil, then wrapped with Tyvek (with and without optical grease) and at last wrapped with 3M foil (with optical grease) (figure 6.7). The 3M foil was either attached with its self-gluing side to both tiles (configuration referred to as 3M foil_{glued}) or the other side of the foil faced the tiles which is the one with the higher reflectivity in the green and blue wavelength region. The reflective foil was fixed in the latter case with adhesive tape to minimize the air gap between foil and tile as much as possible (configuration referred to as 3M foil_{air}). The Čerenkov signal amplitude was measured at a non-optimal beam impact on the

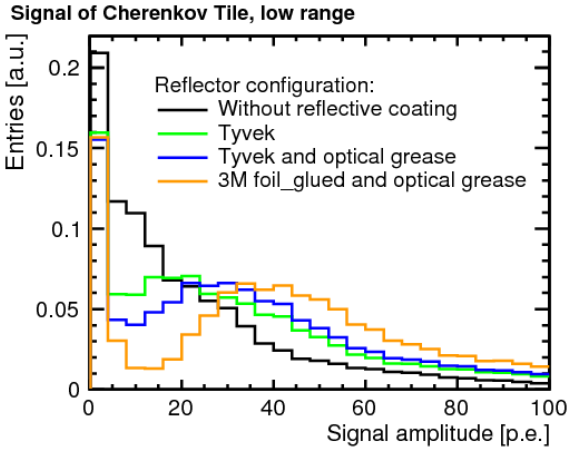

Figure 6.7: Signal response of the rectangular Čerenkov tile (sapphire) for four different reflector configurations.

tile. Still, the relative signal amplitudes can be compared.
The Čerenkov spectrum peaks at different values depending on the tested reflector configuration. If no reflective coating and no optical grease in front of the MPPC is used it is almost impossible to distinguish between the pedestal on the left and the signal peak (black line). The situation improves when the diffuse reflecting Tyvek foil is used and gets even better when in addition optical grease is applied to couple the MPPC to the tile. The best result however is achieved, when 3M foil$_{glued}$ is used in combination with optical grease (orange line). The number of detected Čerenkov photons for this configuration is 51±3 p.e./MIP and was improved by 66.8% compared to the worst setting if temperature corrections are applied. Figure 6.8 gives an overview of the peak positions corrected for the mean temperature at test beam. According to the previous error estimation a 6% uncertainty is assumed for the Čerenkov signals. Relying on these results, 3M foil was used as a reflective coating and the MPPC was coupled to the tiles with BC-630 as optical grease. Since for all

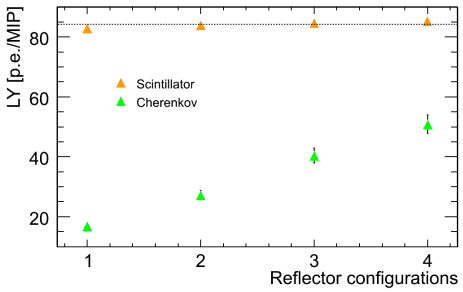

Figure 6.8: Light yield of different configurations is shown: 1 is without any reflective foil, 2 with Tyvek, 3 with Tyvek and optical grease and 4 with 3M foil$_{glued}$ and optical grease. The mean value of the scintillator signal is indicated by the dotted black line.

subsequent measurements as well as for the above presented energy scan the 3M foil was attached in the constellation 3M foil$_{air}$ the impact of this change is examined. Figure 6.9 shows that the scintillator signal is shifted towards a higher amplitude if the configuration 3M foil$_{air}$ is used. Both data runs were taken at almost the same temperature of 19.5 °C and 19.9 °C and the same position of the translation stage, at a beam energy of 3 GeV. This results in a total shift to higher amplitudes of 20 % by switching to the configuration 3M foil$_{air}$.
A similar calculation can be done for the response of the Čerenkov tile. It results in a total difference of 9 % including temperature corrections. It has to be accounted for several uncertainties as stage position, temperature correction and fitting that explain parts of the large difference between Čerenkov and scintillator outcome. Therefore, final correction factors of (20±5) % and (9±5) % for the scintillator and the Čerenkov tile respectively are assumed if the attachment of the 3M foil changes.

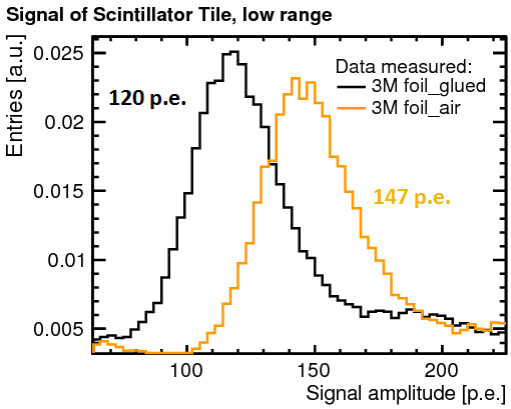

Figure 6.9: Change of the scintillator light yield for different sides of the 3M foil facing the tile surface. For those studies the scintillator tile was exceptionally placed first in the beam line, followed by the Čerenkov tile.

Placement of the Scintillator Tile

In order to improve the light yield of the scintillator tile it as well was coupled with optical grease to the MPPC. This was not the case during the comparison of possible reflector configurations. An increase of 20 % of the scintillator MIP signal can be seen in figure 6.10.
It also shows the impact of the mounting position of the Čerenkov tile in front or behind the scintillator tile. If the scintillator is mounted behind the sapphire tile the positrons show a larger probability to electromagnetically interact inside the scintillator due to the smaller radiation length of sapphire (figure). The chosen geometrical arrangement enables the selection of distinct event samples. A cut on the collected data sample around the determined MIP peak of the scintillator tile for example, should contain only positrons that showed a MIP-like behavior in the

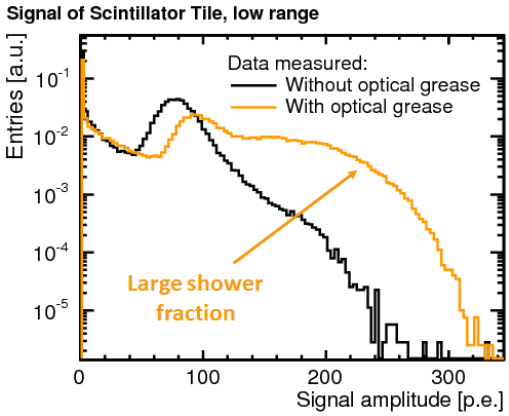

Figure 6.10: The shifted scintillator MIP peak displays the difference in using optical grease or not. The increase in the shower fraction can be seen if the scintillator is mounted behind the Čerenkov tile.

Čerenkov tile and did not interact. It is shown in the appendix that correlated events are hard to investigate due to the very small tile dimensions of only some millimeters.

6.4 Light Yield Measurements

In order to achieve the highest possible signal response of the four Čerenkov tiles, their surface was scanned at each particular configuration with the active beam area in the vertical and horizontal direction. This is done by varying the position of the translation stage in steps of ∼1-2 mm with respect to the $5{\times}5\,mm^2$ large beam incidence. First a beam scan in the vertical direction was accomplished and adjacent at the found optimal y-position in the horizontal direction. The MPV's of the obtained Čerenkov signals are plotted versus the respective beam incidence on the front face of the tile. The applied error of ±0.5 mm on the stage position is due to the non-reproducibility of particular stage positions. A fit uncertainty of ±0.5 p.e. is applied to the quoted values of the measured light yield.
All tiles were completely wrapped with 3M foil$_{air}$ and the positron beam energy was set to 3 GeV. Temperature corrections are applied on the measured spectra as well as the fitting results.

Rectangular Sapphire Tile

The two readout configurations of the rectangular sapphire tile were measured first and the two data samples yielding the maximum light yield found for each of them will be compared at the end of this section.

MPPC mounting position $\mathbf{Pos_{opp}}$ The MPPC was mounted opposite to the beam entrance facing the arriving positron. Positrons traversing not only the tile but also directly the MPPC are not disturbing the tile response, but enlarge the signal amplitude by one more fired pixel at those central beam impacts.
A vertical and a horizontal scan over the entire tile height and its partial width is shown in figure 6.11. The vertical beam scan is supposing a center position of $y = +2\,\text{mm}$ for a tile extension over a range of $\sim 0 < y < 4\,\text{mm}$. The tile response within this range is stable. The mean light yield is illustrated by the black dotted line at (56.5 ± 1) p.e./MIP. Since the setup is symmetric around the tile center and thus to the MPPC placement, only one half of the tile is scanned in x in detail. For $x < 0\,\text{mm}$ the signal amplitude decreases in the same manner as for $x > 0\,\text{mm}$. The

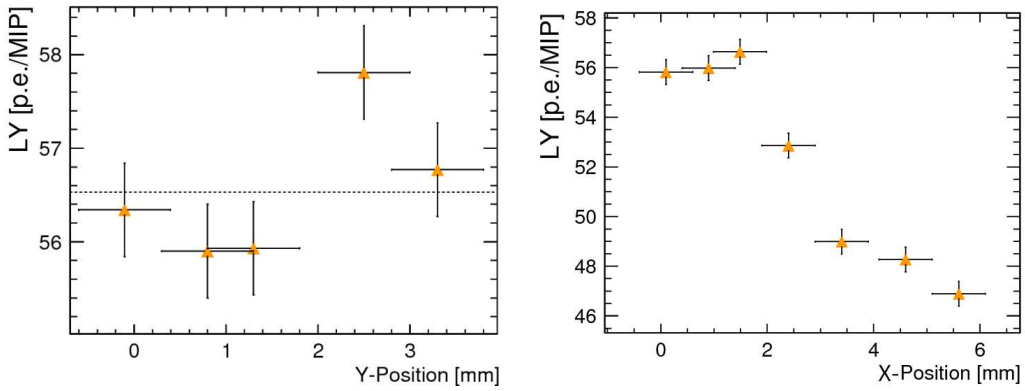

Figure 6.11: MPPC placement Pos_{opp}. The x-axes represent the x- and y-position of the translation stage with respect to the beam incidence. A systematic error of $\pm 0.5\,\text{mm}$ is applied to the position and of ± 0.5 p.e. on the light yield. **Left:** Light yield of the Čerenkov tile for a Y-scan. **Right:** At $y = 1.8\,\text{mm}$ the x-direction is scanned.

tile's center is assumed to lie within the two plateaus at $(x|y) \approx (+1.0| + 2.0)\,\text{mm}$. The maximum number of detected Čerenkov photons is found to be (56 ± 1) p.e./MIP within the plateau region by optimizing the position of the beam incidence on the front face of the tile.

MPPC mounting position $\mathbf{Pos_{lat}}$ The MPPC placement on the rectangular sapphire tile was changed to understand the influence on the light yield for different MPPC mounting positions. Again the beam was moved in x- and y-direction over the tile's front surface to find the position with the highest signal amplitude (figure 6.12). In the vertical direction the tile as well shows a very uniform behavior over its entire height, reaching a mean light yield of (33.5 ± 0.5) p.e./MIP (black dotted line). Whereas so far the optimal position was found to be in the center of the tile, now the largest number of Čerenkov photons is detected at the horizontal edge of the tile, close to the MPPC placement. The signal measured opposite to the MPPC mounting position decreases 28 p.e./MIP.

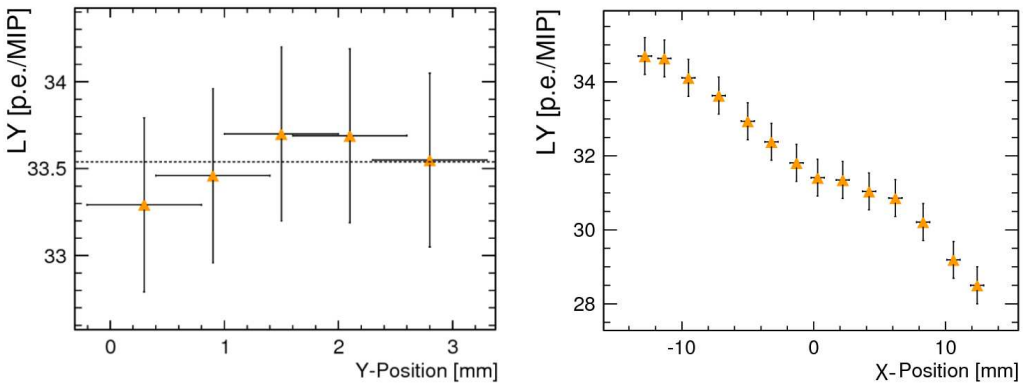

Figure 6.12: MPPC placement Pos_{lat}. The x-axes represent the x- and y-position of the translation stage with respect to the beam incidence. The applied errors are composed as in figure 6.11. **Left:** Light yield of the Čerenkov tile for a y-scan. **Right:** At y = 1.3 mm the x-direction is scanned.

The two setups Pos_{opp} and Pos_{lat} were measured within one day at 18.6 °C (Pos_{opp}) and 18.9 °C (Pos_{lat}). The final comparison is shown in figure 6.13 and the signal amplitudes are compared in table 6.1. Summarizing those results it can be stated, that the optimal position in terms of highest light yield is always found to be close to the MPPC. In the case of the configuration Pos_{opp}, a central beam incidence, exactly opposite to the MPPC is favored and in case of Pos_{lat} beam incidences close to the edge result in the highest output.
The reason for the difference in the number of entries of the two compared MIP signals is as well due to the differing optimal beam impacts. At the optimal position of Pos_{lat} more initial positrons than at other entrance points miss the tile and are

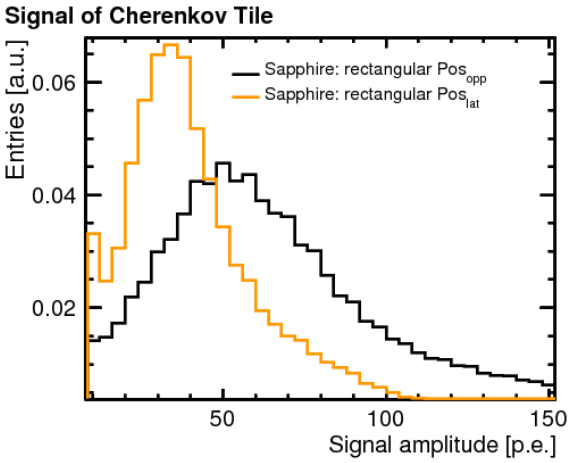

Figure 6.13: Comparison of different MPPC placements. Only runs reaching the maximum light yield of each configuration are shown. Temperature corrections are applied.

Configuration	$A^{Sig}_{\mathbf{Cher}}$ **[p.e./MIP]**	$\sigma_{\mathbf{Cher}}$ **[p.e./MIP]**
Pos_{opp}	47.90	15.28
Pos_{lat}	29.32	8.57

Table 6.1: Overview of the maximum light yield for different MPPC positions on the rectangular sapphire tile. Temperature corrections are applied.

therefore adding to the number of pedestal events reducing the number of entries in the MIP peak. As expected the absolute Čerenkov signal is higher for the setup Pos_{opp} than when the MPPC is mounted on the lateral side of the tile. The maximum MIP response is shifted by 38 % including temperature corrections to lower signal amplitudes and the value of σ_{Cher} decreases by 47 %. The signal-to-noise ratio following equation 6.1 drops from $\frac{S}{N} = 35$ down to $\frac{S}{N} = 22$, but is still high enough for a satisfying resolution of pedestal and MIP peak. This is one of the key issues if one thinks about using the Čerenkov effect for future calorimeter developments.

Rhombic Sapphire Tiles

At first the rhombic sapphire tile with an almost completely rough surface was examined. Only the small area where the MPPC is placed is polished. A scan with the beam incidence on the tile surface over a range of 4 mm in y was done first to find the vertical tile center. As can be seen in figure 6.14, the response for dif-

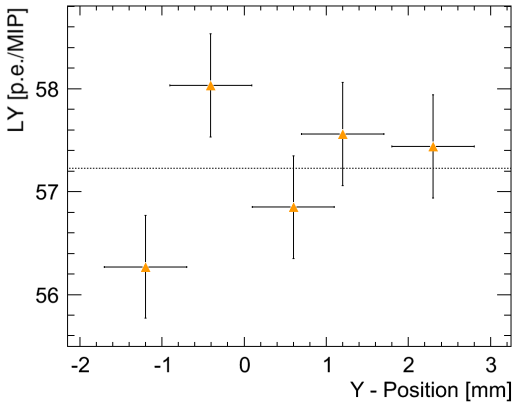

Figure 6.14: Scan in the vertical direction of a rhombically shaped, rough sapphire tile. The black dotted line indicates the calculated mean value.

ferent vertical positions is behaving uniformly. A systematic error of ±0.5 mm on the position accuracy and of ±0.5 p.e. on the measured light yield is applied to all measurements as before. The mean light yield is found to be 57±1 p.e./MIP. As final vertical position y = +1.0 mm is chosen for all further scans in x, since the two tiles were exchanged without moving the translation stage in the vertical direction. The results gained for a scan in the horizontal direction over the front surface of the rough and completely polished sapphire tile are pictured in figure 6.15. A range of

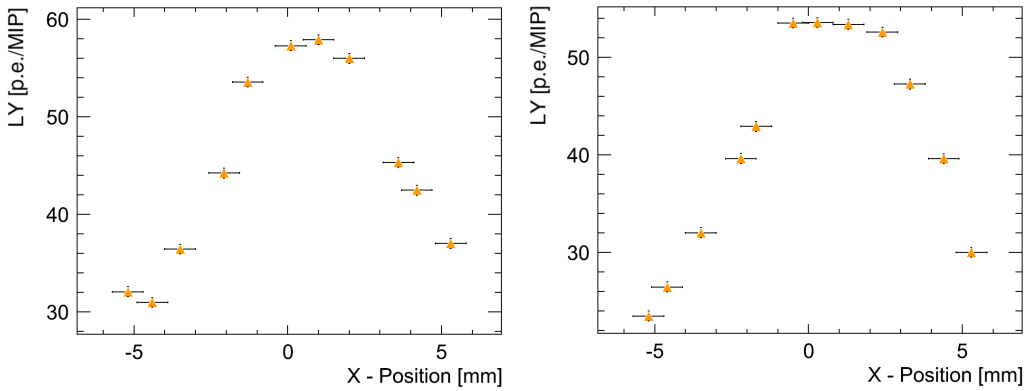

Figure 6.15: Horizontal position scan at y = 1.0 mm for an unrotated beam impact. **Left:** Rough sapphire tile. **Right:** Polished sapphire tile.

approximately 10 mm was scanned in each configuration. There is a central maximum light yield found of 58 p.e./MIP ($x = 1.0$ mm) in case of a rough surface and of 54 p.e./MIP ($x = 0.3$ mm) for a polished surface. The symmetric tile shape can be derived from the graphs since the data points group around a center of ∼1.0 mm which also corresponds to the mounting position of the MPPC on the rear back of the tile. For a direct comparison of a polished and an unpolished rhombic sapphire tile, the two optimal runs are plotted in figure 6.16 and their analyzed MIP peaks are listed in table 6.2. The maximum tile response is by 16 % larger in case the surface is roughened than if it is polished. Compared to the results found for a rectangular sapphire tile, the absolute light yield, the expected increase when using a rhombically shaped sapphire tile is not seen. The highest result is still gained for a central beam incidence opposite to the MPPC placement. Since the amount of material passed at this position is the same for the rectangular and the rhombic tile, the absolute light yield is similar.

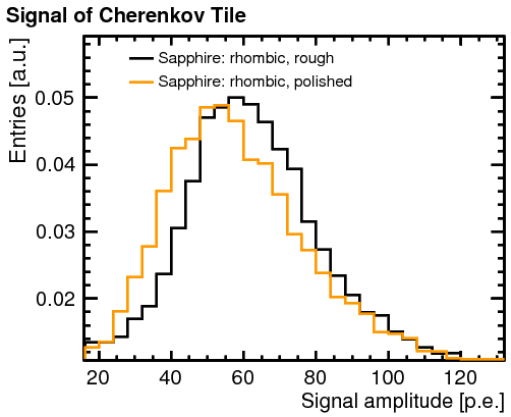

Figure 6.16: The two Čerenkov spectra showing the achieved maximum light yield for a rhombic sapphire tile with an unpolished and a polished surface. Temperature corrections are applied.

Surface Finishing	$A^{Sig}_{\mathbf{Cher}}$ [p.e./MIP]	$\sigma_{\mathbf{Cher}}$ [p.e./MIP]
rough	62.32	11.32
polished	52.65	11.93

Table 6.2: Overview of the maximum light yield for different surface finishings of the rhombic sapphire tile. Temperature corrections are applied.

Rhombic Lead Glass Tile

The observed shape of the collected lead glass spectra differs from the ones gained for the sapphire tiles. On the one hand the MIP peaks of the Čerenkov spectra are less well defined and have a 3-4 times larger width (figure 6.17). On the other hand depending on which material is placed in front of the scintillator, the fraction of events that interact inside the scintillator increases from 16 % in case of sapphire to 39 % in case of lead glass. This can be explained by the 2.8 times smaller radiation length of lead glass compared to sapphire.
The results of a vertical and a horizontal beam scan are shown in figure 6.18. Since the MIP peaks are hard to distinguish the fitting routine of the MIP peak with a Landau function had to be done by hand and a larger uncertainty of ±5 p.e. is applied to the MPV's gained.
The distinction between pedestal and MIP peak is only possible for some positions in x and y. Shifting the beam incidence by only 1-2 mm the MIP peak is smeared out and a fit is no longer possible. The maximum number of detected Čerenkov photons during a vertical position scan of (104±5) p.e./MIP with a σ_{Cher} of 62 p.e./MIP could not be reproduced during the horizontal position scan (figure 6.19). For further comparisons of maximum measured light yields the result found with the horizontal scan of (92±5) p.e./MIP is used. Within the small range in which the MIP signal is distinguishable a sufficiently large signal-to-noise ratio of $\frac{S}{N} = 65$ at maximum is reached.

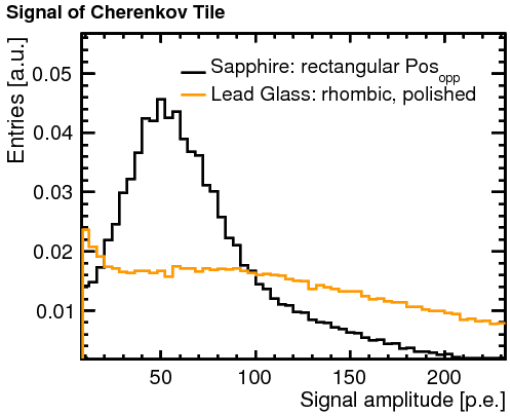

Figure 6.17: Two exemplary Čerenkov spectra of lead glass and sapphire are compared.

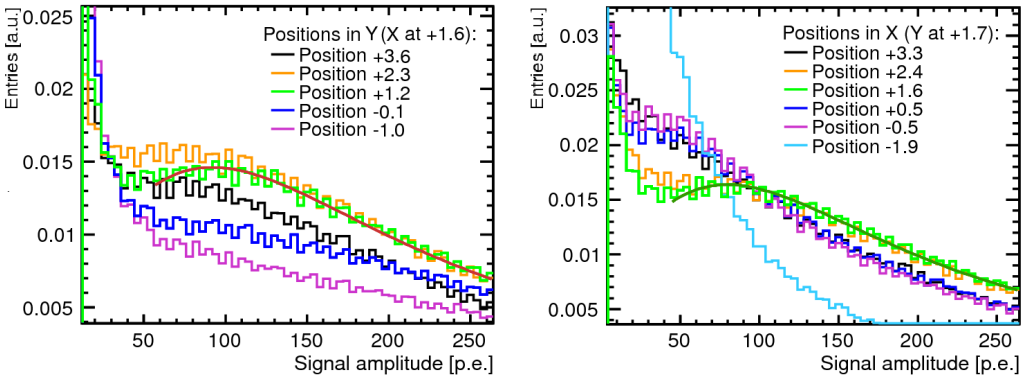

Figure 6.18: Čerenkov spectra for different beam incidences. **Left:** Vertical beam scan over the lead glass surface. **Right:** Horizontal scan with $y = +1.7\,\text{mm}$.

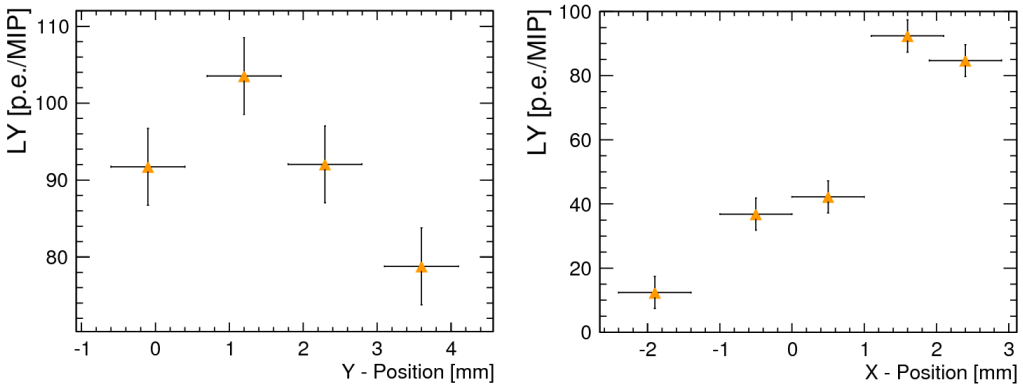

Figure 6.19: **Left:** Light yield for a vertical beam scan over the lead glass surface. **Right:** Light yield for a horizontal scan at $y = +1.7\,\text{mm}$.

6.5 Uniformity of the Tile Responses

It is one of the main objectives to state a measure of how uniform the tile response is with respect to the beam incidence. Uniformity is defined, within the context of this study, as the ratio between the measured light yield at a particular position and the maximum light yield measured for the examined range. Non-uniformity consequentially is defined as the percental deviation from the maximum light yield. Either 100 % uniformity or 0 % non-uniformity would be reached with an ideal tile configuration. The tile response for different vertical beam incidences can be stated to be uniform up to some extent. This behavior can be explained by the good agreement between the tile height and the sensitive surface of the MPPC. The tile non-uniformity is therefore studied based on the results of the horizontal position scans presented in the previous section. Additionally, to examine the degree of uniformity achievable in case of a rhombic tile shape, measurements with an angular beam incidence of $\alpha = 5°$ were accomplished.

Rectangular Sapphire Tile

The two MPPC readout configurations of the rectangular sapphire tile yield not only a different maximum light yield achievable, but also a quite different behavior concerning the observed no-uniformity of the tile response. In case of Pos_{opp} as soon as the beam incidence is moved away from the central plateau region, the light yield decreases from (56±1) p.e./MIP within the plateau region down to 47 p.e./MIP at a 6 mm off-center position. This corresponds to a decrease of 17 % that would increase even more for larger off-center positions. The in parts high horizontal non-uniformity of the signal amplitudes within millimeters, shows how sensitive the whole setup is concerning the beam incidence on the tile.
The dependence on the beam incidence in case of Pos_{lat} is not that strong. The number of detected Čerenkov photons decreases from 34 p.e./MIP down to 28 p.e./MIP which corresponds to a total non-uniformity of 18 % of the entire tile with respect to the maximum amplitude. In case of Pos_{lat} moving the position of the beam incidence

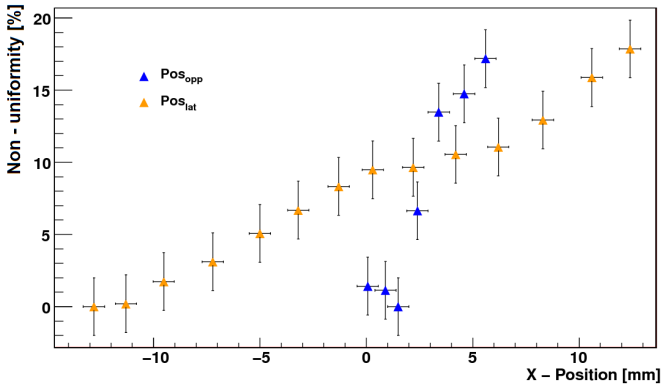

Figure 6.20: Non-uniformity compared for the two readout positions of the rectangular sapphire tile.

on the tile 5 mm away from the maximum the light yield is reduced by ∼3%. Even though the rectangular Čerenkov tile response, when readout in the configuration Pos_{opp}, is higher by approximately 38 %, it is also behaving much more non-uniform. It varies with up to ∼17% for a 5 mm off-center beam incidence which is more than a factor of 5 worse than observed for Pos_{lat}.

Rhombic Sapphire Tiles

The two rhombic sapphire tiles show a similar non-uniform behavior with a symmetry around the tile center as the rectangular sapphire tile does if it is readout in the constellation Pos_{opp}. But it has to be taken into account that the smaller light yield per MIP for beam incidences more outside of the tile's center is not only a consequence of a non-optimal position, but also of the decreasing amount of material passed by the positrons. In the same way the uniformity is reduced for larger off-center positions, also the number of irradiated Čerenkov photons is

lowered. The amount of theoretically produced photons is therefore reduced by a factor of $l(x)/l_{max}$ depending on the beam incidence in x on the tile. A tile center at $x = +1.0\,\text{mm}$ and a maximum tile length of 29.7 mm (29.8 mm) is assumed in case of the roughened (polished) rhombic sapphire tile. The stated non-uniformity has to be corrected for this effect. Figure 6.21 shows the non-uniformity in terms of $(1 - [\text{LY}_{meas}/\text{LY}_{max}])$ for the two tiles, but corrected for the length passed by the positrons at one particular beam incidence. The corrected maximum non-uniformity over a range of ±5 mm decreases to 22% (47% uncorrected) in case of a rough surface and to 30% (56% uncorrected) in case of a polished surface. The behavior of the roughened rhombic tile is compared to the rectangular sapphire tile readout in the configuration Pos_{opp} only slightly worse. The polished rhombic tile deviates from those results by a factor of approximately 1.5.

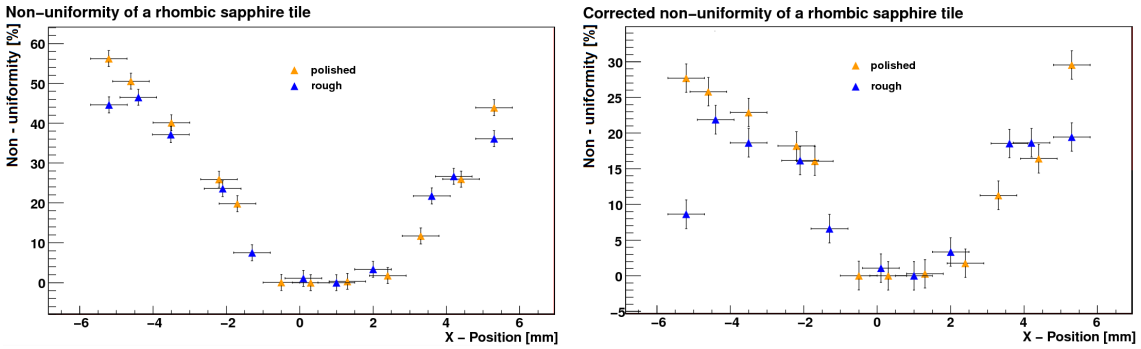

Figure 6.21: Non-uniformity corrected for a reduced Čerenkov light production at positions in x (y = 1.0 mm). A systematic error of ±2% is applied to the quoted values of the non-uniformity. **Left:** Rhombic sapphire tile with a rough surface. **Right:** Rhombic sapphire tile with a polished surface.

Angular Beam Incidence Another possible measure for the uniformity of rhombic tiles is the response under a non-central beam incidence (figure 6.22). Horizontal beam scans show in both cases a lowered signal amplitude by approximately 21% now centering around ∼5 mm. However, scans with different beam angles would have to be done to state correct conclusions about the uniformity measured in such a way. This would require a more sophisticated test stand able to reproduce earlier angle measurements with a higher precision. So far it can only be declared that the signal amplitude changes for positrons passing through the tile under a certain angle.

Rhombic Lead Glass Tile

Similar measurements are carried out to determine the uniformity of the signal amplitude generated by the polished lead glass tile. The observed light yield distribution as a function of the beam incidence also leads to a higher signal non-uniformity.

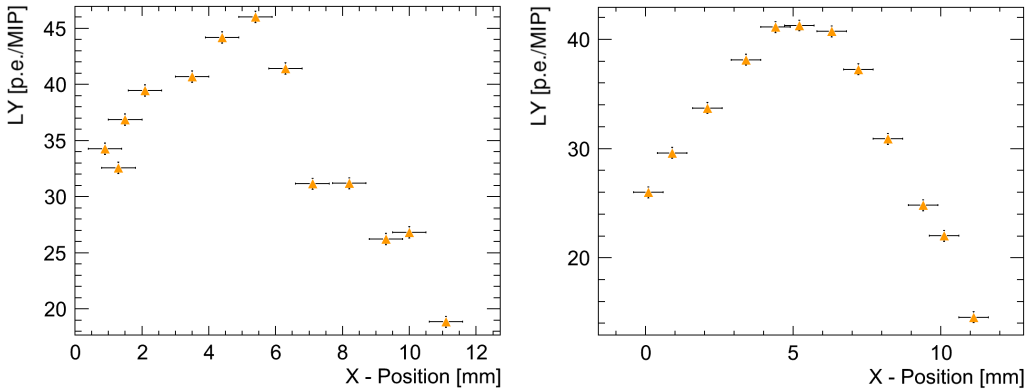

Figure 6.22: Horizontal position scan at y = 1.0 mm for a beam incidence angle of $\sim 5°$. **Left:** Rough sapphire tile. **Right:** Polished sapphire tile.

It seems that only if the beam hits close to the center of the tile a peak is distinguishable. The vertical scan yields a non-uniformity of 12 % within the range over which the tile height extents, but might also be affected by the fitting uncertainties. The data point at $y = 3.6$ mm is already close to the tile edge and would predict a too high non-uniformity. Figure 6.23 shows a comparison of the uncorrected and corrected non-uniformity as a funtion of the horizontal beam incidence (see appendix for the correction factor). In the horizontal direction the light yield fluctuates with up to ∼50 % for a 2 mm off-center position. The non-uniformity increases within a few more millimeters to 77 % before the MIP signal is no longer distinguishable.

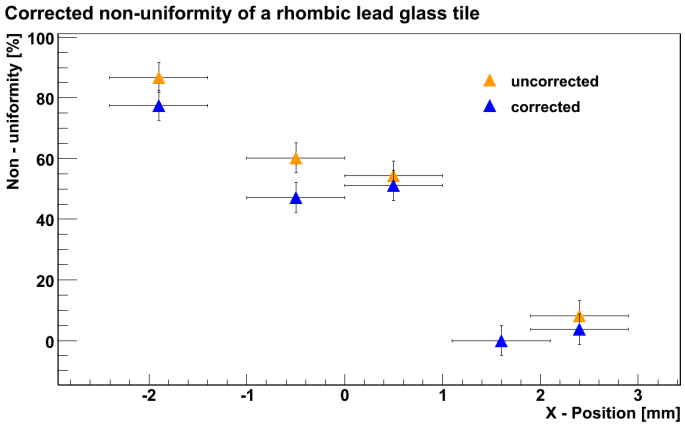

Figure 6.23: Corrected non-uniformity of the lead glass tile. A systematic error of ±5% is applied to the quoted values of the non-uniformity.

Angular Beam Incidence As in case of sapphire also the rhombic lead glass tile was turned by a small angle of ∼5°. But in contrast to the lowered signal response of sapphire for a rotated tile, the signal in case of lead glass increases by 5 % up to 97±1 p.e./MIP and a σ of 49 p.e./MIP (figure 6.24). This confirms the earlier comment that a scan at different rotation angles is inevitable to fully understand the behavior of the tiles for an angular beam incidence.

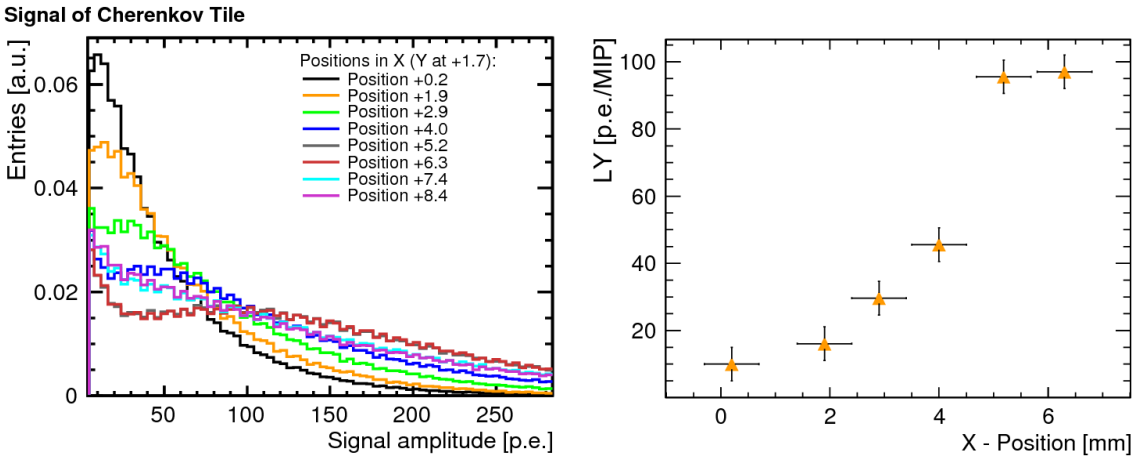

Figure 6.24: Horizontal beam scan of the front face of a lead glass tile turned by ∼5° (zoomed section).

6.6 Conclusion

Five configurations differing in the respective tile shape, the used material and the MPPC readout positions were studied. The achieved maximum Čerenkov light yield LY_{max} was measured with a Hamamatsu MPPC of the type S10362-33-050C. The detected photoelectrons were generated by a MIP-like positron producing Čerenkov photons along its trajectory through the tiles. The results for each tested configuration is summarized in table 6.3 and the single data points are plotted in figure 6.25. The degree of non-uniformity with respect to the maximum light yield relates to a beam incidence within ±5 mm around the optimal beam position. A 6% uncertainty was applied to the temperature corrected Čerenkov data points relying on the discussion in section 6.2.3.

Material	**Configuration**	**LY_{max} [p.e./MIP]**	**σ_{Cher} [p.e./MIP]**	**Non-Uniformity (±5 mm) [%]**
Sapphire	(1) Pos_{opp}	48±3	15±1	17±2
	(2) Pos_{lat}	29±2	9±1	3±2
	(3) rhombic *(rough)*	62±4	11±1	22±2
	(4) rhombic *(polished)*	53±3	12±1	30±2
Lead glass	(5) rhombic *(polished)*	77±5	62±5	77±5

Table 6.3: Summary of the maximum Čerenkov light yield measured for all configurations. The non-uniformity refers to a beam incidence ±5 mm around the optimal beam position. The values are corrected for the mean temperature measured at test beam of 19.95°C.

The highest LY_{max} of the Čerenkov tile is found for lead glass (5). However, this material also yields the highest non-uniformity due to a response signal that varies strongly with a slight change of the beam incidence on the tile. The measured MIP signals in case of lead glass show such a broad distribution and are very position sensitive, that a distinction of the MIP peak is difficult. Lead glass in the investigated rhombic tile shape is thus unsuitable for Čerenkov light yield measurements in small tiles.
The investigation of two different readout positions of the rectangular tile (1,2) result in a 38 % higher light yield if the MPPC is placed opposite to the beam incidence. The measured light yield of the two configurations (1) and (4) agree within their errors of approximately 50 p.e./MIP. The built test setup is not sensitive enough to draw a conclusion about a possible difference between their maximum signal responses.
A difference of 16 % is observable between the maximum light yield of the two rhombic sapphire tiles (3,4). After their signal amplitudes are corrected for a varying tile length the non-uniformity of their tile responses differs by a factor of 1.4. On the basis of these two observations it can be concluded that the surface finish of two

equal tiles has an effect on the outcome. The tile response in terms of light yield and uniformity is improved if the tile surface isroughened. The quoted non-uniformity of

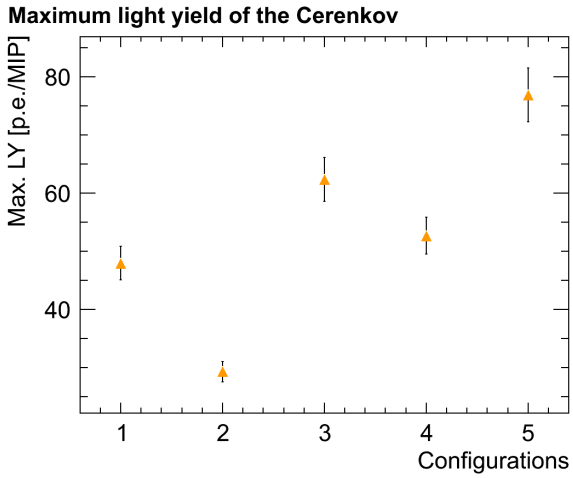

Figure 6.25: Comparison of the maximum Čerenkov light yield for each analyzed configuration: (1)sapphire (Pos_{opp}), (2)sapphire (Pos_{lat}), (3)sapphire, rhombic (rough), (4)sapphire, rhombic (polished) and (5)Lead glass. Temperature corrections are included.

the rough rhombic sapphire tile of 22 % is close to the value found for a roughened rectangular sapphire tile of 17 % in the readout configuration Pos_{opp}.
The lowest non-uniformity with 3% features the rectangular sapphire tile readout in the configuration Pos_{lat} (2). However, in this configuration also the lowest LY_{max} is observed. Since the signal-to-noise ratio is still sufficiently high, it makes this particular configuration next to a rough rhombic sapphire tile (3), compared to all other configurations analyzed within the scope this thesis, a promising candidate suitable for the integration in a PFA optimized hadronic calorimeter. Which one of these two configurations is chosen depends on whether a high light yield or a very small non-uniformity of the tile response is preferred. A stable signal response is often considered to compensate a loss in the maximum achievable light yield. One advantage of a rectangularly shaped tile is its easier production process and the straight forward assembly to one active calorimeter layer.

7 Geant4 Framework

Geant4[1] is a software toolkit to simulate the passage of particles through matter with Monte-Carlo methods. It covers a complete range of functionality including complex geometry, physics processes, tracking and hits. The abundant set of physics models handles interactions of particles with matter across a very wide energy spectrum ranging from only 250 eV up to several TeV.
The package provides ways to specify the geometry of particle detectors including all involved materials and their characteristic properties. Information about interaction type, current volume and energy of the created and tracked fundamental particles, can easily be accessed. The visualization of detector parts or particle trajectories is possible.
The components of the simulation framework, relevant for this thesis, are described in the following. More information on Geant4 in general can be found at [49].

7.1 Global Structure

Currently 17 major categories, hierarchically depending on each other, exist. Superior to the fundamental categories like units, constants and random number handling, reside categories defining materials, particles and geometries. Those categories responsible for the *Tracking*, the *Event* managing and complete *Runs*, consisting of events sharing a common beam and detector implementation, are ranked higher in the command structure. It is in general differentiated between *Tracks* and *Steps* when describing a particle's trajectory. Whereas the former represents a particular state of the particle and therefore holds momentary information, a *Step* carries a 'delta'-information between the start and end point of a step. The propagation of particles in Geant4 is subdivided into steps, where the step length is diced for every possible process and the one with the shortest step length is picked.
The code framework can be customized by specifying user classes. For some of those classes the implementation, instantiation and registration is mandatory, but optional for others [50].
The three mandatory user classes are:

- `G4VUserDetectorConstruction`: Here, the user has to provide information about the geometry of the detector that shall be simulated.

- `G4VUserPhysicsList`: The needed physics processes are defined.

[1] **Ge**ometry **an**d **T**racking

- `G4VUserPrimaryGeneratorAction`: Kind, number and initial properties of the primary particles have to be provided.

There is no default implementation given in advance for any of those abstract classes. The user must derive his own concrete classes from them.
The five optional user classes allow a modification of the default behavior of Geant4:

- `G4VUserRunAction`: Actions are specified that shall be executed at the beginning and end of every *Run*.
- `G4VUserEventAction`: The same as above but now for every *Event*.
- `G4VUserStackingAction`: Customization of the track stacks.
- `G4VUserTrackingAction`: Actions that shall be performed at the creation and completion of every *Track*.
- `G4VUserSteppingAction`: Here, the behavior of every *Step* can be customized.

All of those classes were customized for the simulations carried out for this thesis, including the special needs when simulating Čerenkov light.

7.1.1 Geometry

The geometry package offers the ability to describe the geometrical design of a detector in great detail. This includes physical properties, as the composition of materials and optical properties for example. To correctly define a particular volume, first a solid of the needed shape and size has to be chosen. Then a *logical volume* is created by assigning physical attributes to this solid. Finally, the previous information is merged with placement coordinates and a possible rotation of the volume to generate a *physical volume*. It can be placed within the surrounding mother volume or within another logical volume.
A volume can be declared as a *sensitive detector* that stores information about the properties of the particles at the point of detection.

7.1.2 Optical Processes

The relevant physics processes can individually be activated and customized in the a *physics list*. All particles that can occur within the simulation have to be registered there once.
In the following section only those physics processes are illustrated that create or invoke optical photons. A photon is called *optical* if its wavelength is much greater than the typical atomic spacing. They are therefore treated in a different way than the higher-energetic *gammas*. This allows the incorporation of wave-like properties of electromagnetic radiation into the optical photon process. If the optical photons are produced as secondaries their polarization is assumed to be linear.

Optical photons are created primarily by the Čerenkov and the scintillation process. A small number of optical photons is also created through transition radiation, but this process will be neglected in the following. The optical photons can undergo the following processes: reflection and refraction at medium boundaries, in flight bulk absorption, Rayleigh scattering and wavelength shifting [51]. The material properties essential for such processes are the refractive index, the absorption length and the emission spectrum. Those are stored in a properties table as a function of the photon's energy.

Čerenkov Process The radiation of Čerenkov light along a cone with opening angle θ_c occurs if a charged particle moves through a dispersive medium faster than the velocity of light in that medium. Time and position of the emitted photons are calculated from quantities known from the beginning of the particle's step. The number of produced photons is assumed to be distributed rectilinear along the step, even if the particle slowed down significantly during the step or a magnetic field is present. The average number of Čerenkov photons produced per unit path length of a particle with charge ze and per unit energy interval of the photons is:

$$\frac{d^2N}{dEdx} = \frac{z^2\alpha}{\hbar c} \sin^2\theta_c \approx const, \tag{7.1}$$

where α is the fine-structure constant and θ_c the material depending Čerenkov angle. This can be further approximated for a single charged particle ($z = 1$) to

$$\frac{dN}{dx} \approx 370 \sin^2\theta_c \text{ eV}^{-1}\text{cm}^{-1}. \tag{7.2}$$

The number of photons produced in Geant4 per step length L is calculated from a Poisson distribution with a mean of $< n >= L \cdot \frac{dN}{dx}$. The step length L might be limited by specifying a maximum average number of Čerenkov photons created during one step. The spectral range of the Čerenkov photons created is limited to the energy range in which the index of refraction of the simulated material is specified. The energy is sampled from the density function

$$f(E) = [1 - \frac{1}{n^2(E)\beta^2}]. \tag{7.3}$$

The energy loss, $\Delta E_{loss} =< E > \frac{d^2N}{dEdx}\Delta E\Delta x$ of a charged particle due to the emission of Čerenkov light is in the keV range.
A simplified sketch of the momentum and polarization of a Čerenkov photon in the simulation is shown in figure 7.1. The photon polarization is assigned to be linear and perpendicular to the photon's momentum, while the azimuthal angle ϕ is uniformly distributed between 0 and 2π.

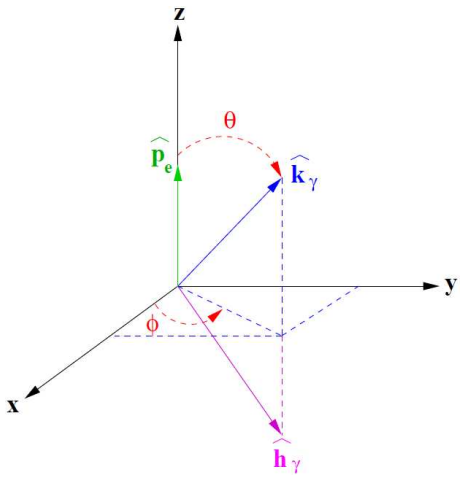

Figure 7.1: Čerenkov polarization (h_γ) and photon momentum (k_γ) with respect to an incident electron in Geant4 [52].

Scintillation Process Several empirical quantities of scintillating materials have to be provided by the user. The most important one is the characteristic light yield which is the effective number of scintillation photons created per energy deposit of the traversing particle. This material dependent number follows a Poisson distribution. The statistical yield fluctuation is either broadened due to impurities for doped crystals or narrowed as a result of the Fano factor [53]. In addition an emission spectrum with one or more exponential decay time constants has to be provided. The scintillation light is isotropically emitted along the track segment with a random linear polarization. The number of scintillation photons emitted is proportional to the energy loss and is usually in the range of several thousands per MeV.

7.1.3 Surface Concept

To understand the idea behind the surface models implemented in Geant4 some preliminary remarks are necessary. In the case of a perfectly smooth interface between two dielectric materials the probabilities for Fresnel reflection (R), including total internal reflection, or refraction ($T = 1 - R$) are calculated. The calculation relies on the photon's wavelength, its angle of incidence and its polarization as well as the refractive indices of the two touching materials. In case the photon encounters an interface of a dielectric and a metal-like material, it can not be transmitted. It will be reflected or absorbed instead. A metal-like surface is therefore chosen to simulate the MPPC's sensitive surface. Optical photons are absorbed depending on the provided photo detection efficiency of the sensitive surface.

In all other cases the optical boundary process as implemented in Geant4 relies on the concept of *surfaces*. Different approaches are available in Geant4 to simulate boundary processes according to the surface roughness and other requirements. For the simulations presented in this work the UNIFIED model [54] was chosen which is

adopted from the DETECT program [55]. Its major advantage compared to other surface models is the possibility to simulate a reflective foil.
The model assumes that a rough surface is a collection of micro facets, whose combination lead to a particular surface roughness (figure 7.2). Every time a reflection or refraction process of a photon occurs at a surface with a *global normal* $\hat{n}_g$ the local surface normal (or *facet normal*) $\hat{n}_f$ of the respective facet is randomly determined. The local surface normals fluctuate around the global surface normal: $\hat{n}_g \equiv \hat{n}_{<f>}$. The micro facets themselves are regarded to be smooth at scales comparable to the considered optical photon wavelengths.

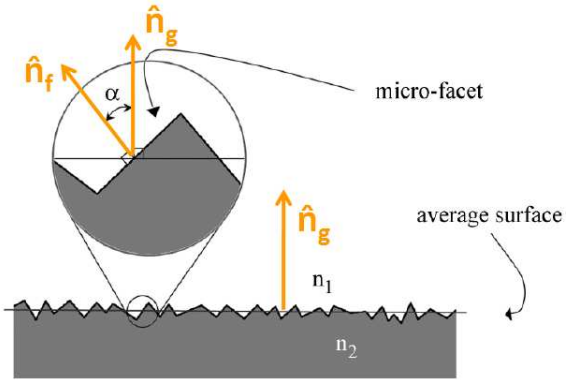

Figure 7.2: Simplified drawing of the optical surface concept in Geant4 [56].

The surface roughness is modeled assuming that the angle α between the facet normal $\hat{n}_f$ and the global surface normal $\hat{n}_g$ is following a Gaussian distribution with a mean of $\alpha = 0$ and a deviation σ_α. The normal of the micro facets is randomly chosen according to this distribution where the empirical value of σ_α has to be provided by the user in advance. Under the restriction $\alpha < 90°$, $\hat{n}_f$ is chosen such that:

$$\hat{n}_f = (\sin\alpha\cos\phi, \sin\alpha\sin\phi, \cos\alpha), \tag{7.4}$$

where ϕ is uniformly distributed and randomly chosen between 0 and 2π.
Afterwards it is determined whether the photon undergoes internal reflection, refraction or is absorbed at the boundary.
Four different boundary reflection mechanisms are comprised in the UNIFIED model. They are set dependent on the wavelength of the initial photon, but assumed to be independent on the incident angle. They are differentiated by the normal around which the reflection process occurs and their characteristic radiant intensities (figure 7.3). One of them, the *specular lobe* constant C_{sl}, represents the reflection probability about the local normal $\hat{n}_f$ of a micro facet. The *specular spike* constant C_{ss}, in turn, illustrates the probability of reflection about the average surface normal $\hat{n}_g$. In both cases reflection and refraction processes are calculated according to Snell's law about the respective normal. The *diffuse lobe* constant C_{dl} defines the probability of Lambertian reflection around the average surface normal $\hat{n}_g$. Lambert's law says

that the radiant intensity observed from any angle is the same in case of an ideal Lambertian reflector. The radiant flux density is directly proportional to the cosine of the angle θ between the observer's line of sight and the surface normal. Finally the *backscatter spike* constant C_{bs} describes the case of several reflections within a deep grove with the final result of exact back scattering in the initial direction which is possible in case of surfaces subject to high impurities.

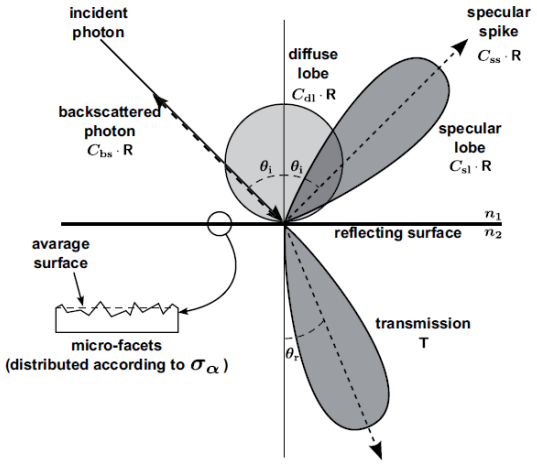

Figure 7.3: Radiant intensities in the UNIFIED model for a photon incidence under the angle θ_i [57].

The four parameters have to add up to uniformity: $C_{sl} + C_{ss} + C_{dl} + C_{bs} = 1$. As default 100% diffuse lobe reflection is used, if none of the other parameters is set. In any other case the reflection type is determined by a uniformly distributed random variable r between 0 and 1 as visualized in figure 7.4. For this study the four pa-

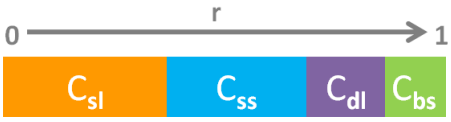

Figure 7.4: Determination of the reflection type occurring at a boundary through a randomly chosen variable r between 0 and 1.

rameters were assumed to be independent of the photon's energy. The exceptional case of a perfectly smooth surface ($\hat{n}_g = \hat{n}_f$) is defined through $C_{ss} = 1$. All other parameters, including σ_α, are ignored or rather trumped.
Furthermore the UNIFIED model offers the possibility to simulate a reflective coating. It is differentiated between a wrapping with an infinite small gap between the solid and the reflector and a reflective painting where no such gap is included. Only the former case was used in the simulations for this study, where the gap was filled with air. Within the Geant4 framework the possibility of multiple reflections in between the air gap is implemented until the photon is refracted back into the

tile or is transmitted out of the assembly and *deleted*. This enlarges the number of reflections per optical photon to an unphysical quantity. In the case of a reflective wrapping the described five surface parameters are only related to the interface of the solid and the air gap. The reflector itself is defined by its reflectivity R and the kind of reflection occurring at its surface. Either 100 % Lambertian ($C_{dl} = 1$) or specularspike reflection ($C_{ss} = 1$) can be chosen for the reflector. R was set to 98 % during all simulations over the entire energy range.

By default only a combination of a polished surface with a mirror-like reflector or of a rough surface with a Lambertian reflector is possible within the Geant4 framework. That also a mixture of those settings can be achieved will be shown in section 7.3.

7.2 Radiometric Definitions

In this section definitions of radiometric terms are given, that are useful in the study of surface reflections. The way light is reflected by a surface is dependent on the microscopic characteristic of the surface. A smooth surface, where surface irregularities are small compared to the wavelength of the incident light, will reflect light in a single direction. A rough surface will tend to scatter light in various directions, in some maybe more often than in others. A first attempt to differentiate between rough and smooth surfaces was made with the *Raleigh criterion* that is based on the phase difference of two reflected light rays at the point of detection.
A detailed description can be found in [58].
The indices of refraction of two media are related by *Snell's law* with the incidence (θ_i) and transmission (θ_t) angles by $n_i/n_t = \sin\theta_t/\sin\theta_i$. If the incident medium features the larger index of refraction the transmission angle is increased. If it approaches 90° at a critical incident angle $\theta_{crit.}$ there will be total internal reflection (figure 7.5): $\sin\theta_{crit.} = n_t \sin(90°)/n_i$.

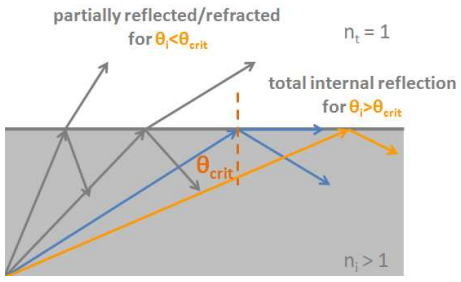

Figure 7.5: Principle of total internal reflection for incident angles larger than a critical angle $\theta_{crit.}$

For incident angles smaller than the critical angle, the fraction of incident electromagnetic energy that is reflected or refracted, depending on the polarization of the incident light and the electrical properties of the surface medium, is described by the

well-known *Fresnel's equations* derived from the classical description of monochromatic plane waves and the *Maxwell equations*:

$$r_\perp = -\frac{n_i \cos\theta_i - n_t \cos\theta_t}{n_i \cos\theta_i + n_t \cos\theta_t} \quad \text{and} \quad r_\parallel = \frac{n_t \cos\theta_i - n_i \cos\theta_t}{n_t \cos\theta_i + n_i \cos\theta_t} \tag{7.5}$$

$$t_\perp = \frac{2n_i \cos\theta_i}{n_i \cos\theta_i + n_t \cos\theta_t} \quad \text{and} \quad t_\parallel = \frac{2n_i \cos\theta_i}{n_t \cos\theta_i + n_i \cos\theta_t} \tag{7.6}$$

The reflection and transmission coefficients, r and t respectively, for parallel ($\parallel$) and perpendicular polarization ($\perp$) of the incident photon, are fractional amplitudes and have to be squared to get the fractional intensities. For a detailed derivation of the equations the reader is referred to [59].
For normal incidence ($\theta_i = 90°$), the reflection losses per interface derived from the Fresnel's equations are simplified to:

$$R_F = \frac{(n-1)^2}{(n+1)^2}, \tag{7.7}$$

with $n = \frac{n_i}{n_t}$, the ratio of the indices of refraction of the tile sample and the surrounding medium.

Under the restriction that the number of photons has to be conserved, the probability for a photon to be reflected or refracted can be calculated. The number of photons is proportional to the energy flux at the boundary, which is given by the *Poynting vector* $\vec{S}$:

$$\vec{S} = \frac{1}{2}\frac{c}{4\pi}\sqrt{\mu\epsilon}\vec{E} \times \vec{H} \qquad [51], \tag{7.8}$$

where ϵ and μ are the permittivity and the permeability of the medium, respectively. The energy balance on an unit area of the boundary surface requires that:

$$S\cos\theta_i = S_t \cos\theta_t + S_r \cos\theta_r, \text{ with } \theta_i = \theta_r \tag{7.9}$$

depending on the angle of incidence θ_i. The transmission probability for a photon then is as follows:

$$T = \left(\frac{E_0'}{E_0}\right)^2 \frac{n_t \cos\theta_t}{n_i \cos\theta_i} \qquad [51], \tag{7.10}$$

where E' corresponds to the medium the photon is transmitted into ($n_t = 1$ for air). The corresponding reflection probability is $R = 1 - T$. Therefore the smaller the incident angle is the higher is the refraction probability for a photon.
Note that the local incident angle of a photon might differ from the global angle of incidence, according to the difference of the local facet surface normal and the mean global normal relative to the average surface of all micro facets.

7.3 Parameter Scan

Due to the large amount of parameters that have to be set manually to simulate surface roughness and reflection types correctly within the Geant4 UNIFIED model a parameter scan was performed. It is intended to determine the effect on the absolute number of detected Čerenkov photons by varying one of the parameters. The goal of this analysis next to knowing the sensitivity of the Monte-Carlo simulation was to be able to estimate its errors induced by the variation of different parameters.
The parameters that were changed in small steps were: σ_α, specular lobe (C_{sl}), specular spike (C_{ss}) and backscatter (C_{bs}). All of them can take values between zero and one. While one parameter is varied the others stay fixed.
The Geant4 default parametrization is defined as 100 % diffuse reflection ($C_{dl} = 1.0$). Since the four constant parameters C_{dl}, C_{sl}, C_{ss} and C_{bs} have to add up to one, the diffuse lobe constant C_{dl} is chosen to act as a compensation when changing one of the other three parameters. With increasing values of C_{sl}, C_{ss} or C_{bs} those for C_{dl} decrease in the same manner. That's why no separate scan was made of C_{dl}.
As setup a rectangular sapphire tile was chosen, featuring the dimensions of the tile measured at test beam and readout in the configuration Pos_{opp} (figure 6.1 (left)). The characteristic photon detection efficiency of the MPPC was set to one for all photon energies to show the impact of varied parameter values independently of the MPPC type used. As a consequence the number of detected photons in this special case is nothing else than the number of photons hitting the 9 mm^2 large sensitive surface of the MPPC. For each configuration 10 000 positrons traversing the tile were simulated.
Note that Čerenkov light propagates in a distinct forward direction and thereby influences the observable outcome.
The gained results are plotted in graphs with the parameter settings on the x-axis and the tile response in terms of light yield on the y-axis. For this purpose the most probable value (MPV) of the obtained Čerenkov signal is fitted with a Landau function (figure 7.6) and represented by one point in the final graphs. Detailed information about the light yield distributions of each point can be found in the appendix of this thesis (section 10.2).

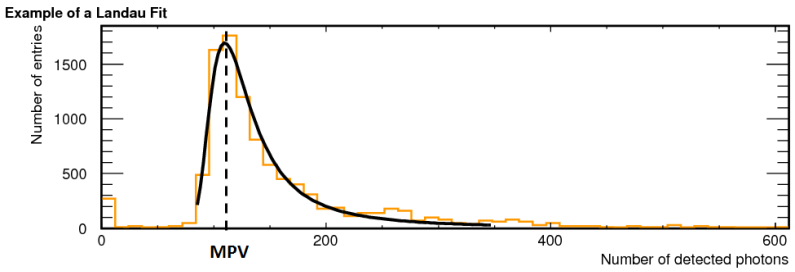

Figure 7.6: Number of Čerenkov photons detected for an arbitrary parametrization and fitted with a Landau function. The MPV was found to be 112 p.e./MIP with a sigma of 12 p.e./MIP

Parameter Scan of σ_α

As parameter to start with σ_α was chosen which determines the surface roughness. During those runs 100 % specular reflection around the micro facet normal was chosen ($C_{sl} = 1$) to emphasize the design of the tile surface assembled of micro facets. A comparison of all gained MPV's for the scan of σ_α can be seen in figure 7.7. Four

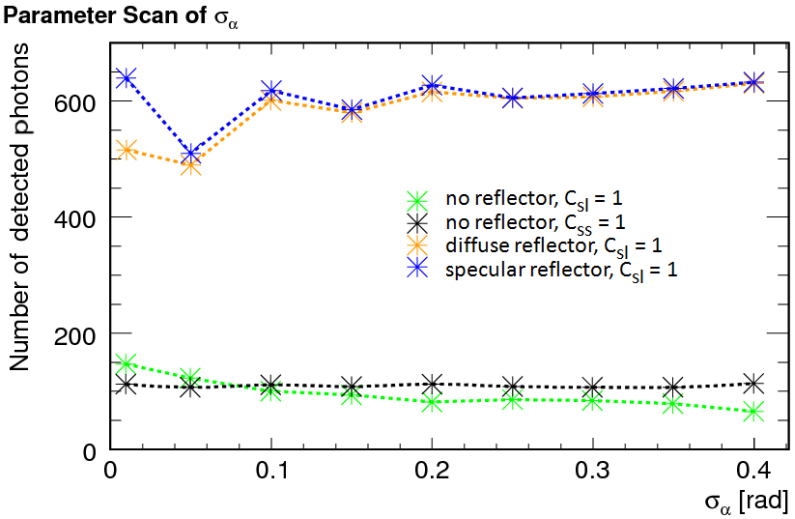

Figure 7.7: The mean number of detected photons for different configurations is plotted versus the value of σ_α in radian.

different cases are investigated: one surface only defined by $C_{sl} = 1$ without any reflector and another two with either a diffuse or a specular reflector. As a cross-check one surface is declared as polished, with $C_{ss} = 1$ (black line). The designation polished for a surface finish trumps any specification related to the probabilities of the various UNIFIED model reflections and hence also the specification of σ_α to sample the micro facet normal. The simulated mean light yield in this case remains constant. The outcome of a perfectly smooth surface will therefore be indicated as a reference line at the determined mean of (109 ± 3) p.e./MIP. The small variation is due to statistical fluctuations and would decrease for higher statistics.
Concerning the other three lines, the most apparent fact is the difference between a tile without or with a reflective coating. By using a reflective foil one can gain an increase in light yield of a factor of ∼4 - 6. The width of the Landau distribution also increases by a factor ∼3 if a reflective foil is used (see appendix 10.2).
Without a reflector (green line) the number of detected photons decreases with increasing σ_α. This shows that for rough surfaces more photons are lost due to Fresnel refraction at the tile boundary. This phenomenon is compensated in case of a reflective wrapping (orange and blue line) and the transmitted photons are partially reflected back into the tile resulting in a higher absolute light yield. The light yield varies for values of σ_α larger than 0.2 around a rather constant mean of (617 ± 15) p.e./MIP no matter if a diffuse or a specular reflector is used.

The large fluctuations in the light yield for configurations where the surface finishing is manually set to polished by reducing the surface roughness to very small values ($0.01 \leq \sigma_\alpha \leq 0.1\,\text{rad}$) is not understood completely. Feedback was given to the Geant4 developers [60] and the observed problem will be revised. It is assumed that for such small values of σ_α, problems occur at a stage in the code where the facet's normal is determined. Confirming this assumption is the fact that for values of $\sigma_\alpha < 0.1\,\text{rad}$ a higher output is achieved for an almost perfectly polished surface (green curve) then for a surface that is declared in advance as perfectly polished (black line). The data points within this σ_α range should overlap.

Summarized this means, that for a polished surface (values of $\sigma_\alpha \leq 0.1\,\text{rad}$) the probability for internal reflection processes is higher than in the case of an unpolished surface, where many photons are refracted out of the tile. This can be explained with the definitions given in the previous section. The critical angle for total internal reflection of sapphire is $\theta_{crit.} = \arcsin 1/1.76 = 90° - \arccos 1/1.76$. A photon radiated through the Čerenkov effect is much likely to undergo total internal reflection in case of a polished surface (figure 7.8). With an increase in the surface roughness, the average incident angle of the photons decreases and refraction becomes more probable.
By adding a reflective coating those beforehand lost photons can be reflected back into the tile. This explains why a reflective foil has a slightly higher impact on rough surfaces than on polished ones.

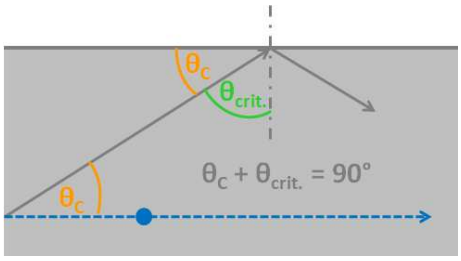

Figure 7.8: Geometrical relation between the Čerenkov angle θ_C and the critical angle $\theta_{crit.}$ for total internal reflection.

Parameter Scans of the Reflection Types

While scanning the parameters related to the type of reflection, considering the above gained insights, σ_α was chosen to be 0.2 rad for rough surfaces and 0.02 rad for surfaces that should be simulated as polished. A perfectly polished surface with $\sigma_\alpha = 0$ was assumed to be unrealistic. This agrees well with the results found in [56].
The starting point for every simulated parametrization is the same with $C_{dl} = 1$ and accordingly the varied parameter set to zero. Each scan was done for four different surface finishings of the rectangular sapphire tile: one rough and one polished surface ($C_{ss} = 1$) without reflector, and a rough and a polished (manually created

through the small value of σ_α) surface wrapped with a diffuse or a specular reflector respectively.

Specular Lobe Constant C_{sl} The first reflection parameter scanned was C_{sl} (figure 7.9). The parameters C_{ss} and C_{bs} are set to zero and C_{dl} is varied to fulfill the restriction of $C_{sl} + C_{ss} + C_{dl} + C_{bs} = 1$. Excluding the unwrapped, polished

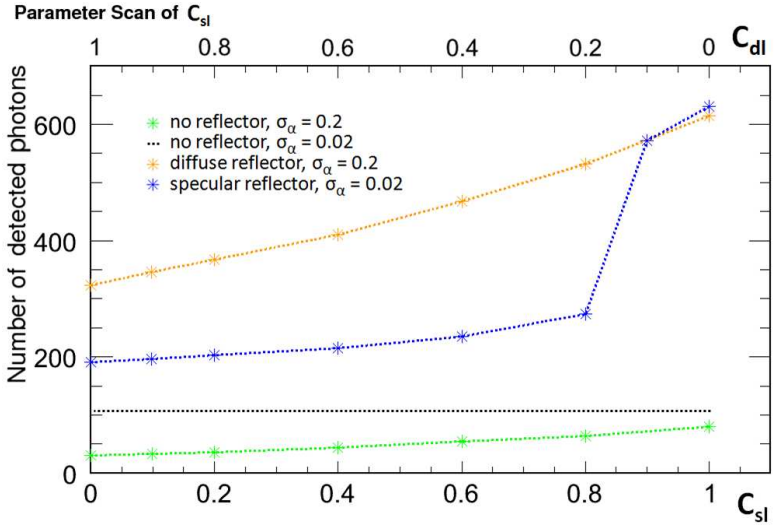

Figure 7.9: The mean number of detected photons for different surface configurations is plotted versus the value of C_{sl} ranging from 0 to 1. $C_{ss} = C_{bs} = 0$.

surface (black reference line), all other configurations show the same behavior: with a higher probability for specular reflection C_{sl} around the local micro facet normal $\hat{n}_f$ and accordingly a lower probability for internal diffuse reflection C_{dl} around the average surface normal $\hat{n}_g$, the mean light yield increases. This is due to the fact that internal diffuse reflection minimizes the probability of a Čerenkov photon reaching the MPPC. Specular reflection in contrast leads to forward reflections towards the MPPC. That is why for $C_{sl} = 1$, and no reflector simulated, the resulting signal amplitudes of a rough approach those of a perfectly polished surface.
The effect is most apparent in the case of a polished surface wrapped with a specular reflector. An increase in the mean light yield of almost 70 % can be observed from 100 % internal diffuse reflection ($C_{dl} = 1$) to 100 % specular reflection ($C_{sl} = 1$). Generally, if C_{sl} reflection is the probability sampling result for the reflection type at the interface crystal-air gap, the micro facet normal is sampled from the Gaussian distribution defined by σ_α. For a specular reflector wrapped around a polished surface, this means that by setting C_{sl} to values $\geq$0.9, a depolished surface with a specular reflector is artificially created. This is how a mixing of the two default combinations of surface and reflector type can be achieved.
The impact of using a reflector as wrapping decreases from a factor of approximately 10 to a factor of 7.5 in case of rough surfaces with increasing specular reflection

around the local micro facet. Consequentially less photons are refracted out of the tile for higher C_{sl} values. For polished surfaces the opposite behavior appears. With increasing values of C_{sl}, the impact of the reflector rises there from a factor ~ 1.7 to ~ 5.7 because the surface is treated more and more as a rough surface.

Specular Spike Constant C_{ss} The parameter scan is continued with the reflection type C_{ss} and the same simulation adjustments as before, except now the parameters C_{sl} and C_{bs} were set to zero. The results are displayed in figure 7.10. For a

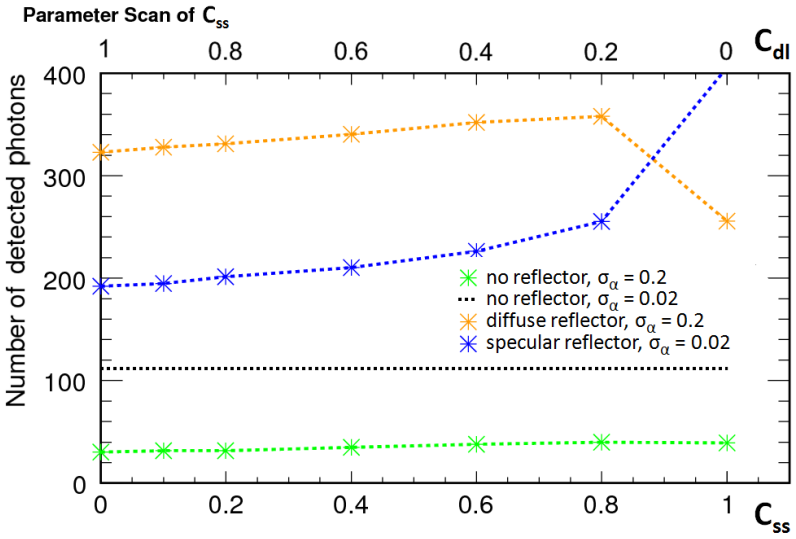

Figure 7.10: The mean number of detected photons for different configurations are plotted versus the value of C_{ss} ranging from 0 to 1. $C_{sl} = C_{bs} = 0$.

depolished surface without reflector the difference between zero and 100 % specular reflection around the global surface normal ($C_{ss} = 1$) is close to 23 %. In principle, setting C_{ss} to one should artificially create a polished surface out of a rough surface by ignoring σ_α. All light should be reflected around the global surface normal as in case of a perfectly smooth surface. This explains the receding impact of the diffuse reflector wrapped around a rough surface from a factor of ~ 10.6 to ~ 6.5 (orange line), but the expected behavior for an unwrapped, rough surface can not be observed. In this case as well feedback is forwarded to the Geant4 developers [60]. It is assumed that the problem in the simulation is similar to the other phenomenon observed. The propagation of an optical photon is computed in the following succession: first the facet normal is sampled according to the value of σ_α, then it is decided whether reflection or refraction occurs and not until then the reflection type is sampled. Therefore the light yield of a rough surface will never converge to the one of a polished surface, even for $C_{ss} = 1$.
A value of $C_{ss} = 1$ is responsible for the kink of the curve for a rough surface wrapped with a diffuse reflector. It was assumed that at this point the opposite mixing of the default combinations of surface finishing and reflector type is achieved: a pol-

ished surface is wrapped with a diffuse reflector. Considering the before mentioned problem this might not be the case but has to be revised.

Backscatter Constant C_{bs} The last parameter whose effect on the output was investigated is the reflection type C_{bs}. The number of detected photons declines for all configurations, besides the one for a polished surface, with rising C_{bs} values (figure 7.11). The strongest impact of up to 95% is observed on a rough surface with a diffuse reflector. The value of σ of the Landau fits is reduced by a factor of ~2 - 3. This particular reflection type results in a photon reflected back the same way it arrived at the surface. Thereby the probability of a photon reaching the sensitive detector surface is lowered and even smaller than in case of diffuse internal reflection where at least 50 % of all reflections occurring turn out with a forward reflection. In case of such small σ_α values of 0.02 and 0.2 a backscattering reflection seems more unrealistic compared to the other reflection types.

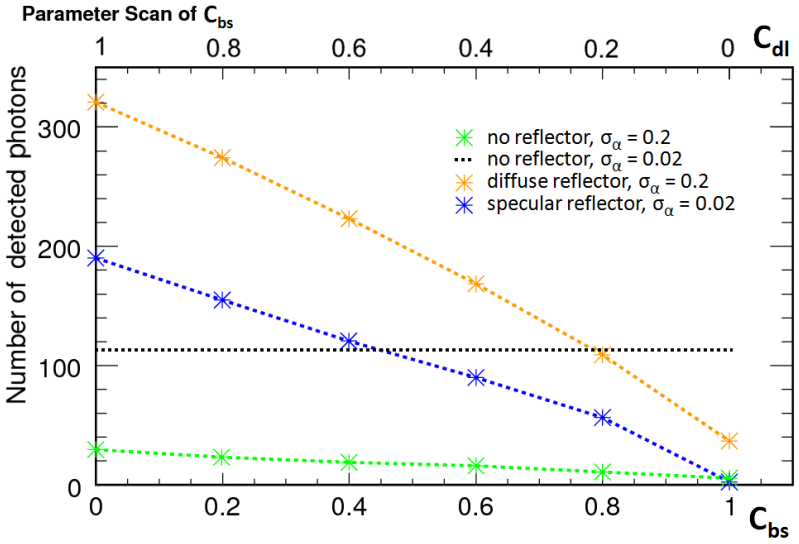

Figure 7.11: The mean number of detected photons for different configurations are plotted versus the value of C_{bs} ranging from 0 to 1. $C_{sl} = C_{ss} = 0$.

8 Monte-Carlo Studies with Geant4

To make accurate predictions of possible detector setups, the different configurations measured at test beam are tried to reconstruct via simulation. All simulated Čerenkov tiles were shaped according to the dimensions available at test beam (table 5.1) and the parametrization is chosen based on the results of the previous section. Since the focus lies on the signal response of the Čerenkov tile there is no additional scintillator tile simulated.

Parametrization of the Simulated Configurations

Based on the results found with the parameter scan this subsection shall give a compact overview of the parameter settings chosen for the Monte-Carlo simulation. According to the percental change in the number of detected photons the errors are estimated.
By allocating more weight from the internal diffuse reflection C_{dl} to one of the probability constants C_{sl} or C_{ss} the signal response increases or decreases only slightly as long as C_{dl} is not completely switched off. The greatest change is seen in all cases when a 100% C_{sl} or C_{ss} reflection was forced. Not so in the case of C_{bs}. There, a continuous decrease of the light yield for all configurations is observed.
At test beam two possible surface configurations were tested. Either polished or unpolished tiles were wrapped with a specular reflector of 98% reflectivity and a small layer of air between tile and reflector. In case of a rough surface and a specular reflector the demonstrated mixing of the default combinations of surface finishing and reflector type has to be used. Table 8.1 gives an overview of the parameter settings for the Monte-Carlo simulation. For the first setting of a polished surface

Surface Finish	σ_α **[rad]**	$\mathbf{C_{dl}}$ **[%]**	$\mathbf{C_{sl}}$ **[%]**	$\mathbf{C_{ss}}$ **[%]**	$\mathbf{C_{bs}}$ **[%]**
polished	0.02	0.2	0.15	0.6	0.05
unpolished	0.2	0.0	0.9	0.05	0.05

Table 8.1: Surface parametrization as chosen for Monte-Carlo simulations with Geant4 for a polished and an unpolished surface wrapped with a specular reflector.

wrapped with a specular reflector the weight is shifted towards C_{ss} reflections. If C_{ss} in this case is chosen to be between 0.0 and 0.8 it varies around a mean of 213 p.e./MIP by ±12%. The chosen value of 0.6 still lies within this region. Since C_{sl} and C_{bs} reflections are chosen to be quite small in case of a polished surface, C_{dl} is set to 0.20. C_{sl} varies between 0.0 and 0.8 around a mean of 219 p.e./MIP by

$\pm 15\%$ and $C_{bs} = 0.05$ reduces the light yield by $\sim 5\%$. The second configuration with a depolished surface and a specular reflector is created artificially by setting C_{sl} to 0.9. As a consequence almost no free space is left for adjusting the other reflection parameters.
Since those values are only an estimation and can not be verified by measurements within the scope of this study, an error estimation has to be made. The total uncertainty $\Delta\Sigma$ of the following simulation results is composed of the uncorrelated errors of the parameters σ_α, C_{sl}, C_{ss} and C_{bs}:

$$\Delta\Sigma = \Delta\sigma_\alpha \oplus \Delta C_{sl} \oplus \Delta C_{ss} \oplus \Delta C_{bs}. \tag{8.1}$$

C_{dl} is excluded from this calculation since it is a function of the other three reflection parameters. Table 8.2 gives an overview of the errors estimated for the individual parameters as well as their sum. Final errors of 12.4 % in case of a polished surface and of 16 % in case of a rough surface are calculated. The difference between those values originates from the differing light yield sensitivity for certain parameter ranges. These errors are used as an uncertainty estimation of the Monte-Carlo simulations.

Surface Finish	$\Delta\sigma_\alpha$ **[%]**	$\Delta\mathbf{C_{sl}}$ **[%]**	$\Delta\mathbf{C_{ss}}$ **[%]**	$\Delta\mathbf{C_{bs}}$ **[%]**	$\Delta\Sigma$ **[%]**
polished	± 10	± 3	± 5	± 4.5	$\pm$**12.4**
	(0.01-0.05)	(0.05-0.25)	(0.5-0.7)	(0.0-0.1)	
unpolished	± 3	± 15	± 1	± 4.5	$\pm$**16.0**
	(0.1-0.3)	(0.85-0.95)	(0.0-0.1)	(0.0-0.1)	

Table 8.2: Error estimation for the Monte-Carlo studies based on the results found by the parameter scan. The parameter ranges from which the errors are derived are given in brackets.

Simulated Geometries

According to the geometrical setup of the tiles at test beam, in the simulations the long axis of the tiles is aligned in parallel with the beam axis. The origin of the coordinate system lies in the center of the Čerenkov tile. The tile length is described by the z-coordinate, the width and height by the abscissa and the ordinate respectively. A picture of the simulated geometries is shown in figure 8.1. The mother volume in which the tiles are placed is filled with air. In order to simulate one side of the rectangular tile as polished, an extra sapphire volume of a very small thickness (0.1 mm) is added to the geometrical arrangement (light blue). Its outer surface facing the surrounding mother volume is polished using the same parametrization as for completely polished tiles. The three rhombic tiles consist of two aligned trapezoids made of the identical material (sapphire or lead glass). By defining the boarder between those two solids as perfectly polished, none of the possible optical boundary processes occurs and the two assembled trapezoids behave

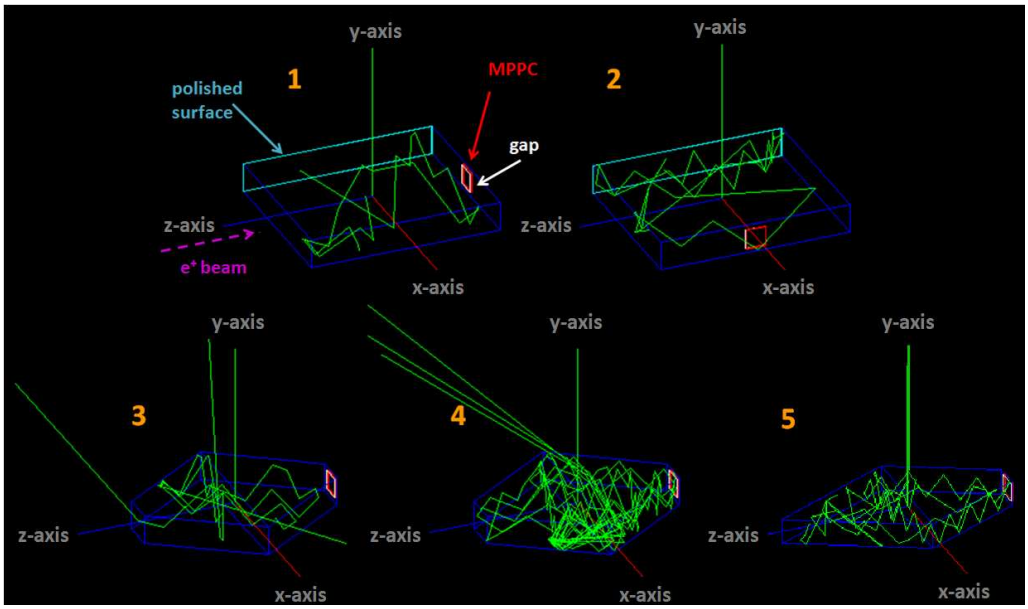

Figure 8.1: The five tile configurations as simulated with the Geant4 software package. The produced photons are colored in green, the air gap is white and the MPPC is visualized in red (the initial electron is not visible). **Top:** Rectangular sapphire tile with the MPPC positioned at Pos_{opp} (1) and Pos_{lat} (2). **Bottom:** Rhombic sapphire tiles with a rough (3) and a polished (4) surface finishing and the polished lead glass tile (5).

as one rhombohedron.
The primary particle is a positron with an energy of 3 GeV. The primary particle source, producing the positrons, is situated at (0|0|9.9) cm in the positive z-direction. The positron beam incidence is uniformly distributed in x and y over the entire height and width of the tiles. In case of the rhombic tiles this equal to their maximum transverse profile.
The produced photons are detected by a $3{\times}3{\times}0.2\,\mathrm{mm}^3$ large sensitive area (red) through a $3{\times}3{\times}0.1\,\mathrm{mm}^3$ thick gap filled with optical grease (white) with a constant refractive index of $\mathrm{n}_{grease} = 1.465$. The interface between the tile and the gap in front of the MPPC is always set to polished, whereas the interface of the MPPC and the gap is always defined as metal-like in order be treated as a sensitive surface. The pixelized substructure of a MPPC, considering also the fill factor of each pixel, is not taken into account in the geometrical design. The quoted numbers of the absolute light yield found by simulations within this study are not convoluted with the characteristic PDE of the MPPC. The results shown are obtained with $PDE = 1$, meaning that every photon is absorbed by the sensitive detector independent of its wavelength.

Material properties

To make accurate predictions of the detector behavior by simulation, one has to consider the properties of the different materials that were used for the measurements at test beam. The characteristic composition of the lead glass type used is given in table 8.3. The average values of each component were implemented in the

Compound	Percentage [%]
Lead Oxide	50 - 60
Silicon Dioxide	30 - 40
Potassium Oxide	0 -10
Sodium Oxide	0 - 10
Barium Oxide	<1
Arsenic Trioxide	0.2

Table 8.3: Composition of the lead glass type SF5.

simulation. The contribution from arsenic trioxide are assumed to negligible.
All optical material properties of sapphire and lead glass are defined over a wavelength range of 180 nm to 1000 nm (1.2 eV to 6.9 eV). Part of the needed data is provided by the manufacturers. The given values of the index of refraction for lead glass are not covering the complete wavelength range down to 180 nm. For the small wavelengths outside the available interval the values are linearly estimated (figure 8.2).

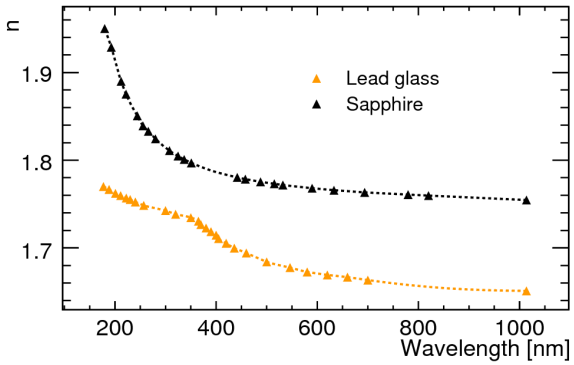

Figure 8.2: Refractive index of sapphire and lead glass as provided by the manufacturers [61, 48]. The values of lead glass are estimated for lower wavelengths than 300 nm.

In the simulations the absorption probability of the photons is computed according to the attenuation length. In case of lead glass the internal transmittance as a function of the sample thickness and the wavelength ($T_\lambda(x)$) is available. The data points of the transmission spectrum were converted into the attenuation lengths X_λ as follows:

$$T_\lambda(d) = e^{-\frac{d}{X_\lambda}} \Leftrightarrow X_\lambda = -\frac{d}{\ln T_\lambda}, \tag{8.2}$$

where d is the sample thickness at which the transmission has been measured by the manufacturer. The following figures show the transmission spectrum of lead glass provided by the manufacturer and the converted attenuation lengths as implemented in the simulations (figure 8.3). As a comparison the attenuation length of sapphire which was read from [61] is also shown. The transmittance of lead glass for wavelengths smaller than 300 nm was set to zero.
The attenuation lengths of the optical cement BC-630 are not defined in the simulation studies assuming 100 % transmission for all wavelengths.

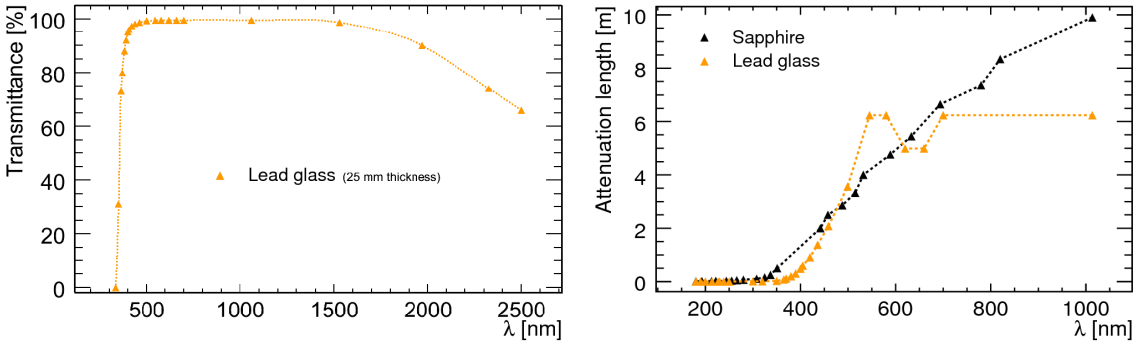

Figure 8.3: Transmittance and corresponding attenuation lengths of sapphire and lead glass [61, 48].

8.1 Results

For each of the explained configurations 100 000 positrons were simulated, uniformly distributed over the tile width, traversing the tiles in parallel to the z-axes. In the following several quantities are studied in detail in order to investigate the behavior of the produced Čerenkov photons inside the tiles. Some of the properties of the tested materials are compared to find the one most suitable for the detection of low-intensity Čerenkov light.

Wavelength Distributions

The simulated wavelength distributions for all tile configurations are compared in figure 8.4. The shape of the obtained wavelength spectra depends solely on the chosen material and not on the specific tile shape or MPPC readout position. The wavelength distribution of the produced photons is supposed to be proportional to $1/\lambda^2$ for all constellations:

$$\frac{dN^2}{d\lambda dx} = \frac{2\pi\alpha z^2}{\lambda^2} \sin\theta_C \tag{8.3}$$

The plotted spectra follow such a behavior and differ only according to the absolute number of produced photons. The part of the spectrum that is reabsorbed lies for sapphire between 180 nm and 420 nm, similar to lead glass which though absorbs

slightly more photons around 350 nm. The absorption range where photons are no longer transmitted through the tile, is also visible in the wavelength spectrum of the detected photons.Since this is a superposition of the first two distributions fewer photons are detected within wavelength ranges where the absorption rate is high.

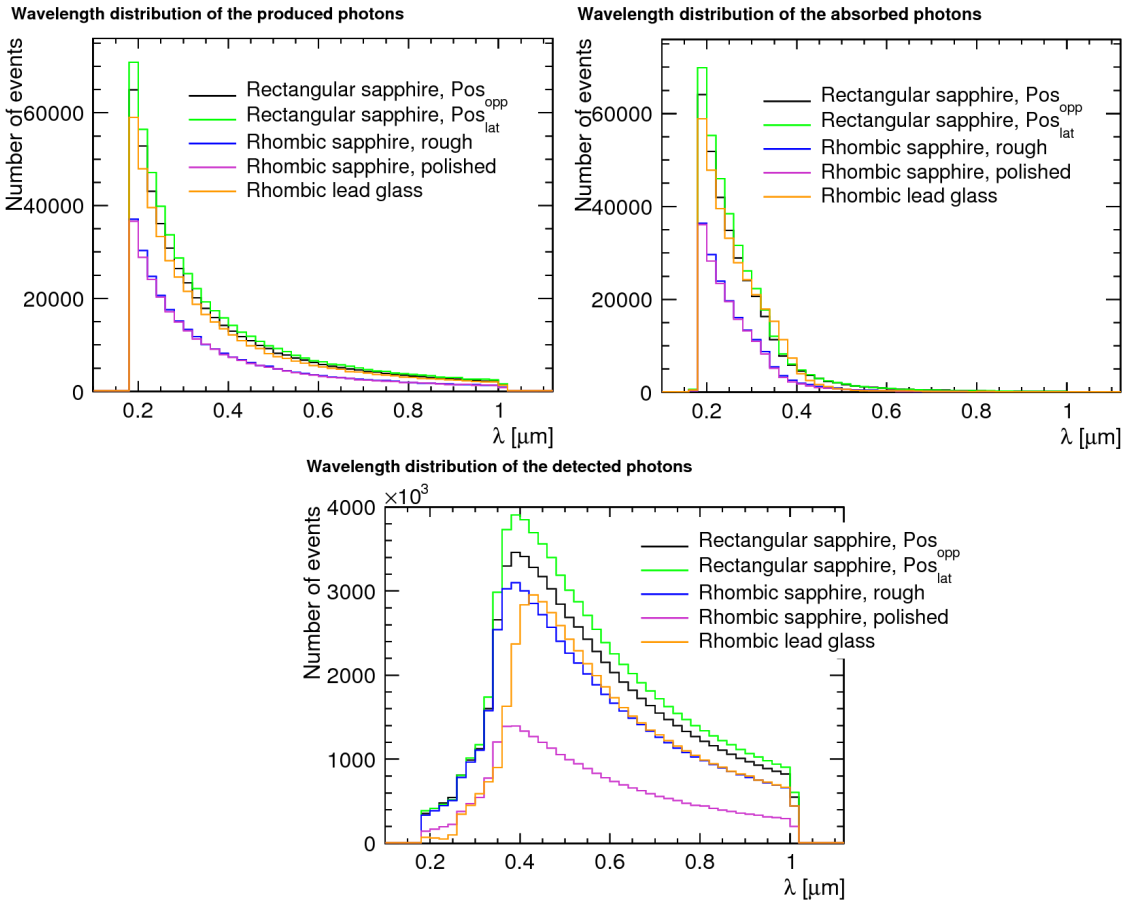

Figure 8.4: Wavelength distributions of the produced (**upper left**), absorbed (**upper right**) and detected (**bottom**) photons for all simulated configurations.

Produced and Absorbed Photons

Since the expected Čerenkov light yield is very low, materials that produce many and absorb few Čerenkov photons are favored. Both numbers increase with the density of the material. The number of absorbed photons though decreases within wavelength regions with a growing transmission probability. For sapphire and lead glass these two numbers are compared in figure 8.5 for the five different configurations. The mean of the each histogram is quoted. The two readout configurations of the rough, rectangular sapphire tile are depicted in one plot, since the number of

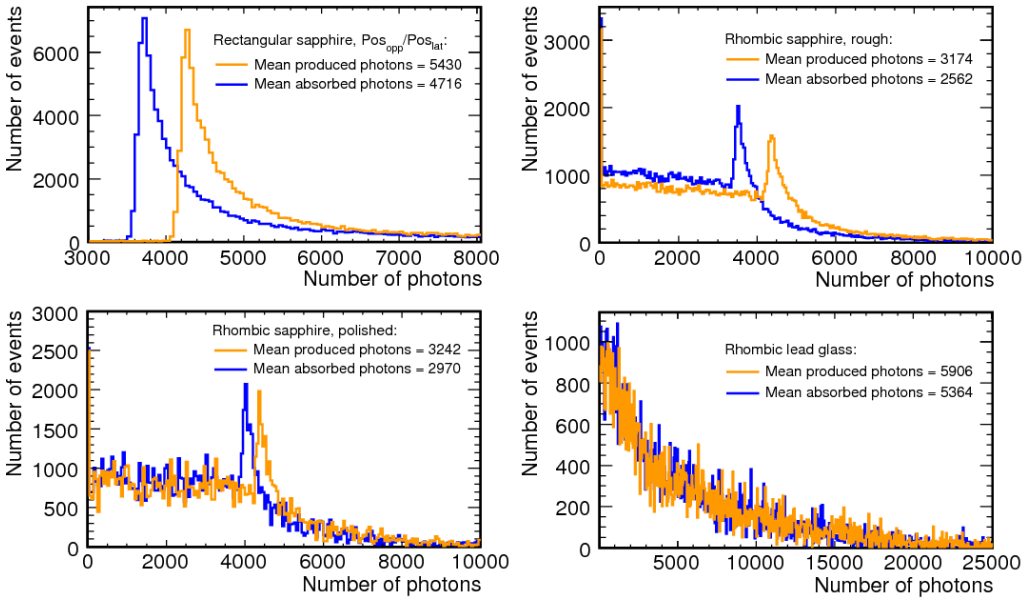

Figure 8.5: The number of produced (orange) and absorbed (blue) optical photons per event for every configuration simulated.

produced and absorbed photons is not influenced by the MPPC detection position. All distributions are characterized through a long Landau tail to high numbers of produced and absorbed photons. This gets the most distinct in case of lead glass. It is the denser material of the two studied and consequentially produces a higher number of photons with a large Landau tail of up to 25 000 photons per positron crossing the tile. However, numerous photons are reabsorbed by the material which leads to a number of detectable photons comparable to sapphire.
In case of the rectangular sapphire tile, on average approximately 700 photons can be detected. Since the positrons always traverse an equal amount of material less than 4000 photons are never produced and accordingly always more than 3400 are absorbed. Comparing the two rhombic sapphire tiles, in case of a polished surface finishing 14 % more photons get absorbed than for a rough surface finishing. Due to the higher probability of total internal reflection for a polished surface, the number of reflections increases and similarly the path length of a photon inside the tile. Therefore the probability for a photon to be absorbed increases. The observed constant production and absorption rates below the peak value can be explained by the symmetric tile shape. The number of produced photons is proportional to the amount of material passed and decreases thus for beam impacts outside the range of the maximum tile length. This maximum range accounts in case of the rhombic sapphire tiles for 18% of the whole tile width causing the visible peak in the distributions. The lead glass tile is having an acute opening angle which is why there is only one trajectory featuring a maximum length. Consequentially a peak is almost not distinguishable.

In figure 8.6 the number of produced photons as a function of the horizontal beam

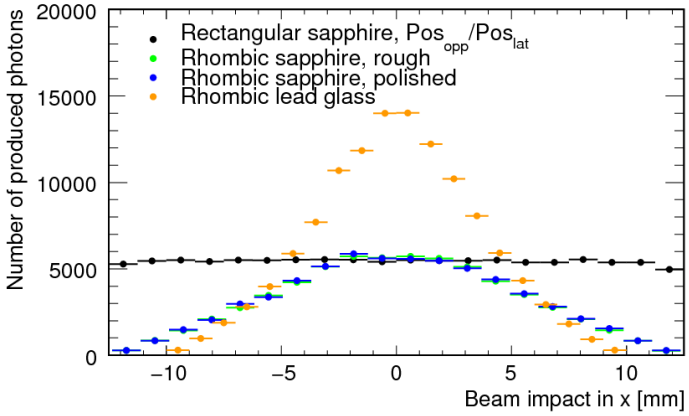

Figure 8.6: Distributions of the number of produced optical photons versus the beam impact in x [mm] for different materials.

impact is shown. The impact of different beam incidences in the vertical direction is assumed to be negligible, since the sensitive area of the MPPC almost matches the tile height. One point in the profile represents the mean number of produced photons for all vertical impacts corresponding to one horizontal beam impact. The statistical vertical errors are negligible.
Whereas in case of a rectangularly shaped tile, the distribution of produced photons is constant over the entire range, for all rhombically shaped tiles the dependence on the amount of traversed material and consequentially on the beam incidence is visible. If the positrons pass through the center of the rhombic tile (track length of ∼30 mm), they reach the same amount of produced photons as in case of the rectangular sapphire tile. The number of photons produced in lead glass is about a factor of three higher than for sapphire. One has to take into account that also the maximum track length is larger by 6 mm.

Detected Photons

The fraction of theoretically detectable photons is:

$$\gamma_{detectable} = \frac{\gamma_{prod} - \gamma_{abs}}{\gamma_{prod}}, \tag{8.4}$$

where the numerator is equal to the number of detected photons in case of PDE = 1. By studying different materials, adjusting tile shapes and MPPC readout positions, the ratio $\gamma_{detectable}$ can be improved. For the five configurations measured at test beam the number of detected photons γ_{det} per event is shown in figure 8.7 if PDE = 1 is set. The shape of the distributions resembles those obtained for the produced photons. If the MPPC is positioned at the lateral side of the rectangular sapphire tile (Pos_{lat}) a 10 % higher mean number of detected photons is obtained than if it is placed along the z-axes facing the beam impact point (Pos_{opp}). The advantage of a rectangular tile readout in the configuration Pos_{lat} is that the photon has to undergo

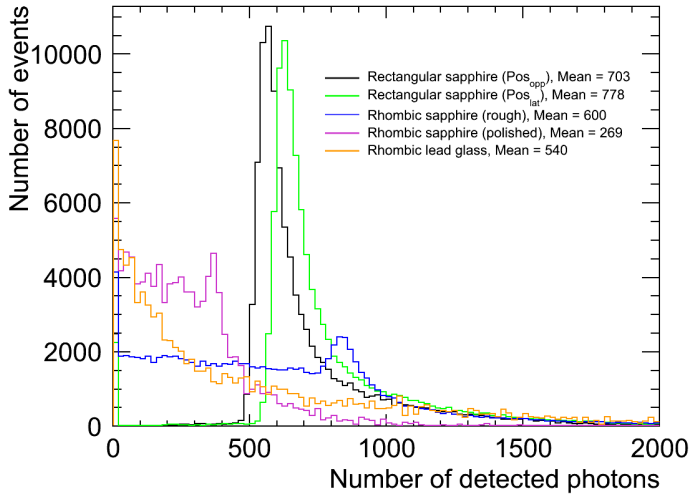

Figure 8.7: Number of detected optical photons for each event of every configuration simulated (PDE = 1). No correction is applied for the varying amount of material a positron traverses in case of rhombic tile shapes.

fewer boundary reflections and refractions until it reaches the sensitive surface of the MPPC.
The distribution of the rhombic sapphire tile with a rough surface peaks at an even higher value of ∼840 p.e./MIP, though the mean light yield is lower than in case of the rectangular tiles. A large difference can be seen in the spectra of the two rhombic sapphire tiles. While the mean light yield in case of a rough surface is about 18 % lower than for a rectangular sapphire tile, it decreases by 64 % if the rhombic sapphire tile is polished. As before this is due to the number of reflections and refractions occuring during the photon's path inside the tile. If the tile is polished, the number of absorbed photons is higher due to more boundary reflections. This reduces the light yield considerably.
The mean number of detected photons in lead glass decreases by approximately 26 % compared to the rectangular sapphire tiles due to the large number of absorbed photons. Nevertheless, the maximum achievable light yield of ∼950 p.e./MIP is about twice as high as for a rectangular sapphire tile and about 1.4 times higher than for a rhombically shaped sapphire tile. Figure 8.8 (left) shows the distribution of the detected photons as function of the horizontal beam impact and PDE = 1. The shape of these spectra resembles those shown before for the number of produced photons. This verifies the dependence of the light yield on the amount of produced photons at one particular position. The right plot in figure 8.8 contains the number of detected photoelectrons but in case of the three rhombic tiles corrected for the amount of material traversed by the positrons. The conversion takes the specific geometrical dimensions into account (see appendix). By applying the correction the number of detected photons increases at off-center positions in case of a rhombic tile shape. This flattens out the previous spectra.

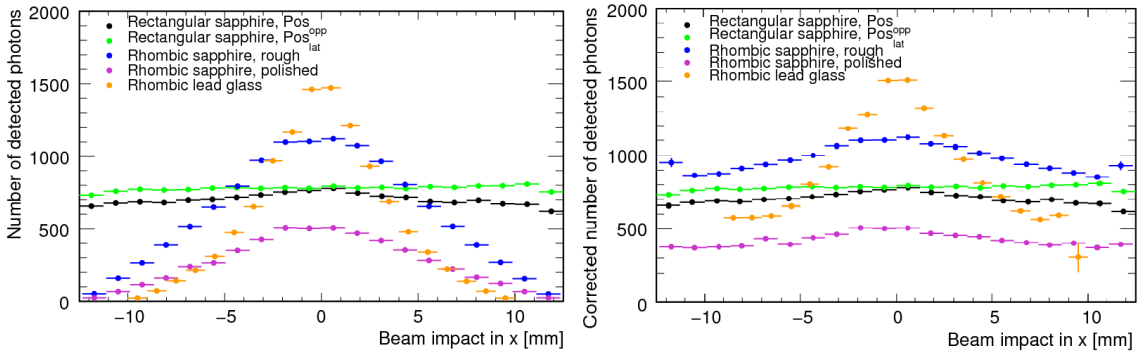

Figure 8.8: Distribution of the detected optical photons vs the beam impact in x [mm] for different materials (PDE = 1).

Non-uniformity

A quantity which is directly comparable to data without the superposition with the PDE of the MPPC is the non-uniformity of the tile response. Similar to experimental measurements the non-uniformity is defined as the percental deviation from the maximum light yield LY_{max}:

$$\text{Non-uniformity} = 1 - \frac{LY_{meas}}{LY_{max}}. \tag{8.5}$$

Figure 8.9 is obtained using this definition and the maximum light yield values found in figure 8.8. On the left the uncorrected values are plotted whereas on the right the length correction is applied. In the following only the corrected non-uniformity spectra are discussed. The lowest non-uniformity shows the rectangular sapphire tile if readout at the lateral side (Pos_{lat}). The overall non-uniformity reaches a maximum of approximately 15 % at the opposite side of the MPPC mounting position ($x = 12.5$). If the same tile is readout at $-1.5 < x < 1.5$ the non-uniformity increases up to 20 % at both sides of the tile. The non-uniformity of this configuration (Pos_{opp}) is always about a factor of 2 higher than for the first configuration (Pos_{lat}). The three rhombic tiles behave similar with a strong increase in the non-uniformity with a growing distance of the beam incidence to the MPPC readout position ($-1.5 < x < 1.5$). There difference between a rhombic sapphire tile with a polished or a rough surface becomes more obvious if the data points are corrected. The non-uniformity in case of a polished sapphire tile is a factor of 1.5 higher as if the same tile is depolished. Total non-uniformities of 35 % and 25 % are found for a polished and a rough rhombic sapphire tile respectively. The lead glass tile has in parts a non-uniformity which is twice as high as that of the rhombic sapphire tiles and ends up at about 65 %.
The very outlying data points show an unphysical behavior due to the binning of the histograms.

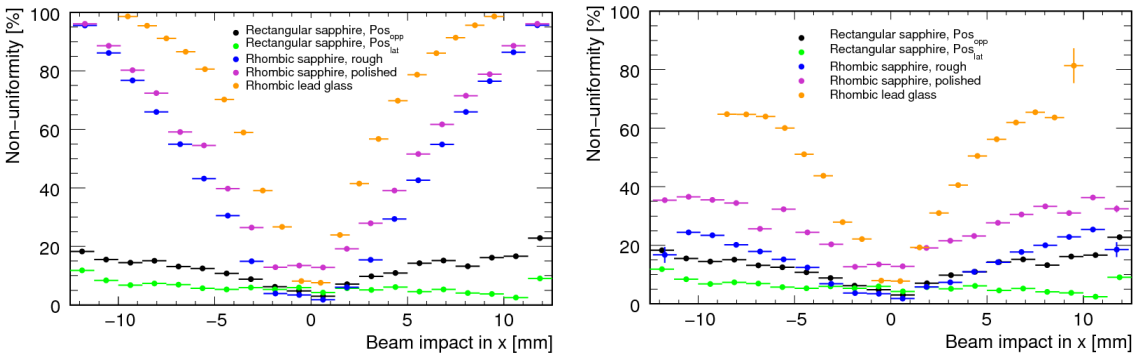

Figure 8.9: Non-uniformity of the signal response for the five simulated configurations versus the beam impact in x [mm].

Detection Efficiency

Another quantity, not measurable at test beam is the detection efficiency, which is defined as the ratio between detected and produced photons:

$$\text{Detection Efficiency} = \frac{\gamma_{det}}{\gamma_{prod}}. \tag{8.6}$$

This ratio is shown in figure 8.10 for all detected events. The fluctuations of the

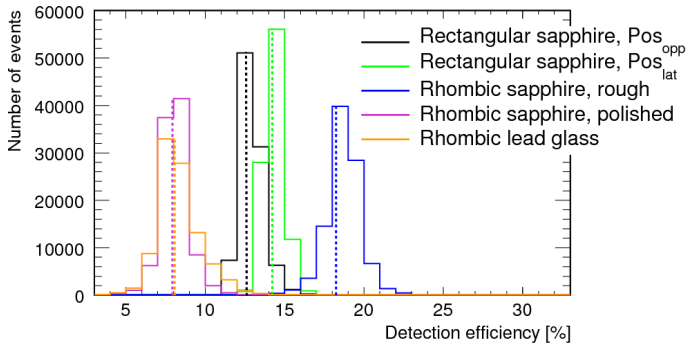

Figure 8.10: Distribution of the mean detection efficiency vs the beam impact in x [mm] (PDE = 1).

gained distributions can also be interpreted as a measure for the uniformity or non-uniformity of the signal response. In contrast to the before quoted values, here the distribution of the produced photons at every position in x, including the characteristic long Landau tail, is taken into account. This ratio is thereby independent of the varying material length of the rhombic tiles. It shows how efficient one of the five constellations is in detecting the produced photons. Clearly the best result is obtained in case of a rhombic sapphire tile with a roughened surface. With a mean at about (18.3±1) % it is much more efficient in the detection of the produced photons than all others. The second best detection efficiency is achieved for a rectangular sapphire tile, which is readout in the configuration Pos_{lat}.

The mean value is found at (14.1±0.5) %. A comparable detection efficiency is only reached for few events with a central incidence in case the same tile is readout at its center in the configuration Pos_{opp}. If the positron traverses the tile farer outside the detection efficiency decreases following a similar shape as the number of photons.
The worst mean detection efficiency of (8±2) % is found for the polished sapphire tile and the polished lead glass tile. In both cases this is caused by the large amount of reabsorbed photons. Due to the higher number of reflections at a polished boundary, the path length of the photons increases and hence the probability to be absorbed.

8.2 Conclusion

Based on a detailed parameter scan the simulation of optical photons with the Geant4 toolkit was accomplished. An applicable error was derived from the simulated light yield fluctuations as a function of the five parameters σ_α, C_{sl}, C_{ss}, C_{dl} and C_{bs}. The error was estimated to be 12.4 % if the surface is simulated as polished and 16 % in case of a rough surface.
Table 8.5 gives a final overview of the five configurations and all simulated quantities. The mean light yield LY_{mean} is the mean value of the entire histogram and the maximum light yield LY_{max} is the MPV obtained from a landau fit to the light yield spectra (figure 8.7). The mean of the histogram can be larger than the maximum value due to the long landau tail to higher values. In addition the mean time reso-

Configuration	**1**	**2**	**3**	**4**	**5**
Mean produced photons	5430	5430	3174	3242	5906
Mean absorbed photons	4716	4716	2562	2970	5364
$\gamma_{detectable}$ **[%]**	13.15	13.15	19.28	8.39	9.18
LY_{mean} **(PDE=1) [p.e./MIP]**	703	778	600	269	540
LY_{max} **(PDE=1) [p.e./MIP]**	567	633	837	360	950
σ_{Cher} **[p.e./MIP]**	31	31	52	33	207
δt **[ns]**	4.31	3.91	4.09	4.85	3.59
Mean detection efficiency [%]	12.6	14.06	18.26	7.93	8.06
Total non-uniformity [%]	15.0	20.0	25	35	65

Table 8.4: Final results of all configurations comparing the simulated quantities. Rectangular sapphire tile with the MPPC positioned at Pos_{opp} (1) and Pos_{lat} (2), rhombic sapphire tiles with a rough (3) and a polished (4) surface finishing and the polished lead glass tile (5).

lution δt of the used materials is provided. On average the Čerenkov photons need about 4 ns to reach the sensitive surface of the MPPC. Lead glass is slightly faster in the propagation of the photons and in case of a polished rhombic sapphire tile it takes the optical photons a slightly longer to reach the MPPC due to their longer path lengths.
Simulations have shown that the gain from the denser lead glass is compensated by

an evenly higher number of absorbed photons. The very broad distributions complicate an accurate fit. A rhombic sapphire tile with a rough surface and wrapped with a specular reflector is the configuration yielding the highest maximum light yield LY_{max} of all sapphire tiles. Although it is also accompanied by a higher non-uniformity. The lowest non-uniformity is observed for a rectangular sapphire tile readout in the configuration Pos_{lat}. The next section will compare the simulated results with those found during test beam measurements.

8.3 Comparison of Data and Simulation Results

All five configurations measured at test beam have been reconstructed with Monte-Carlo (MC) simulations using the Geant4 software package. The test setup did not allow for a comparable precise positioning of the examined tiles with respect to the beam incidence as possible during simulations. In the simulations the tiles are perfectly wrapped with a reflector. Such an accuracy can not be reached in real measurements where gaps in the reflector wrapping exist and the thickness of the air gap in between tile and reflector varies. The tiles were also not scanned over their full width during data acquisition due to time constraints. A comparison of the stated non-uniformity is thus restrained to a limited range of the horizontal extension of the tiles. A comparison between data and MC studies is further complicated through the parametrization requested by the simulation package for the correct propagation of optical photons. Up to which extent the provided values for the five surface parameters agree with reality can not be stated. The estimated errors caused by this uncertainty are 12.4 % for a polished surface and 16 % for an unpolished surface. The shape of the light yield distributions obtained from MC studies and positions scans at test beam are similar. The four configurations for which the MPPC is mounted at the center of the rear back of the tiles show a symmetric distribution around this particular readout position. Whereas if the MPPC is mounted at the lateral side of the tile, the maximum light yield is shifted to this position.
Since no PDE is superimposed in simulations a comparison with absolute numbers from measurements is not possible. The ratio between the measured maximum light yields LY though can be compared (figure 8.8) because the PDE in this case cancels out.
Table 8.5 gives an overview of the five configurations and the comparable quantities from test beam measurements and MC studies. Uncertainties are applied to data and MC results. In order to compare MC and data results the absolute values of the maximum LY from both studies were divided by the maximum light yield measured in configuration (1) for data and MC studies respectively. The spread of the simulated and measured distributions is divided by the respective maximum

Configuration	**1**	**2**	**3**	**4**	**5**
$\mathbf{LY}^{max}_{\mathbf{MC}}$ [%]	100±16	112±18	148±24	63±8	168±21
$\mathbf{LY}^{max}_{\mathbf{DATA}}$ [%]	100±6	60±4	129±8	110±6	160±10
$(\sigma/\mathbf{LY})_{\mathbf{MC}}$ [%]	5.5±0.9	4.9±0.8	6.2±1.0	9.2±1.1	21.8±2.7
$(\sigma/\mathbf{LY})_{\mathbf{DATA}}$ [%]	31.3±2.1	31.0±3.4	17.7±1.6	22.6±1.9	80.5±6.5
$\mathbf{Non\text{-}uni.}_{\mathbf{MC}}$ [%]	10.0±2	5±1	15±2	30±4	60±7
$\mathbf{Non\text{-}uni.}_{\mathbf{DATA}}$ [%]	17.0±2	3±2	22±2	30±2	77±5

Table 8.5: Comparison of data and MC results for all configurations. Configurations: rectangular sapphire tile with the MPPC positioned at Pos_{opp} (1) and Pos_{lat} (2), rhombic sapphire tiles with a rough (3) and a polished (4) surface finishing and the polished lead glass tile (5). Values for the non-uniformity refer to a distance of ±5 mm from the maximum position.

light yield of the configuration:

$$LY^{max} = \frac{LY_i^{max}}{LY_1^{max}}, \tag{8.7}$$

$$\sigma/LY = \frac{\sigma_i}{LY_i}, \tag{8.8}$$

with configuration $i = 1..5$ and $LY_1^{max} = 48$ p.e./MIP in data and $LY_1^{max} = 567$ p.e./MIP in simulations.
The measured maximum light yield LY_1^{max} served as a reference value and can thus not be directly compared in table 8.5. In this case the impact of the PDE on the absolute simulated light yield can be estimated. This results in a simulated maximum light yield of (170±28)p.e./MIP if a mean PDE of 30 % is assumed. This is approximately a factor 3 higher than observed during measurements. A higher light yield in simulations is expected due to the higher precision. A better knowledge of the needed surface parameters would decrease this discrepancy.

Two of the other four configurations agree well within their errors (3,5) whereas configurations (2) and (4) do not agree within data and MC studies. The simulation of a rhombic lead glass tile predicts an occasionally very high number of detected Čerenkov photons. This behavior can be confirmed also by test beam measurements. The maximum number of detected photons is about (68±21) % higher than for configuration (1). The same comparison in data shows a (60±10) % higher maximum light yield. The simulated maximum light yields of a rhombic sapphire tile with a rough surface (3) and a rhombic lead glass tile (5) agree within their errors. In data the resulting light yields are close with a minimum difference of 10 % including errors.
Both, MC as well as test beam studies reveal that in case of the rhombic sapphire tile, a rough surface finish improves the achievable maximum light yield compared

to a polished surface. The impact in simulations is about (57±20) % and about (15±10) % in data. Including errors, those results are close. MC simulations showed that this is due to the lower number of reflections and refractions occuring in case of an unpolished tile surface. The deviation of the two relative values could be caused by the chosen parametrization for the polished tile. If the surface properties do not agree well with reality, i.e. the surface was simulated too smooth, the number of reabsorbed photons increases by mistake.

The spread of the distributions is in data for all configurations broader than in simulations. This again is due to the higher precision provided in simulations. However, the characteristic large width of the lead glass signal response (a factor of 4 - 6 broader than for all other configurations) is observed in MC studies as well as during measurements. It is caused by the strongly fluctuating number of produced and thus detected photons up to very high numbers. Similar to the collected data samples where the MIP peak is hard to distinguish, it is almost not visible in the simulations (see figure 8.7). Hence, also from simulation studies it can be concluded that a lead glass tile with the investigated shape is not suitable for the measurement of Čerenkov photons produced in small tiles.
The spreads of the four sapphire configurations show the same behavior in data and MC. The spread in case of a rectangular sapphire tile is independent of the readout configuration. The distribution for a polished rhombic sapphire tile is broader than if its surface is unpolished.

Measurements show for the two readout configurations of the rectangular sapphire tile a difference of (40±8) %. In simulations a partially opposite behavior is observed. There only a small difference between the two configurations is simulated that is negligible if the errors are taken into account. Such a small difference between the maximum light yields of the two configurations would not be reproducable during test beam measurements. The large and oppositional discrepancy in the tile repsonses observed in MC studies and measurements needs further investigations. It might be caused partially by the conditions at testbeam, allowing no precise position measurements. To move the beam incidence to the maximum beam position in the configuration Pos_{opp} at tile center is easier than in the readout configuration Pos_{lat}.

The non-uniformity of the tile response does not need to be normalized. The vertical direction is found to behave uniformly in simulations as well as during measurements and is not further investigated. Since the horizontal range which was scanned at the test beam differs for each configuration and hence was in all cases but one smaller than the entire tile width, values for the non-uniformity are quoted within ±5 mm around the optimal position. Comparing the values listed in table 8.5 the same trends are visible and the values agree within a few percent. The non-uniformities found at the test beam are partially worse than stated by the simulation which is due to the less stable measuring conditions. The rectangular sapphire tile readout in the configuration Pos_{lat} features with (5±1) % the lowest non-uniformity of all con-

figurations. Based on measurements a non-uniformity of (3±2) % was determined. This configuration is the only one for which the tile was scanned over its entire width resulting in a total non-uniformity of (18±5) % in data and of (20±2) % in simulation which agrees well within the assumed errors.
The second lowest tile non-uniformity is found in case of a rhombic sapphire tile with a rough surface. Simulation predicts a non-uniformity of the tile response of (15±2) %, while from data a value of (22±2) % was extracted. The highly non-uniform tile response of lead glass observed during measurements is reproduced in simulations. The fit results of the MIP peak are subject to large uncertainties.

Summarizing, it can be stated that the simulated relative tile behavior in terms of uniformity and light yield agrees within errors with the measured data. The comparison of the two rhombic sapphire tiles yields a discrepancy between test beam measurements and MC studies. However, the trend to a lower maximum light yield in case of a polished surface is visible in both studies.
Since this was a first approach in studying the measured light yield with simulations a better knowledge of the surface parameters is needed in order to state quantitative relations. Therefore the surface roughness as well as the reflection probabilities would have to be measured and implemented in the simulation framework.
Additionally, by increasing the measurement precision at the test beam an even better agreement between MC simulations and data can be reached.
So far a final comparison shows a satisfying consistency between data and MC studies. Based on simulations qualitative predictions can be made for further configurations.

9 Summary and Outlook

A combination of the particle flow approach (PFA) and the dual-readout technique in one hadronic calorimeter would benefit from the two fundamentally different concepts to improve the jet energy resolution. It is known that the PFA reconstruction algorithm might not be able to reconstruct every single particle and assign it to the correct shower cluster for energies in the TeV region. In those cases information gained from the dual-readout can be used to nevertheless improve the energy resolution.
The cell size optimized for PFA is at the order of some centimeters. In a possible calorimeter design the cell sizes of the scintillator and the Čerenkov layers both have to fulfill this demand. This ensures that the generated Čerenkov light is sampled at the same spatial position and with the same frequency as the scintillation light is detected.

In this thesis, the achievable Čerenkov light yield in small tiles suitable for PFA was measured with MPPC's. For this purpose several different tile configurations were tested in order to find the one most suitable for a possible integration in a hadronic calorimeter. Two quantities are decisive: the absolute light yield in terms of detected photoelectrons and the uniformity of the tile response.
A test setup was built at the DESY test beam facility where the scintillator and the Čerenkov tile were simultaneously exposed to a 3 GeV positron beam. The tile signals were readout with two MPPC's manufactured by Hamamatsu of the type S10362-33-050C and S10362-11-050C. Čerenkov tiles of either rectangular or rhombic shape have been investigated. As Čerenkov tile materials sapphire and lead glass have been studied. Additionally, two different MPPC readout positions of the rectangular sapphire tile were examined.
It was shown that the highest uniformity compared to the other constellations is reached if a rectangular sapphire tile is readout at the lateral tile side, at a 90° rotated position with respect to the beam line. The tile response varied within a 5 mm range around the maximum by only (3±2) % and over the entire tile width by (18±5) %. However, the maximum light yield found in this readout configuration (29±2 p.e./MIP) was the lowest compared to all others. The second lowest non-uniformity of (22±5) % within a 5 mm range around the maximum as well as the second largest light yield (62±4 p.e./MIP) was found for a rhombic sapphire tile with a rough surface finish. Both configurations yield a sufficiently high light yield and are thus promising candidates for the integration into a HCAL combining the ideas of PFA and dual-readout.

Furthermore, it was tried to reconstruct the tile behavior observed at test beam via Monte-Carlo (MC) studies. The simulation of optical photons within the Geant4 framework requires a precise knowledge of the surface properties. Those were estimated within the scope of this thesis by analyzing the impact of several parameters on the light yield. A more accurate way would be to actually measure the surface conditions, primarily the surface roughness. This can be done with for example with an atomic force microscope to determine the degree of height fluctuations.
From the parameter scan an error of 12.4 % or 16 % for a polished or unpolished surface respectively was derived and applied on the MC results. Within errors the results gained from measurements and simulations agree in parts well with each other. It is assumed that the comparison of data and MC studies would agree even better for a more detailed knowledge of the surface characteristics and a more precise measurement of the tile response. The latter would need a more sophisticated test setup able to move in finer steps in the vertical and horizontal direction. To understand the tile behavior under an angular beam incidence one needs a way to rotate the tiles by small, reproducable angles. The measuring conditions would also be improved if the active beam cross section of $5\times5\,\mathrm{mm}^2$ is reduced.

The simulations can be used to find Čerenkov materials with higher transmission probabilities. Possible candidates are for example fused quartz or a wavelength shifting medium. Considering the absolute number of detected photoelectrons the tile shape can be adjusted to improve on quantities as the tile uniformity or the detection efficiency.
Detailed studies are needed to confirm the advantage of a highly granular calorimeter combining PFA with the dual-readout technique. Especially the possible improvement of the jet energy resolution in the multi-TeV energy range needs to be investigated.
The purpose of the presented thesis was to prove that the light yield of small Čerenkov tiles is sufficiently high. Hence, from a technological point of view a feasible solution exists to benefit from the dual-readout information without the need to decrease the granularity of the calorimeter cells.

10 Appendix

Beam Generation at DESY Test Beam

The electron-synchrotron DESY II was built in 1987 and was used as a pre-accelerator for the large electron-proton storage ring HERA. After the shutdown of HERA in 2007 it serves nowadays as a pre-accelerator of electrons and positrons for the two particle accelerators DORIS III and PETRA III. It provides furthermore three test beam lines (21, 22, 24), e.g. for the development and testing of particle detectors. It is a 292.8 m long ring accelerator, operating at 6 GeV with up to 10^{10} particles per second and cm^2. The particles are accelerated in sinusoidal mode with a frequency of 12.5 kHz leading to 80 ms long DESY II cycles.
Electron and positron test beams are available, but only the latter was used for the presented measurements. Figure 10.1a sketches the beam generation. The lepton beam is generated via the formation of bremsstrahlung photons when hitting a carbon fiber of 1 mm thickness. Those photons are converted into electron-positron pairs by a metal plate. The lepton pairs are horizontally spread out with a dipole magnet. Using a collimator the final beam is cut out. The achieved beam energies range from 1 GeV to 6 GeV with an energy spread of 5 % and a beam divergence of 2 mrad. Up to 10^3 positrons per second and cm^2 are available at test beam 21. By changing the current of the dipole magnet one can choose the momentum of the beam particles.

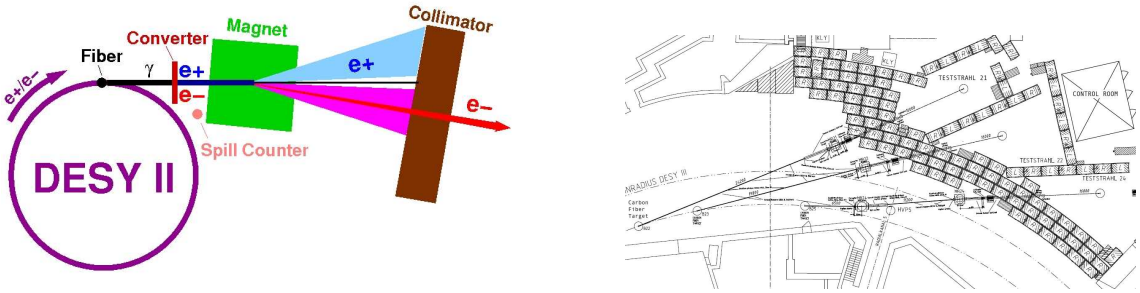

(a) Beam generation at test beam 21.

(b) Sketch of the DESY II test beam area.

Figure 10.1: Data Acquisition at Test Beam.

Correlation Studies

To estimate the correlation between the two signals one data sample collected with the rectangular sapphire tile is analyzed. The positrons traversed first the Čerenkov and then the scintillator tile at a central beam incidence. Note that this study is not meant to be a measure for the described Dual-Readout technique.
The x-axis of each histogram is converted from a QDC-channel scale to a MIP scale to study the correlation of the two measured signal amplitudes. For this purpose the MIP peak of the examined run was fitted and rescaled to one MIP while the pedestal is shifted to zero (figure 10.2). Based on a cut selection on the energy spectra one can observe the different types of trajectories a positron can possibly follow (figure 10.3).

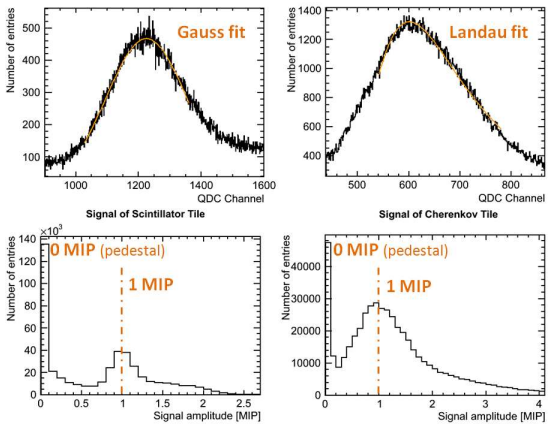

Figure 10.2: Conversion from QDC-channel scale to MIP scale for an example data sample recorded with the rectangular sapphire tile.**Top:** Spectra with x-scale in QDC-channels. **Bottom:** Spectra of the measured visible energy in MIP scale.

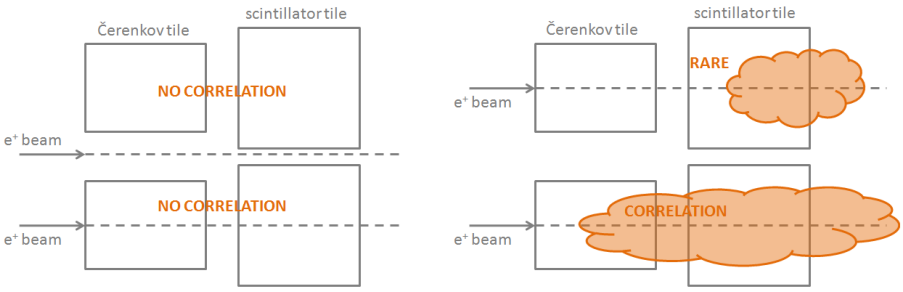

Figure 10.3: Possible event tracks. **Upper Left:** Pedestal events. **Bottom Left:** A MIP signal in each tile. **Upper Right:** The positron starts showering in the scintillator tile. **Bottom Right:** The positron starts already showering in the sapphire tile and continues to do so in the scintillator.

Either the two tiles are missed by the positron and the events are added to the number of entries in the pedestal or the positron traverses the tiles and three different track types are observable. Concerning the former occurrence, the fraction of pedestal events accounts for 17 % in case of the Čerenkov tile (cut at $< 0.2\,\mathrm{MIP}_C$) and of 54 % of all collected events in case of the sintillator tile (cut at $< 0.7\,\mathrm{MIP}_S$). The two dimensional correlation histogram of the measured energy spectra with the two pedestal cuts applied is shown in figure 10.4. The MIP peaks are visible,

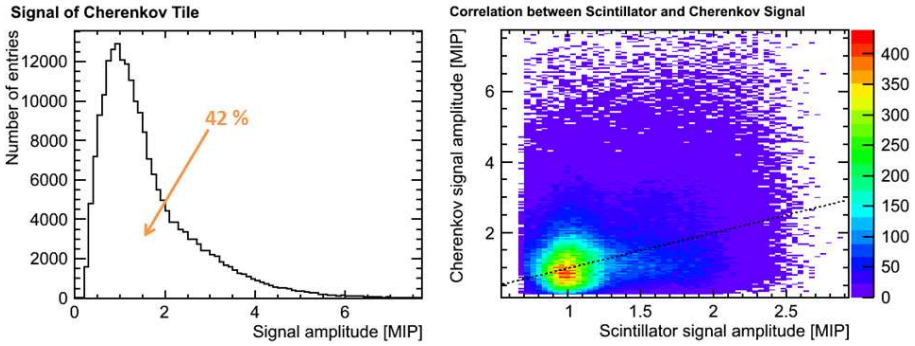

Figure 10.4: Correlation of the visible energy measured by the scintillator and the Čerenkov tile if all pedestal events are discarded. The identity line is indicated by the black dotted line.

but also a fraction of electromagnetically interacting events of both tiles. So far no correlation is visible. A small misalignment of the two tiles in height and their difference in broadness leads to the existence of events where the positron crosses only one of the two tiles. This is eliminated by discarding all pedestal events of both tiles and can therefore not be seen in the pictured histogram. In total 42 % of all events collected remain after the cut.
If the traversing positron is not electromagnetically interacting within any of the two tiles, MIP signals are observed in both of them. Those events are expected to be highly uncorrelated, ideally visible by a circle within a correlation plot of the visible energy. By applying a cut on the scintillator MIP peak (cut at events $\leq 0.7\,\mathrm{MIP}_S$ and $> 1.25\,\mathrm{MIP}_S$) which was placed behind the Čerenkov tile downstream the beam line, the correlation of these events can be visualized (figure 10.5). As expected there is no correlation visible for a cut on the MIP peak in the scintillator due to the single energetic positrons. Approximately 25 % of all events account for such track types excluding pedestal events that remain in the Čerenkov tile (∼3%). 10.6). The last two options for a positron crossing the tiles take into consideration that the positron can interact electromagnetically with one (no correlation measurable) or both of the two tiles. A positron already interacting inside the sapphire tile is yet more probable than a later shower start in the scintillator, due to the smaller radiation length of sapphire. A high correlation of the measured visible energy is expected if the positron interacts within both tiles, which ideally would be reflected by an ellipse around the identity line. By cutting on those events electromagnetically interacting inside the scintillator tile (cut at $\geq 1.25\,\mathrm{MIP}_S$), it is tried to make

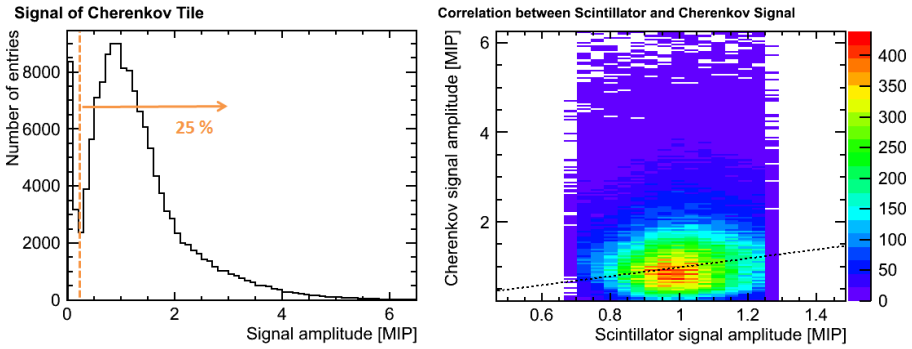

Figure 10.5: Correlation of the visible energy measured by the Čerenkov and the scintillator tile for a cut on the scintillator MIP peak. The remaining pedestal events (below orange line) are excluded. The identity line is indicated by the black dotted line.

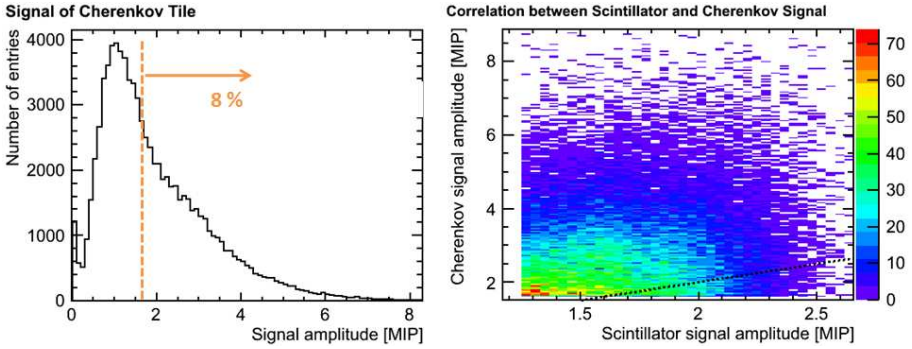

Figure 10.6: Correlation of the visible energy measured by the Čerenkov and the scintillator tile for a cut on events electromagnetically interacting inside the scintillator. The identity line is indicated by the black dotted line.

those events visible (figure About 16 % of all events interact inside the scintillator tile. Excluding those that still gave a MIP-like signal in the Čerenkov tile (cut at $< 1.6\,\mathrm{MIP}_C$), 8% of the measured events remain. The fact that no correlation appears even for those event trajectories, leads to the conclusion that the tiles are to small to obtain satisfying results. The shower leakage is too high for such studies. The situation could be improved if an absorber of a particular depth would be placed in front of the tiles, to place them in the center of the shower development and if the two tiles would be placed on top of each other. In this way the two tiles would sample the same part of the shower and the measured visible energy would be expected to show a higher correlation. Still, the tiles' size would be too small to contain the entire shower. A good correlation therefore can only be reached in a calorimeter-like setup, with larger and more tiles.

Correction of the Rhombic Tile Lengths

The corrected tile length l_{corr} and the corrected light yield LY_{corr} are calculated as follows:

$$l_{corr} = (l_{max} - \frac{c \cdot \Delta x}{\tan \alpha/2})/l_{max} \tag{10.1}$$

$$LY_{corr} = LY_{meas}/l_{corr}, \tag{10.2}$$

where l_{max} is the respective maximum tile length and α the opening angle of the tile. The constant factor c is either 2 or 1 depending on the distance Δx to the tile center and the geometrical extensions.

Histograms of the Parameter Scan

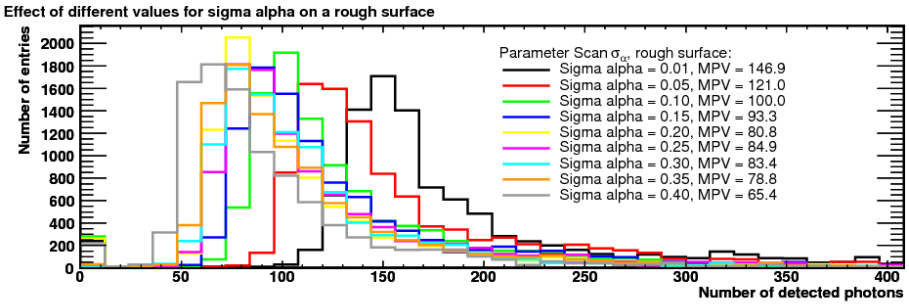

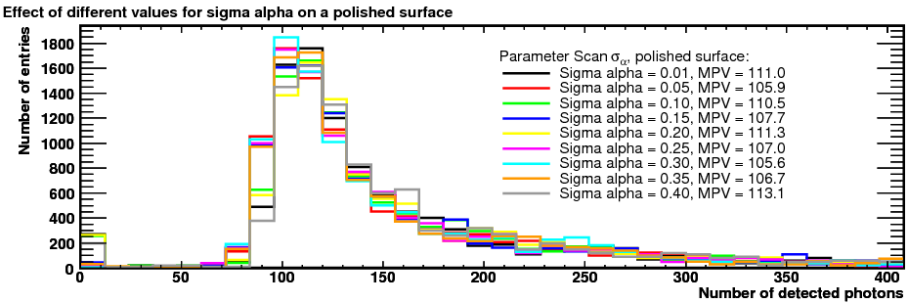

(a)

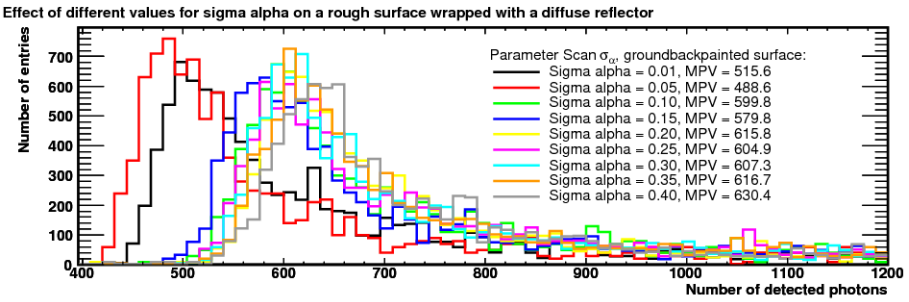

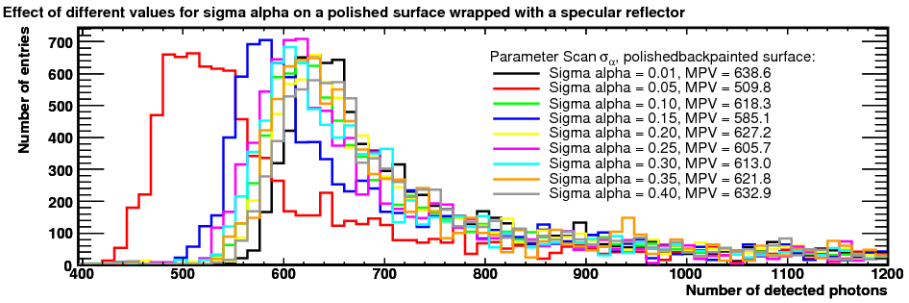

(b)

Figure 10.7: Scan of the parameter σ_α from 0.01 to 1.0 for four different surface types defined by Geant4. a) shows the change in light yield for a rough and a polished surface (*ground* / *polished*) without, b) shows the same with a reflector coating (*groundbackpainted* / *polishedbackpainted*).

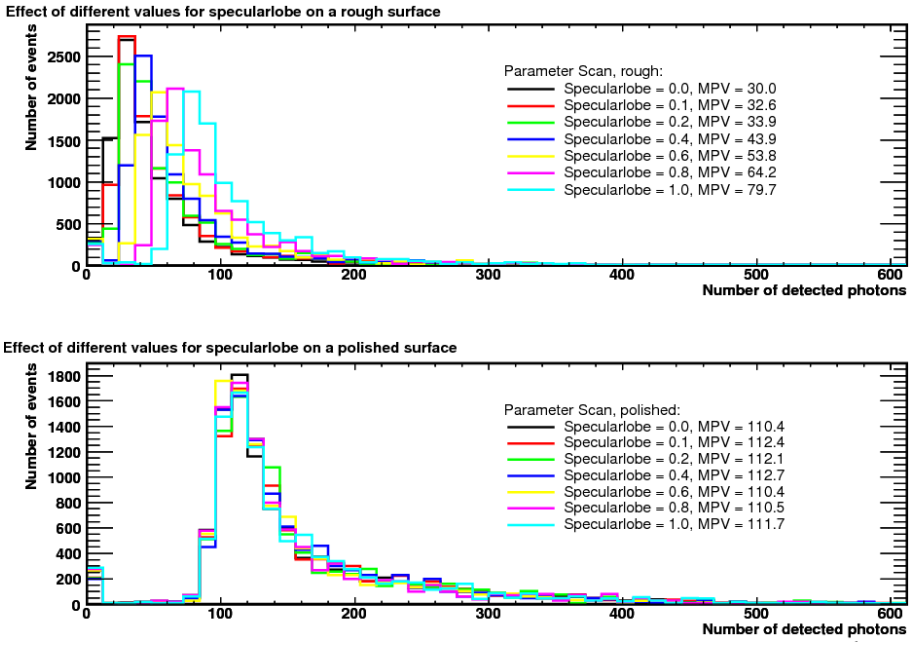

(a)

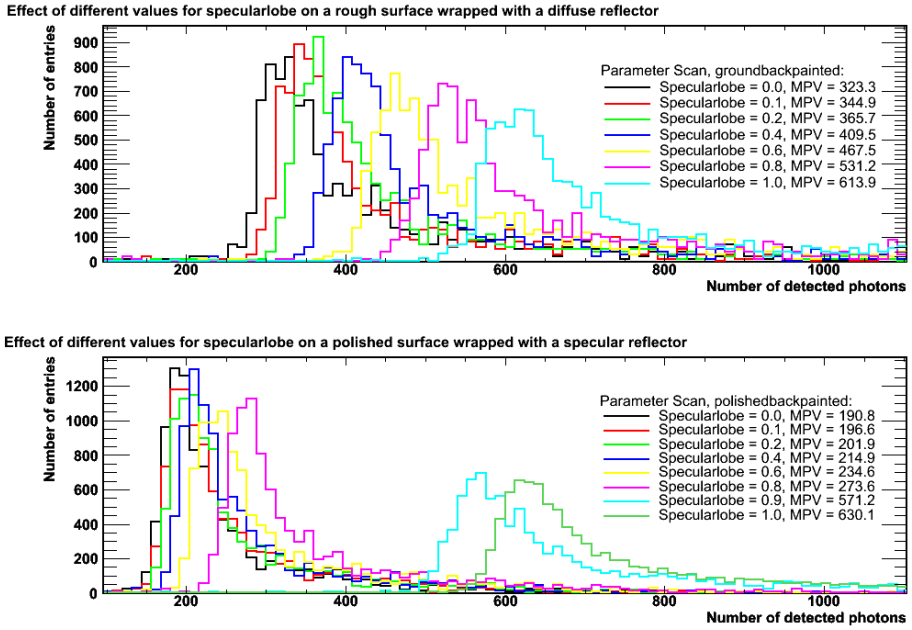

(b)

Figure 10.8: Scan of the parameter C_{sl} from 0.0 to 1.0 for four different surface types defined by Geant4. a) shows the change in light yield for a rough and a polished surface (*ground / polished*) without, b) shows the same with a reflector coating (*groundbackpainted / polishedbackpainted*).

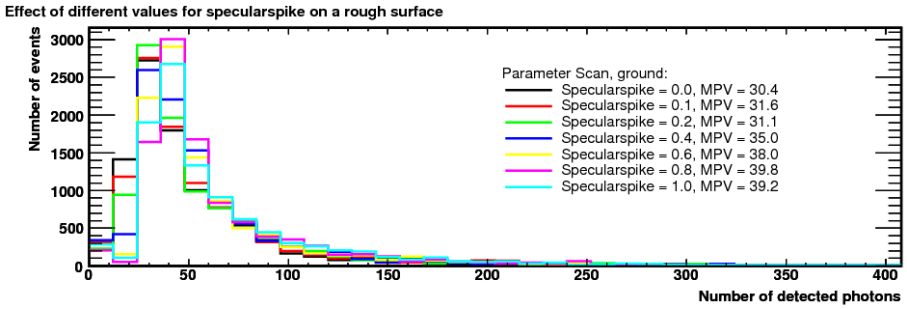

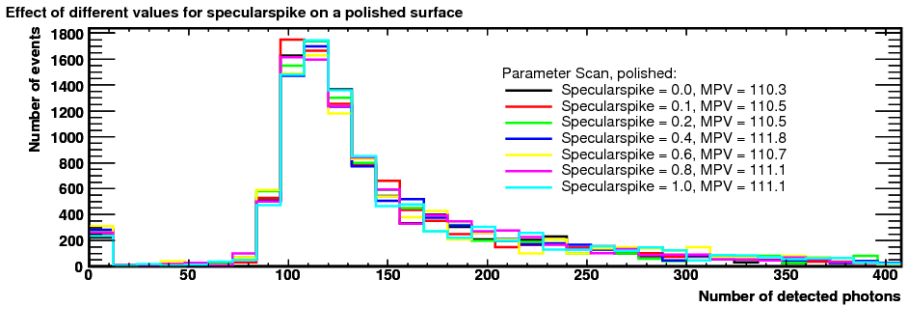

(a)

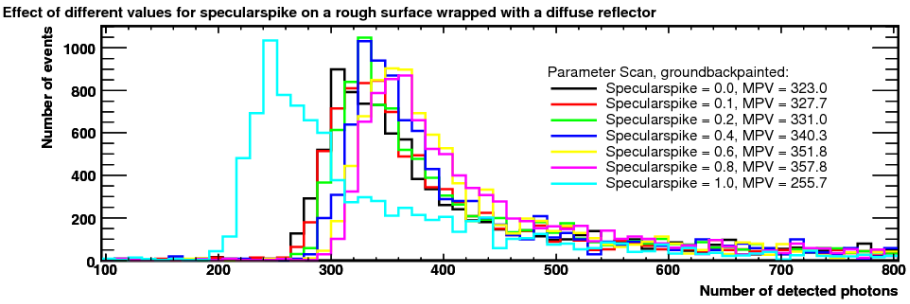

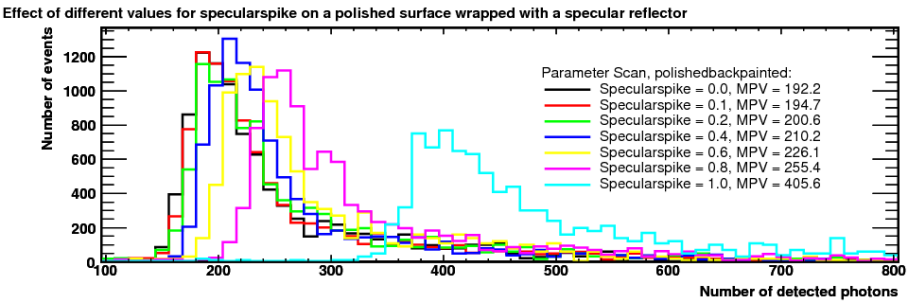

(b)

Figure 10.9: Scan of the parameter C_{ss} from 0.0 to 1.0 for four different surface types defined by Geant4. a) shows the change in light yield for a rough and a polished surface (*ground / polished*) without, b) shows the same with a reflector coating (*groundbackpainted / polishedbackpainted*).

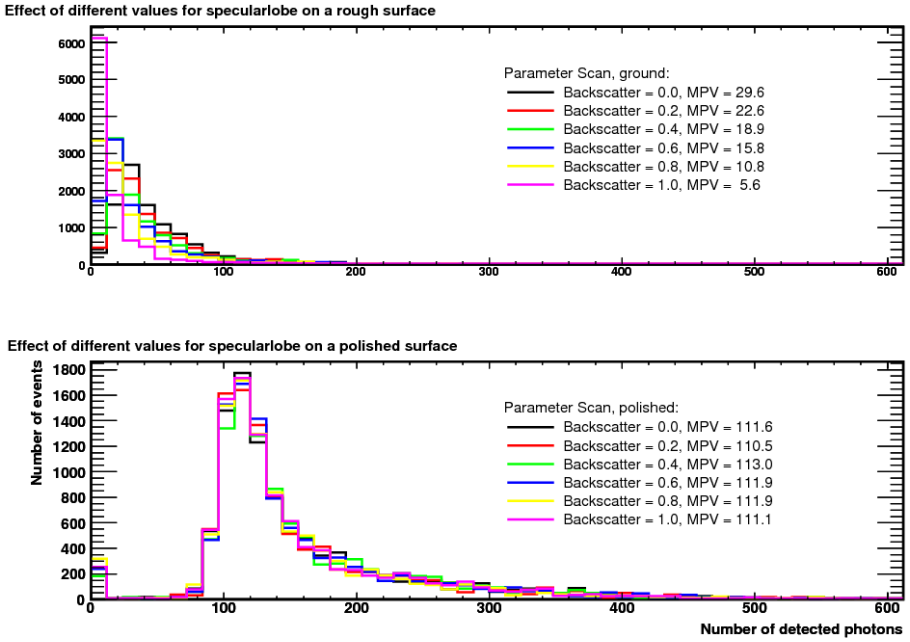

(a)

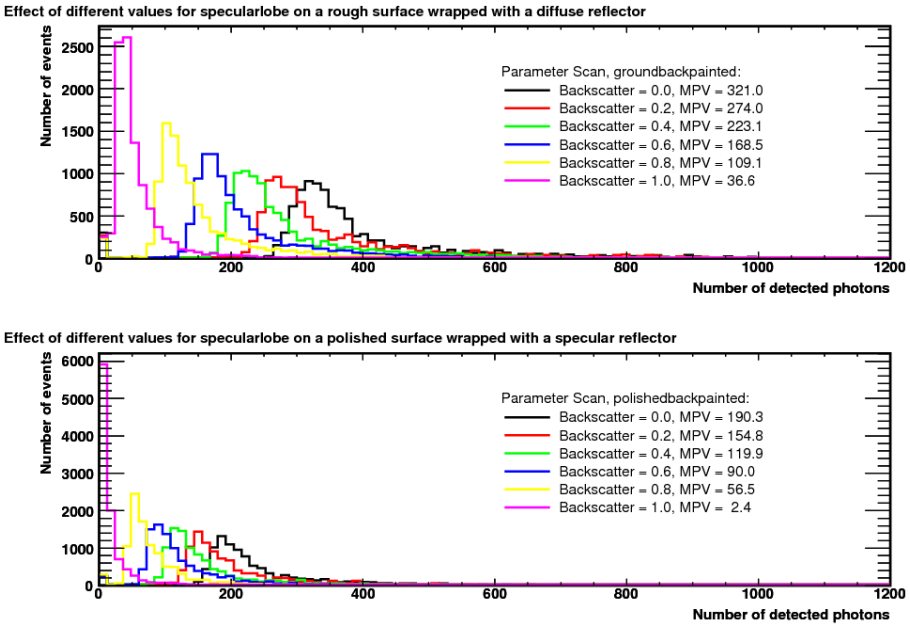

(b)

Figure 10.10: Scan of the parameter C_{bs} from 0.0 to 1.0 for four different surface types defined by Geant4. a) shows the change in light yield for a rough and a polished surface (*ground* / *polished*) without, b) shows the same with a reflector coating (*groundbackpainted* / *polishedbackpainted*).

11 Bibliography

[1] **LEP Working Group for Higgs boson searches, ALEPH Collaboration, DELPHI Collaboration, L3 Collaboration, OPAL Collaboration** Collaboration, R. Barate *et al.*, "Search for the standard model Higgs boson at LEP," *Phys.Lett.* **B565** (2003) 61–75, arXiv:hep-ex/0306033 [hep-ex].

[2] **CDF and D0** Collaboration, "Combined CDF and D0 Upper Limits on Standard Model Higgs-Boson Production with up to 6.7 fb^{-1} of Data," arXiv:1007.4587 [hep-ex].

[3] **ILC** Collaboration, E. Brau, James *et al.*, "ILC Reference Design Report: ILC Global Design Effort and World Wide Study," arXiv:0712.1950 [physics.acc-ph].

[4] **CLIC Study Group** Collaboration, J.-P. Delahaye *et al.*, "CLIC: A Two beam multi-TeV e+- linear collider," arXiv:physics/0008064 [physics].

[5] C. Adloff, Y. Karyotakis, J. Repond, A. Brandt, H. Brown, *et al.*, "Construction and Commissioning of the CALICE Analog Hadron Calorimeter Prototype," *JINST* **5** (2010) P05004, arXiv:1003.2662 [physics.ins-det].

[6] **CALICE** Collaboration, C. Adloff *et al.*, "Response of the CALICE Si-W Electromagnetic Calorimeter Physics Prototype to Electrons," *J.Phys.Conf.Ser.* **160** (2009) 012065, arXiv:0811.2354 [physics.ins-det].

[7] M. Thomson, "Particle Flow Calorimetry and the PandoraPFA Algorithm," *Nucl.Instrum.Meth.* **A611** (2009) 25–40, arXiv:0907.3577 [physics.ins-det].

[8] **ILD Concept Group - Linear Collider** Collaboration, T. Abe *et al.*, "The International Large Detector: Letter of Intent," arXiv:1006.3396 [hep-ex]. http://ilcild.org/documents/ild-letter-of-intent/LOIFeb2010.pdf/view.

[9] E. Aihara, H., E. Burrows, P., E. Oreglia, M., E. Berger, V. Guarino, *et al.*, "SiD Letter of Intent," arXiv:0911.0006 [physics.ins-det]. http://silicondetector.org/display/SiD/LOI.

[10] A. Mazzacane, "The 4th concept detector for the ILC," *Nucl.Instrum.Meth.* **A617** (2010) 173–176. http://www.4thconcept.org/4LoI.pdf.

[11] **GLD Concept Study Group** Collaboration, K. Abe *et al.*, "GLD Detector Outline Document: Version 1.2," arXiv:physics/0607154 [physics].

[12] T. Behnke, "The LDC detector concept," *Pramana* **69** (2007) 697–702.

[13] **CLIC Study Team** Collaboration, H. Braun *et al.*, "CLIC 2008 parameters,".

[14] **CLIC Study Group** Collaboration, R. Corsini, "CLIC R & D Technology, test facilities and future plans," *Nucl.Phys.Proc.Suppl.* **154** (2006) 137–145.

[15] "CLIC Parameter List 3 TeV." http://clic-meeting.web.cern.ch/clic-meeting/clictable2010.html.

[16] **Particle Data Group** Collaboration, K. Nakamura *et al.*, "Review of particle physics," *J.Phys.G* **G37** (2010) 075021.

[17] T. Gabriel, D. E. Groom, P. Job, N. Mokhov, and G. Stevenson, "Energy dependence of hadronic activity," *Nucl.Instrum.Meth.* **A338** (1994) 336–347.

[18] N. Akchurin, K. Carrell, J. Hauptman, H. Kim, H. Paar, *et al.*, "Hadron and jet detection with a dual-readout calorimeter," *Nucl.Instrum.Meth.* **A537** (2005) 537–561.

[19] R. Wigmans, "Calorimetry: Energy measurement in particle physics," *Int.Ser.Monogr.Phys.* **107** (2000) 1–726.

[20] **H1 Collaboration** Collaboration, W. Braunschweig *et al.*, "RESULTS FROM A TEST OF A Pb - Cu LIQUID ARGON CALORIMETER," *Nucl.Instrum.Meth.* **A265** (1988) 419.

[21] **H1 Calorimeter Group** Collaboration, W. Braunschweig *et al.*, "PERFORMANCE OF A Pb Cu LIQUID ARGON CALORIMETER WITH AN IRON STREAMER TUBE TAIL CATCHER," *Nucl.Instrum.Meth.* **A275** (1989) 246–257.

[22] **ALEPH Collaboration** Collaboration, D. Buskulic *et al.*, "Performance of the ALEPH detector at LEP," *Nucl.Instrum.Meth.* **A360** (1995) 481–506.

[23] H. Abramowicz, J. de Groot, J. Knobloch, J. May, P. Palazzi, *et al.*, "THE RESPONSE AND RESOLUTION OF AN IRON SCINTILLATOR CALORIMETER FOR HADRONIC AND ELECTROMAGNETIC SHOWERS BETWEEN 10-GeV AND 140-GeV," *Nucl.Instrum.Meth.* **180** (1981) 429.

[24] **ATLAS Collaboration** Collaboration, G. Aad *et al.*, "The ATLAS Experiment at the CERN Large Hadron Collider," *JINST* **3** (2008) S08003.

[25] I. Knowles and G. Lafferty, "Hadronization in Z0 decay," *J.Phys.G* **G23** (1997) 731–789, arXiv:hep-ph/9705217 [hep-ph].

[26] R. Wigmans, "Energy measurement at the TeV scale," *New J. Phys.* **10** (2008) .

[27] R. Wigmans, "The DREAM project: Results and plans," *Nucl.Instrum.Meth.* **A572** (2007) 215–217.

[28] **DREAM Collaboration** Collaboration, R. Wigmans, "The DREAM project: Towards the ultimate in calorimetry," *Nucl.Instrum.Meth.* **A617** (2010) 129–133.

[29] R. Wigmans, "Recent results from the DREAM project," *J.Phys.Conf.Ser.* **160** (2009) 012018.

[30] M. Kim, C. Avanzini, M. Bagliesi, G. Bigongiari, T. Lomtadze, *et al.*, "Scintillation and Cherenkov light detection with a 3 mm x 3 mm silicon photomultiplier," *Nucl.Phys.Proc.Suppl.* **197** (2009) 325–330.

[31] G. Ahmed, P. Buhler, J. Marton, and K. Suzuki, "Study of timing performance of Silicon Photomultiplier and application for a Cherenkov detector," *Nucl.Instrum.Meth.* **A628** (2011) 393–397, arXiv:1004.4144 [nucl-ex]. * Temporary entry *.

[32] P. Buzhan, B. Dolgoshein, A. Ilyin, V. Kantserov, V. Kaplin, *et al.*, "An advanced study of silicon photomultiplier," *ICFA Instrum.Bull.* **23** (2001) 28–41.

[33] Hamamatsu, "Multi-Pixel Photon Counter, Technical Information." http://jp.hamamatsu.com/resources/products/ssd/eng/html/mppc_e/pdf/mppc_kapd9003e02.pdf.

[34] http://sales.hamamatsu.com/en/products/solid-state-division/si-photodiode-series/mppc.php. January 2011.

[35] N. Wattimena, "The calice tile hadron calorimeter prototype with silicon photomultiplier readout." In *10th ICATPP Conference on Astroparticle, Particle, Space Physics, Detectors and Medical Physics Applications*, 2007.

[36] H. Spieler, "Semiconductor detector systems," *Ser.Semicond.Sci.Tech.* **12** (2005) 1–489.

[37] M. Yokoyama, "Performance of multi-pixel photon counters for the T2K near detectors," *Nuclear Instruments and Methods in Physics Research Section A: Accelerators, Spectrometers, Detectors and Associated Equipment* **622, Issue 3** (2010) 567–573.

[38] N. Feege, "Silicon photomultipliers: Properties and application in a highly granular calorimeter,". DESY-THESIS-2008-050.

[39] A. Lacaita, S. Cova, A. Spinelli, and F. Zappa, "On the bremsstrahlung origin of hot-carrier-induced photons in silicon devices," *IEEE Trans. Electron Dev.* **40, Issue 3** (1993) 577 – 582.

[40] P. Eckert, "Advanced Silicon-Photomultiplier Characterization for Calorimetric Applications," 2010. University of Heidelberg, Kirchhoff-Institute for Physics, Diploma thesis HD-KIP 10-11.

[41] P. Eckert, H.-C. Schultz-Coulon, W. Shen, R. Stamen, and A. Tadday, "Characterisation Studies of Silicon Photomultipliers," *Nucl.Instrum.Meth.* **A620** (2010) 217–226, arXiv:1003.6071 [physics.ins-det].

[42] A. Tadday, "Characterisation of Silicon Photomultipliers," 2008. University of Heidelberg, Kirchhoff-Institute for Physics, Diploma thesis HD-KIP 08-18.

[43] 3M Deutschland GmbH. http://3m.com.

[44] Pt100 temperature sensor. http://www.picotech.com/pt100_sensors.html.

[45] V. L. Morgunov, "International Workshop on Linear Colliders 2010, The fastest Calorimeter." http://ilcagenda.linearcollider.org/getFile.py/access?contribId=328&sessionId=56&resId=0&materialId=slides&confId=4507.

[46] Vladimir. http://uniplast-vladimir.com.

[47] RSA LE RUBIS SA, "Sapphire Properties." http://www.rubisrsa.com/b/s/408/fiches/2RSAVerneuilSapphireProperties1.pdf.

[48] Schott AG, "Data Sheet SF5," 2003. http://www.schott.com/advance_optics/english/abbe_datasheets/datasheet_sf5.pdf.

[49] Official Geant4 Homepage. http://www.geant4.org/geant4.

[50] **GEANT4** Collaboration, S. Agostinelli *et al.*, "GEANT4: A Simulation toolkit," *Nucl.Instrum.Meth.* **A506** (2003) 250–303.

[51] "GEANT4 Reference Manual." http://www.geant4.org/geant4.

[52] K. Grimm and M. Gericke, "QWeak GEANT4 Code Manual," 2007. http://www.phys.vt.edu/~jmammei/example_code/qweaksimdoc.pdf.

[53] R. C. Alig, S. Bloom, and C. W. Struck, "Scattering by ionization and phonon emission in semiconductors," *Phys. Rev. B* **22** no. 12, (Dec, 1980) 5565–5582.

[54] A. Levin and C. Moisan, "A More Physical Approach to Model the Surface Treatment of Scintillation Counters and its Implementation into DETECT," *IEEE Trans.Nucl.Sci.* (Oct. 1996) . TRI-PP-96-64.

[55] G.F. Knoll, T.F. Knoll and T.M. Henderson, "Light Collection Scintillation Detector Composites for Neutron Detection," *IEEE Trans.Nucl.Sci.* **35, Issue 1** (1988) 872–875.

[56] W. Janecek and W. Moses, "Simulating Scintillator Light Collection Using Measured Optical Reflectance," *IEEE Trans.Nucl.Sci.* **57, Issue 3** (Jun. 2010) .

[57] P. Papacz, "Optimisation of the Particle Detection Efficiency for Scintillation Detectors with SiPM Readout,". Rheinisch-Westf'alischen Technischen Hochschule Aachen, III. Physikalisches Institut A, Diploma thesis.

[58] K. I. S. K. Nayar and T. Kanadae, "Surface Reflection: Physical and Geometrical Perspectives," *Carnegie Mellon University, The Robotics Institute* (March 1989) . CMU-RI-TR-89-7.

[59] J. D. Jackson, *Classical Electrodynamics*. de Gruyter, Berlin, 2006.

[60] GEANT4 Forum, personal communication with P. Gumplinger. `http://hypernews.slac.stanford.edu/HyperNews/geant4/get/opticalphotons/370.html`.

[61] B. S. Patel and Z. H. Zaidi, "The suitability of sapphire for laser windows," *Measurement Science and Technology* **10, Issue 3** (1999) 146.

Danksagung

Ich möchte mich gerne bei mehreren Personen bedanken, die auf ganz unterschiedliche Weisen diese Diplomarbeit unterstützt haben.
Zunächst möchte ich mich bei Prof. Dr. Hans-Christian Schultz-Coulon und Dr. Erika Garutti bedanken, die diese Diplomarbeit ermöglicht und betreut haben. Prof. Dr. Dirk Dubber danke ich für die Bereitschaft diese Arbeit als Zweitgutachter zu korrigieren.

Daneben gilt mein Dank meinen Betreuern Dr. Martin Göttlich, Dr. Mark Terwort und Yuri Soloviev. Jeder von Ihnen hat mich über die Dauer der vorliegenden Diplomarbeit zweitweise intensiv betreut und Mark hat sich bereit erklärt einen großen Teil dieser Diplomarbeit Korrektur zu lesen.
Ich danke Dr. Benjamin Lutz für die immer sehr hilfreichen und ausschlaggebenden Tips und Diskussionen. Vorallem für die spontane Unterstützung am Test Strahl, die genau zum richtigen Zeitpunkt kam.

Mein ganz besonderer Dank gilt Alexander Kaplan. Für all die hilfreichen Erklärungen und Gespräche, vor allem auch für die freundschaftliche Unterstützung und ein immer offenes Ohr. Ich hätte mir keine bessere Bürogesellschaft vorstellen können. Ich wünsche ihm für die Zukunft von Herzen alles Gute, viel Erfolg beim Abschluss seiner Doktorarbeit und ein ganz besonderes Jahr 2011.

Desweiteren möchte ich mich bei den restlichen Mitgliedern der FLC Gruppe am DESY und am KIP bedanken für die immer problemlose Hilfe und schnelle Beantwortung von Fragen, für eine schöne Arbeitsatmosphäre und viel Spaß beim Kanufahren und Grillen.

Meinen Eltern, meiner restlichen Familie und all meinen Freunden aus nah und fern danke ich abschließend für die einjährige Unterstützung. Ihr habt mich mit viel Geduld während dieser stressigen Zeit immer wieder aufgefangen und neu motiviert. Eure zahlreichen Besuche haben mir die Zeit in Hamburg verschönert.

Vielen Dank!

Erklärung:

Ich versichere, dass ich diese Arbeit selbstständig verfasst habe und keine anderen als die angegebenen Quellen und Hilfsmittel benutzt habe.

Heidelberg, den 22. Februar 2011 .....